

**APPLICATION OF ACTIVE FLOW CONTROL TECHNOLOGY IN
AN UNMANNED AERIAL VEHICLE**

A Thesis

by

GAURAV

Submitted to the Office of Graduate Studies of
Texas A&M University
in partial fulfillment of the requirements for the degree of

MASTER OF SCIENCE

August 2007

Major Subject: Mechanical Engineering

**APPLICATION OF ACTIVE FLOW CONTROL TECHNOLOGY IN
AN UNMANNED AERIAL VEHICLE**

A Thesis

by

GAURAV

Submitted to the Office of Graduate Studies of
Texas A&M University
in partial fulfillment of the requirements for the degree of

MASTER OF SCIENCE

Approved by:

| | |
|-------------------------|---------------------|
| Co-Chairs of Committee, | Othon K. Rediniotis |
| | Luis San Andres |
| Committee Member, | Jerald A. Caton |
| Head of Department, | Dennis O' Neal |

August 2007

Major Subject: Mechanical Engineering

ABSTRACT

Application of Active Flow Control Technology in
an Unmanned Aerial Vehicle. (August 2007)

Gaurav, B.E., National Institute of Technology, Allahabad, India.

Co-Chairs of Advisory Committee: Dr. Othon K. Rediniotis
Dr. Luis San Andres

A low speed wind tunnel experimental investigation was conducted to determine the effectiveness of the leading edge pulsed blowing and the trailing edge jet blowing/ Gurney flap on the improvement of aerodynamic performance of an unmanned aerial vehicle at low Reynolds numbers.

The wind tunnel tests for the leading edge pulsed jet blowing were conducted at 10%, 30% and 50% location of the chord length from the leading edge at a free stream velocity of 20 m/s. The jet momentum coefficient and the non-dimensional pulser frequency had been varied independently to investigate the effectiveness of the leading edge pulsed blowing. The trailing edge jet blowing tests were conducted at free stream velocity of 20 m/s at different jet momentum coefficients.

The leading edge pulsed blowing showed a strong dependency of the actuator effectiveness on the jet momentum and the pulser frequency. The leading edge pulsed blowing had delayed the flow separation over the airfoil from an angle of attack of 17° to 22° with a docile stall for jet emanating at 10% location of the chord length for a jet momentum coefficient of 0.0275. The pulsed blowing at 50% chord location generated

higher lift compared to the 10% location of the pulser with an abrupt stall at 19° . There was no evidence of the lift augmentation in the pre-stall angle of attack regime.

The experimental results showed that the trailing edge jet flap was capable of generating significant roll moment at realistic jet momentum coefficients.

The fluidic actuators were then integrated into the wings of a $\frac{1}{3}$ scale Extra 330 model airplane. The wind tunnel results for the leading edge pulsed blowing on the scale model indicated a delay in the stall of the airplane from an angle of attack of 12° to 21° with a 13% increase in the lift at take-off and landing speed of 17 m/s. The trailing edge jet actuators were also able to augment lift and demonstrate the roll control authority at low angle attacks at a cruising speed of 30 m/s.

DEDICATION

*To my parents, Veena and Anil Kumar
and my sister, Ragini.*

ACKNOWLEDGMENTS

I would like to thank Dr. Othon K. Rediniotis for allowing me to contribute to this research project and for his continual guidance in my education and research. I also thank my committee members, Dr. Luis San Andres and Dr. Jerald A. Caton, for their support and advice.

I would also like thank Dr. Lance W. Traub, whose expert knowledge and advice on experimental aerodynamics has been invaluable. His assistance in this research endeavor has contributed to its success. Additionally, I would like to thank my fellow colleagues involved in this project, Dr. John Valesak, Dr. Isaac Ekoto, Abhinav Kumar and Andrew Beckett, who have helped me during the course of the project.

I thank the technical staff of the Aerospace Engineering Department, Texas A&M University, Josh Weimar, and Rick Allen, for their help in manufacturing and fabricating various components for the project.

TABLE OF CONTENTS

| | Page |
|---|------|
| ABSTRACT | iii |
| DEDICATION | v |
| ACKNOWLEDGMENTS..... | vi |
| TABLE OF CONTENTS | vii |
| LIST OF TABLES | ix |
| LIST OF FIGURES..... | x |
| INTRODUCTION..... | 1 |
| General | 1 |
| Prior Work - Jet/Gurney Flap..... | 4 |
| Prior Work - Separation Control | 9 |
| Research Procedure | 11 |
| EXPRESSION OF UNCERTAINTY | 12 |
| TRAILING EDGE JET BLOWING..... | 14 |
| General | 14 |
| Setup and Procedure..... | 14 |
| Results and Discussions | 18 |
| Wake Survey | 21 |
| LEADING EDGE PULSED BLOWING | 24 |
| General | 24 |
| Wing Model..... | 26 |
| Wind Tunnel Facility | 31 |
| Wind Tunnel Test Matrix..... | 33 |
| Force Balance Results | 34 |
| Surface Pressure Measurements..... | 44 |
| Flow Reattachment through Sudden Pulsed Blower Actuation..... | 48 |

| | Page |
|--|------|
| THE TEST VEHICLE | 57 |
| The Extra 330 “Basic” Wing..... | 59 |
| The Wing with Fluidic Actuators..... | 60 |
| Leading Edge Actuators..... | 61 |
| Trailing Edge Jet Blower..... | 65 |
| Optical Tachometers | 69 |
| In-flight Pressure Measurement | 70 |
| Final Assembly..... | 71 |
| WIND TUNNEL TESTING OF THE VEHICLE | 73 |
| Facility Description..... | 73 |
| Wind Tunnel Test Matrix..... | 75 |
| Discussion of Test Results | 78 |
| CONCLUSIONS AND RECOMMENDATIONS | 84 |
| Conclusions | 84 |
| Recommendations | 85 |
| REFERENCES..... | 86 |
| VITA | 94 |

LIST OF TABLES

| | Page |
|---|------|
| Table 1. Test matrix for jet/Gurney flap characteristics on aerodynamic performance. | 18 |
| Table 2. Specification of the experimental setup for pulsed blowing | 27 |
| Table 3. Location of pressure ports on the wind tunnel model | 28 |
| Table 4. Specifications of $\frac{1}{3}$ scale Extra 330 model airplane. | 57 |
| Table 5. Zenoah G800 BPU engine specifications | 58 |
| Table 6. Specification of servos used in the basic configuration of the test vehicle..... | 60 |
| Table 7. Specification of servos used in the test vehicle with fluidic actuators..... | 69 |
| Table 8. Comparison of the conventional wing and the wing with fluidic actuators..... | 72 |
| Table 9. Flow characteristics of the O. W. Nicks Low Speed Wind Tunnel | 74 |
| Table 10. O.W. Nicks Low Speed Wind Tunnel external balance specification..... | 74 |
| Table 11. Low speed wind tunnel test matrix using conventional wings | 76 |
| Table 12. Low speed wind tunnel test matrix using wings with reduced ailerons..... | 76 |
| Table 13. Low speed wind tunnel test matrix using wings with fluidic actuators | 78 |

LIST OF FIGURES

| | Page |
|---|------|
| Figure 1. A Gurney flap | 4 |
| Figure 2. Flow conditions at the trailing edge of a conventional wing ¹⁶ | 5 |
| Figure 3. Flow at the trailing edge of the wing with a Gurney flap ¹⁶ | 5 |
| Figure 4. Time averaged LDA results of 4% Gurney at 0° angle of attack ²⁰ | 7 |
| Figure 5. Flow over NACA 0012 with Gurney flap at 10 m/s and 0° angle of attack ²⁰ ... | 7 |
| Figure 6. 1 ft by 1 ft wind tunnel facility at Texas A&M University | 14 |
| Figure 7. Specifications of the trailing edge jet blowing experimental setup | 15 |
| Figure 8. Flow visualization of the trailing edge jet blowing | 17 |
| Figure 9. Measured variation of lift coefficient with angle of attack..... | 19 |
| Figure 10. Variation of lift augmentation ratio with C_{μ} at 0° angle of attack | 20 |
| Figure 11. Variation of zero lift angle of attack with C_{μ} | 20 |
| Figure 12. Variation of lift coefficient with C_{μ} at 0° angle of attack | 21 |
| Figure 13. Wake surveys conducted at two chord lengths downstream of the trailing edge..... | 22 |
| Figure 14. Effect of jet flap on measured drag coefficient..... | 23 |
| Figure 15. Centrifugal fan based pulsed blower | 25 |
| Figure 16. Velocity profile of pulsed air at fan speed of 6000 rpm and a frequency of 225 Hz | 26 |
| Figure 17. NACA 0015 profile based wind tunnel model | 27 |
| Figure 18. Leading edge pulsed air blowing experimental set up in 3 ft by 4 ft wind tunnel | 28 |
| Figure 19. Effect of pulser location on loss coefficient, k | 29 |

| | |
|--|----|
| Figure 20. Exit velocity profile at $x/c = 0.1$ at pulsed air frequency of 72 Hz..... | 30 |
| Figure 21. Exit velocity profile at $x/c = 0.5$ at pulsed air frequency of 130 Hz..... | 31 |
| Figure 22. Performance curves of L.E. pulsed blowing at constant $C_{\mu} = 0.0075$ | 35 |
| Figure 23. Performance curves of L.E. pulsed blowing at constant $C_{\mu} = 0.015$ | 36 |
| Figure 24. Performance curves of L.E. pulsed blowing at constant $C_{\mu} = 0.0275$ | 37 |
| Figure 25. Variation of maximum lift coefficient with C_{μ} at different F^{+} | 38 |
| Figure 26. Performance curves of L.E. pulsed blowing at constant $F^{+} = 0$ | 39 |
| Figure 27. Performance curves of L.E. pulsed blowing at constant $F^{+} = 1.5$ | 40 |
| Figure 28. Performance curves of L.E. pulsed blowing at constant $F^{+} = 1.0$ | 41 |
| Figure 29. Performance curves of L.E. pulsed blowing at constant $F^{+} = 1.5$ | 42 |
| Figure 30. Variation of maximum lift coefficient with F^{+} at different C_{μ} | 43 |
| Figure 31. Effect of pulsed air blowing on the wing surface pressure distribution at $C_{\mu} = 0.0075$ | 45 |
| Figure 32. Effect of pulsed air blowing on the wing surface pressure distribution at $C_{\mu} = 0.015$ | 46 |
| Figure 33. Effect of pulsed air blowing on the wing surface pressure distribution at $C_{\mu} = 0.0275$ | 47 |
| Figure 34. Response of leading edge pulser at $x/c = 0.1$ on sudden actuation..... | 49 |
| Figure 35. Response of leading edge pulser at $x/c = 0.3$ on sudden actuation..... | 50 |
| Figure 36. Response of leading edge pulser at $x/c = 0.5$ on sudden actuation..... | 51 |
| Figure 37. Flow visualization using tufts at 20.4° angle of attack with no actuation | 52 |
| Figure 38. Flow visualization using tufts at 20.4° angle of attack at $x/c = 0.1$ | 53 |
| Figure 39. Flow visualization using tufts at 20.4° angle of attack at $x/c = 0.3$ | 54 |

| | Page |
|--|------|
| Figure 40. Flow visualization using tufts at 20.4° angle of attack at $x/c = 0.5$ | 55 |
| Figure 41. Flow visualization at various operating conditions | 56 |
| Figure 42. A $\frac{1}{3}$ scale Extra 330 model airplane | 58 |
| Figure 43. Top view of $\frac{1}{3}$ scale Extra 330 model airplane | 59 |
| Figure 44. CAD model of the original wing | 60 |
| Figure 45. Leading edge actuator at 15 % chord length location..... | 62 |
| Figure 46. Two impeller fan housing and brushless motors | 62 |
| Figure 47. Intake manifold for the leading edge pulsed blowing..... | 63 |
| Figure 48. Impeller with aluminum insert..... | 63 |
| Figure 49. The pulser housing; inset: exit jet slot geometry and delivery manifold..... | 64 |
| Figure 50. The pulser shaft and its driving mechanism | 65 |
| Figure 51. Location of trailing edge jet blower assembly..... | 65 |
| Figure 52. Modified wing structure and the ribs | 66 |
| Figure 53. Full and reduced aileron | 67 |
| Figure 54. Trailing edge wire mesh intake manifold and modified wing structure | 67 |
| Figure 55. Trailing edge jet blower assembly in Plexiglass [®] | 68 |
| Figure 56. Trailing edge jet flap and servo mechanism for jet flap deflection control | 68 |
| Figure 57. Flow visualization of the trailing edge jet at different deflection angles..... | 69 |
| Figure 58. Optical sensor and its control circuit | 70 |
| Figure 59. 5-Hole probe and pressure ports on the upper surface of the wing | 71 |
| Figure 60. Mountings for the airplane in the low speed wind tunnel..... | 73 |

| | Page |
|---|------|
| Figure 61. Control Station and the Labview [®] based program to control the vehicle | 75 |
| Figure 62. Electronic components and wiring harness..... | 76 |
| Figure 63. Pulser velocity profile at fan speed of 12000 rpm | 77 |
| Figure 64. UAV performance at free stream velocity of 17 m/s, leading edge pulser $C_\mu = 0.0275$, $F^+ = 1.0$; trailing edge jet blower $C_\mu = 0.0075$ | 81 |
| Figure 65. UAV performance with trailing edge actuators at free stream velocity of 30 m/s, trailing edge jet blower $C_\mu = 0.0024$ | 82 |
| Figure 66. UAV performance with trailing edge actuators at free stream velocity of 17 m/s, trailing edge jet blower $C_\mu = 0.0075$ | 83 |

INTRODUCTION

General

Advances made in flow control technology have greatly increased the military acceptance of and demand for unmanned aerial vehicles. These vehicles have become an integral part of world's military with their increased application in battlefield. The technology evolution in the field of flow control has increased the possibilities for the improvement in the unmanned aerial vehicle performance.

Aerodynamically, a vast majority of the aircraft operation is spent in the attached flow regime. During take-off and landing, enhanced performance of the aircraft requires its operation at high angle of attack, which may cause the flow over the wings to separate. Flow control technology can be integrated with the flight control to yield improvements in the aerodynamic performance and increased endurance. In addition, it may also reduce the risk of detection by the enemy because of its inherent stealth capability (no conventional moving surfaces).

Flow control may be used to control/promote the boundary layer transition, to limit flow separation, to augment lift and to reduce drag, either actively or passively. It can also be used for the “dynamic” modification of the pressure distribution over a wing surface.

Passive modes of flow control, e.g. distributed roughness over a surface¹, vortex generators² and self-excited rods³, augment the boundary layer momentum through

This thesis follows the format of the *AIAA Journal*.

enhanced mixing or by introducing velocity fluctuations in the transverse direction to control flow separation without any addition of energy.

Active flow control techniques can be implemented through various methods e.g., continuous blowing⁴, continuous suction⁵, pulsed blowing⁶, oscillatory blowing and suction⁷, vibrating ribbons⁸, wall oscillations⁹ and net-zero mass flux actuators¹⁰⁻¹¹. Desired results are achieved by either removing the low energy carrying fluid from the boundary layer or by increasing the boundary layer momentum. Net-zero mass flux actuation and pulsed blowing additionally introduce vortical structures into the flow, which influence the mixing of the slow moving boundary layer with the free stream.

Earlier methods demonstrating the application of active flow control technology had used pneumatic actuation using compressed air supply¹² or the moving/non-stationary surface¹³. These methods have inherent issues in the practical application because of reduced structural stability and the feasibility/availability of compressed air in an unmanned aerial vehicle. Net-zero mass flux actuators using piezoelectric transducers¹⁴⁻¹⁵ had been used to demonstrate the application of active flow control technology in an unmanned aerial vehicle. However, the aircraft had a limited operating range because of limited mass flow rates, frequency bandwidth and the angle of attack regime in which the actuators were effective. The results suggest that a more global implementation approach is required for the effective flight control throughout the angle of attack regime. The transition of active flow technologies from laboratory to the test flight is thus very challenging.

The objective of the current research is to develop and to prove that flow manipulation over the wings is achievable, and then to implement it in a prototype, demonstrating its application to facilitate the performance enhancement on an unmanned aerial vehicle. NACA 0015 airfoil geometry and a $\frac{1}{3}$ scale Extra 330 model airplane have been used to demonstrate the new developments in the subject matter.

The behavior of the flow over the airfoil, with and without control is reviewed. The data analysis from the low speed wind tunnel experiments on NACA 0015 reveals an extension in the angle of attack envelope by suppressing the flow separation, and a possibility of hinge-less control through leading and trailing edge flow manipulation.

With this key information, flow control devices have been optimally designed and integrated into a test vehicle. The flow control devices and parts, along with the associated electronic components are designed for easy integration with the end user configurable avionics, with an ease in serviceability of the parts. Commercially available software and hardware components have been used for the bench top and wind tunnel testing of the fluidic actuators. Reduced in-board ailerons are provided as a backup in case of any unforeseen in-flight failure of the fluidic actuators. The performance characteristics of the modified airplane are investigated in a low speed wind tunnel at the cruising and take-off/landing speeds. The experimental results will be presented using a variety of standard performance descriptors that allow quantification of the gains achieved by flow control.

Prior Work - Jet/Gurney Flap

Aerodynamic control effectors, usually an aileron or elevator, create a useful and controllable change in the lateral and longitudinal flight behavior. The geometry of the trailing edge has a significant influence on the degree of control and the improvement made in the airfoil aerodynamic performance.

The flow manipulation around the trailing edge can be achieved either through active or passive means. Integration of a Gurney flap, a simple passive device, at the trailing edge of an airfoil has enhanced the aerodynamic performance in car racing applications for a long time. A Gurney flap, as shown in Figure 1, is a small plate attached along the trailing edge and is generally normal to the pressure (lower) side of the airfoil. The dimensions of the flap range from 0.5% to 1.5% of the chord length, such that the flap remains inside the boundary layer at the trailing edge.

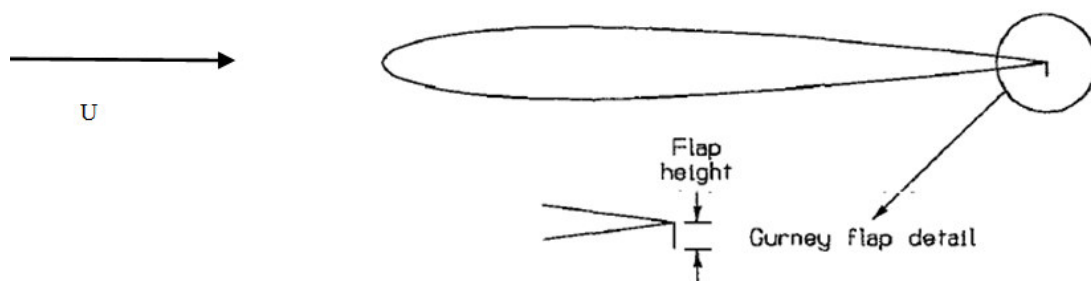


Figure 1. A Gurney flap

Experimental investigations made by Liebeck¹⁶ and Neuhert¹⁷ reveal a significant amount of flow turning over the backside of the flap when compared to flow at the trailing edge of a conventional wing (Figure 2). The reverse flow region, modeled by

two counter rotating vortices in Figure 3, has also been observed behind the flap. The results had indicated an increase in the lift coefficient with a slight reduction in the drag. The results are in agreement with earlier studies so long as the flap is inside the boundary layer.

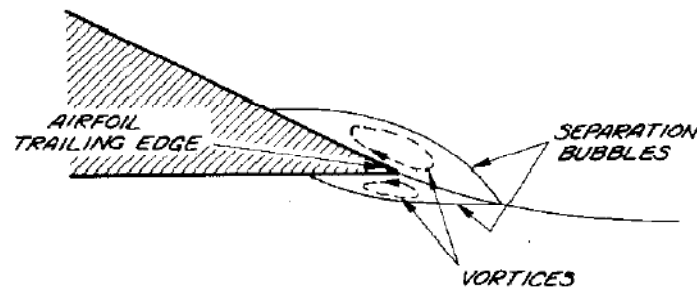


Figure 2. Flow conditions at the trailing edge of a conventional wing¹⁶

The independent studies done by Myose¹⁸⁻¹⁹ and Jeffrey²⁰ explain the phenomenon of high lift generated by Gurney flaps. Time averaged Laser Doppler Anemometry done downstream of the flap²⁰ have a good correlation with the results obtained by Liebeck¹⁶. However, the instantaneous results have indicated a wake of alternatively shedding Von-Karman vortex-street.

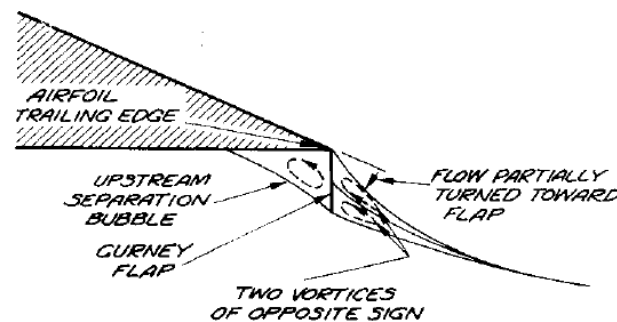


Figure 3. Flow at the trailing edge of the wing with a Gurney flap¹⁶

During the initial stages of formation of the Von-Karman vortex-street²¹, a separated shear layer on the one side of the body rolls up to form a vortex. At the same time, it draws the separating flow from the other side of the body. As it crosses the centerline of the wake, it cuts off the supply of the former. At this point, the vortex breaks away from the body and moves downstream along the wake. The process repeats itself alternatively on the either side of the surface. The wake, thus, consists of vortices alternating in sign. The Gurney flap provides an off-surface fixed edge separation point for the pressure (lower) side of the shear layer. The suction side of the shear layer interacts with it to form the vortex street as depicted in Figure 5.

The Gurney flap decelerates the flow on the pressure (lower) side while the vortex shedding increases the suction on the suction (upper) side of the airfoil at the trailing edge. This phenomenon can be treated as a point vortex placed at the trailing edge, analogous to a violation of the Kutta condition at the trailing edge, which increases the total circulation around the wing, thus the lift. This causes the final pressure recovery to occur on an off-surface point as shown in Figure 3 and 4, thus increasing the effective chord length and the camber of the airfoil.

Gai and Palfrey²² have shown that the effectiveness of the Gurney flap is dependent upon the ratio of the height of the flap to the chord length and on the ratio of the velocity of the flow on the suction (upper) surface to the mean velocity of the pressure (lower) surface.

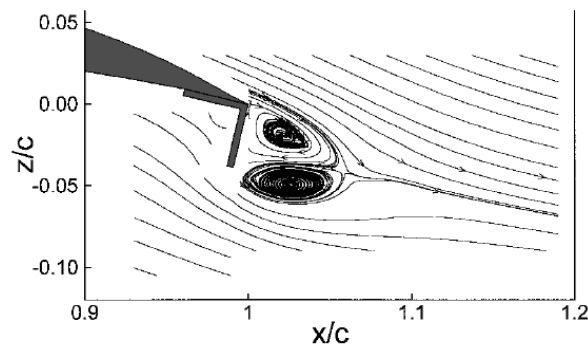


Figure 4. Time averaged LDA results of 4% Gurney at 0° angle of attack²⁰

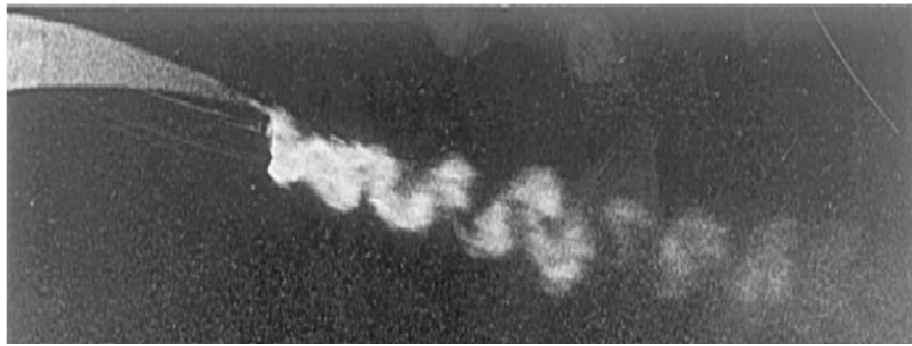


Figure 5. Flow over NACA 0012 with Gurney flap at 10 m/s and 0° angle of attack²⁰

The different mounting angles²³ of the Gurney flap have been shown to produce an augmentation of the lift coefficient when compared to an airfoil with no flaps. The lift increment becomes more significant at higher mounting angles from the lower surface of the airfoil. The experimental results²³ also show that airfoil stalls at a lower angle of attack, compared to an airfoil with no flap. The zero-lift angle of attack also reduces with the increase in the mounting angle.

Increasing the mounting angle of the flap also leads to a higher momentum deficit in the wake that causes an increase in drag coefficient. Use of an *edge* or “V” shaped Gurney flap²⁴ or splitter plate²⁵ with a varying mounting angle and height across

the span of the trailing edge may reduce the drag caused by the Gurney flap. These techniques attenuate the Von-Karman vortex-street by introducing three dimensional flows effects in the wake.

The application of the Gurney flap is an attractive alternative to the conventional aerodynamic control effectors. However, it needs moving parts for the “dynamic” control of the performance characteristics during the flight. An alternative approach to the Gurney flaps is the application of a jet flap. The jet flap works by ejecting a sheet of high velocity air at an angle from the trailing edge of the airfoil.

Analysis by Spence²⁶ explains that lift augmentation can be attributed to the effective lengthening of the airfoil at a moderate jet momentum coefficient and due to the inclined flow of the jet leading to the greater turning of the free stream flow, which is equivalent to a cambered airfoil.

Active flow control can be implemented either by the continuous or oscillatory blowing at the trailing edge²⁷⁻²⁸. An alternative approach for its implementation is the circulation control using a Coanda type trailing edge²⁹⁻³⁰. The experimental results have shown that these techniques can augment the lift significantly without a drag penalty during the cruise conditions for jet momentum coefficients that are practically realizable in an unmanned aerial vehicle. A preliminary study done by Traub³¹ shows that jet flap is capable of generating moments for the roll control authority in a $\frac{1}{3}$ scale Extra 330 model airplane. The Gurney/jet flap, thus, represents a proven technology that may be implemented for the active and stealthy control of an unmanned aerial vehicle.

Prior Work - Separation Control

The stall of an airfoil occurs because of the flow separation over the surface of the airfoil caused by the lack of momentum in the boundary layer flow to overcome the adverse pressure gradients.

Flow control technologies have been proven to be effective in reattaching the flow on the airfoils which otherwise would have stalled. A wide variety of passive control techniques¹⁻² have been used in the past to induce mixing that increases the amount of turbulence in the boundary layer to overcome the adverse pressure gradient. The development of the separation control devices has been well documented by Gad-el-Hak³²⁻³³. Various active flow control actuators, e.g. use of rotating cylinders to delay separation³⁴, moving surfaces³⁵⁻³⁶, steady blowing either tangentially to surface to increase the momentum of the boundary layer or normal to surface to increase the mixing rate³⁷, acoustic excitations³⁸, use of oscillating flaps for the periodic forcing of the flow³⁹⁻⁴⁰ have been investigated in past for the their effects on modifying the flow, controlling the flow separation over the bluff bodies and their success in improving the lift, drag and flight control parameters.

Flow manipulation using synthetic jet actuators or “net-zero mass flux” has gained a lot of acceptance over the conventional surfaces for the dynamic change in the pressure distribution over the airfoil surface⁴¹⁻⁴². In most of the efforts, the synthetic jet actuators are powered either by piezoelectric transducers⁴³⁻⁴⁴ or by pneumatic devices, external to the airfoil⁴⁵⁻⁴⁶.

Wu et al.⁴⁷ have documented the mechanism for the post stall control by using the periodic blowing-suction at the leading edge. In an unforced shear-layer, the shear-layer and the vortex shedding at the leading edge couple with each other at frequencies that are not harmonics of each other, leading to a random behavior of the separated flow.

The key parameter in the forced shear-layer separation control is the pulsation frequency of the forced blowing-suction. When done in the correct frequency range, the shear-layer shifts and locks-in with the pulsed jet frequency or one of its harmonics. This causes the shear-layer to roll up into discrete vortices, which then coalesce to form larger and stronger lifting vortices with a reduced frequency. This merging procedure enhances the mixing of the high momentum free stream fluid into the boundary layer, thus energizing it. As these vortices move downward, they interact with trailing edge vortices. Thus, it is possible to find a frequency range so that both the leading edge and trailing edge vortices can be modulated with a single pulsed blowing-suction. Increasing the pulsing frequency leads to the formation of smaller and close vortices. However, at excessive high frequencies, the rolling up coalescence of the vortices may be impaired.

For the realistic and full scale application of these technologies in an unmanned aerial vehicle, the active flow control devices should be modular, lightweight, compact and should have high power to weight ratio so that they can be embedded inside the control surface. The performance of an unmanned aerial vehicle⁴⁸, having piezoelectric transducer based synthetic jet actuators, was limited by low velocity amplitude generated by the actuators. Further, the performance deteriorated when the actuators were operated at frequencies away from the resonance frequencies.

The reciprocating piston based synthetic jet actuator⁴⁹⁻⁵² had been shown to be effective and self sufficient in comparison to the earlier designs. However, the actuator is heavy and its operating range is further limited as the jet momentum coefficient and the pulsation frequency are coupled with each other⁴⁹, making it unsuitable for its application in an airplane of the size comparable to 1/3 scale Extra 330 model airplane.

Research Procedure

An experimental investigation has been carried out for the evaluation of the effectiveness of the trailing edge Gurney/jet flap at low angle of attack on NACA 0015 at different jet velocities characterized by jet momentum coefficient.

To address the need of compact, lightweight, high power density and self-sufficient pulsed jet air blower, a new rotary actuator based pulsed blower has been developed. The effect of this device on the pressure, lift and drag over the angle of range on NACA 0015 will be discussed.

Based on the results of the above two experimental studies, the leading edge pulsed air blowing and trailing edge jet blowing are incorporated into the wings for 1/3 scale Extra 330 model airplane. The performance of the test vehicle has been experimentally determined in a low speed wind tunnel experimental study. The test methodology and the results will be discussed later in this thesis.

EXPRESSION OF UNCERTAINTY

An expression of uncertainty in any measurement is necessary to provide quantitative indication of the quality of the experimental results. The uncertainty, generally, consists of several components, grouped into two categories according to the way in which their numerical value is estimated⁵³⁻⁵⁴

Type A: Evaluated by statistical methods

Type B: Evaluated by other means, including previous measurement data, knowledge of the behavior and properties of the instruments, manufacturer's specifications, calibration certificates, and uncertainties assigned to reference data taken from handbooks.

The uncertainty estimates for the wind tunnel results presented here are based on the Recommendation 1(C1-1981) of the CIPM and Recommendation INC -1 (1980) of the working group on the statement of uncertainties convened by BIPM. The combined standard uncertainty, u_c , of an uncorrelated input quantities is the positive square root of the combined variance, $u_c^2(y)$ given by

$$u_c^2(y) = \sum_{i=1}^n \left(\frac{\partial f}{\partial x_i} \right)^2 u^2 \quad (1)$$

where f is a functional relationship between the measurand, Y and N other quantities x_1, x_2, \dots, x_N

$$Y = f(x_1, x_2, \dots, x_N) \quad (2)$$

The combined standard uncertainty $u_c(y)$ is an estimated standard deviation and characterizes the dispersion of the values that could be reasonably attributed to the

measurand, Y . In order to define an interval about the measurement result that may be expected to cover a large fraction of the distribution of values that could be easily attributed to the measurand is termed as expanded uncertainty and is obtained by multiplying the combined uncertainty by a coverage factor, k

$$U = ku_c(y) \quad (3)$$

The value of the coverage factor, k , is based on the level of confidence required. In general, the value of k is two for a level of confidence of approximately 95%. The result of measurand is expressed as:

$$Y = y \pm U \quad (4)$$

This may be interpreted as the best-estimated value of the measurand Y is y and that $y-U$ to $y+U$ is an interval that may be expected to cover a large fraction of the distribution of the values that could be reasonably attributed to Y . The uncertainty in the measurement of various measurands has been mentioned in the entire thesis, where required.

TRAILING EDGE JET BLOWING

General

This section presents the effect of the trailing edge Gurney/jet flap on the aerodynamic performance characteristics of a NACA 0015 airfoil. The experimental procedure and analysis of the results follow.

Setup and Procedure

The wind tunnel tests were carried out in Texas A&M University 1 ft by 1 ft open circuit wind tunnel to investigate the effectiveness of the jet flap in conjunction with the Gurney flap. The tests were done on a comparative basis with respect to the baseline wing (no jet actuation/Gurney flap). Thus, the wall effects and the correction factors for the streamline curvature and solid blockage had not been estimated.

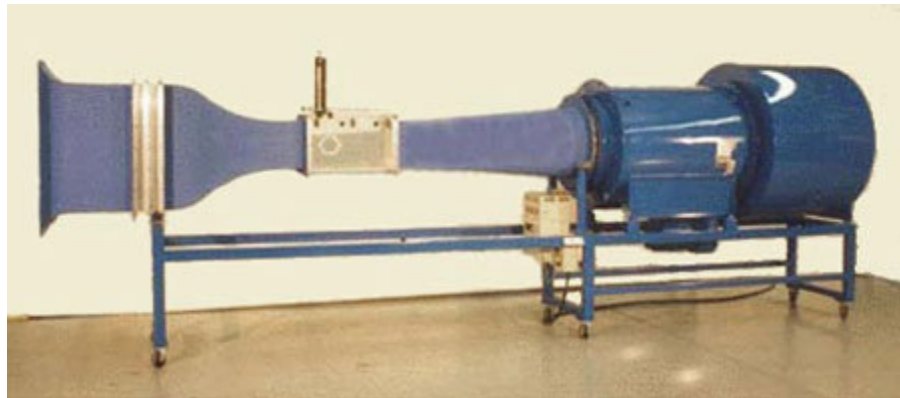


Figure 6. 1 ft by 1 ft wind tunnel facility at Texas A&M University

The test wing was based on the NACA 0015 profile, representing the wing profile of a $\frac{1}{3}$ scale Extra 330 model airplane. The test wing was rapid prototyped from acrylonitrile butadiene styrene (ABS) plastic. The wing had a chord length of 122.50

mm and a span of 140 mm. The projected flap height, normal to the surface, was limited to 1.0 mm (a 0.75% Gurney flap) and such that the flap remained in the boundary layer to retain its effectiveness as shown by Gai and Palfrey²² and Traub et.al.²⁴. Further, it had been inclined at 20° from the vertical to reduce the drag penalty associated with the Gurney flap. The jet exit had an opening of 1.28 mm.

The baseline wing with no jet/Gurney flap was made by smoothing the pressure side (lower surface) using clay, resulting in a blunt trailing edge. A blunt trailing edge was preferred over the sharp trailing edge as the model was designed on the wing geometry of a 1/3 scale Extra 330 model airplane, which has a blunt trailing edge.

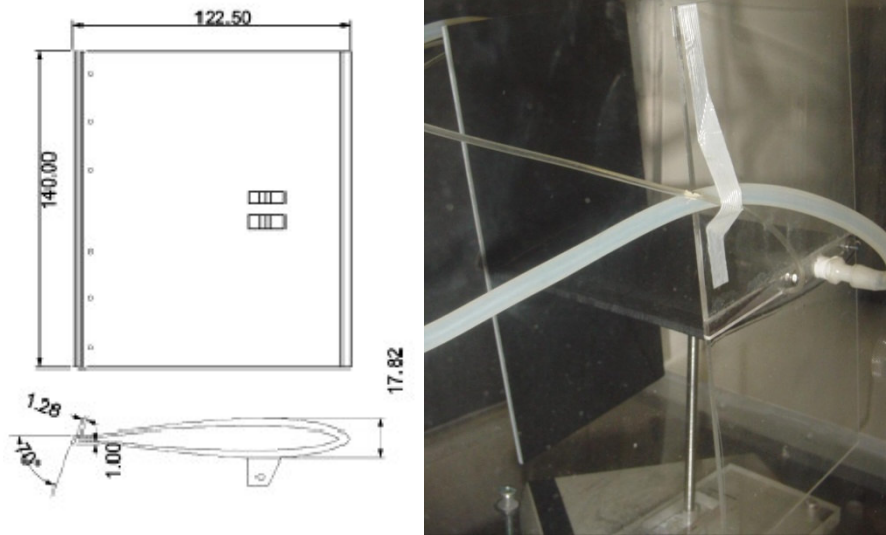


Figure 7. Specifications of the trailing edge jet blowing experimental setup

In order to reduce three-dimensional flow effects, clear acrylic side plates, 122 mm by 246 mm in size, were installed at the end of the wing. However, the flow was not completely two dimensional, due to the limited extent of the side plates. The angle of

attack was measured at the chord line of the wing using a digital inclinometer. The digital inclinometer had a resolution of 0.01° and an accuracy of $\pm 0.05^\circ$ in the operating range of 0° to 9.99° . Because of low aerodynamic loads, a high-resolution Setra -4100D force balance was used. The balance had a resolution of 0.01 gram and an accuracy of 0.02 gram over an operating range of 0-4000 grams. The relative expanded uncertainty in the measurement of the lift coefficient at 95 % confidence level was 3%.

Compressed shop air was used to supply the required amount of air to the jet. The supply pressure was regulated by using a British standard 1042 orifice plate⁵⁵. For the results presented in this study, the jet momentum coefficient was calculated using the maximum value of the flow velocity exiting the jet. The expression that defines the jet momentum coefficient is

$$C_\mu = \frac{2(\rho h u^2)_{jet}}{(\rho c u^2)_{freestream}} \quad (5)$$

where, ρ is the fluid density, h is the width of the jet exit, u is the velocity and c is the chord length of the airfoil. The jet momentum coefficients used during the experiment were such selected that could be practically realizable in the future test flights.

The internal cavity in the wing acted as a settling chamber/plenum before the air ejected from the trailing edge. The internal cavity was pressure tapped. The plenum pressure was used to estimate the exit jet velocity. The pressure and velocity measurements were done using FlowkineticsTM FKS 1 DP-PBM manometer with an accuracy of 0.1 %. The comparison between the direct measurement of the exit jet velocity using the stagnation probe and the estimated velocity using plenum pressure indicated an error of less than 1.5%. The jet exit at the trailing edge was surveyed with a

stagnation probe to determine the span wise flow uniformity, and was determined to be within 5% of the set velocity. The relative expanded uncertainty in the measurement of the jet momentum coefficient, C_{μ} was 5% at 95% confidence level.



Figure 8. Flow visualization of the trailing edge jet blowing

To mitigate the effect of additional loading due to the external tubing supplying the pressurized air to the setup, flexible silicone based tubing were used. Tare test readings were also undertaken to measure the transmitted loads over the entire angle of attack range. The data indicated that loads were very low.

The tests were carried out for an angle of attack envelope from -5° to 5° at a free stream velocity of 20 m/s yielding a chord based Reynolds number of 160,000. The model was pitched about its quarter-chord location. The angle of attack envelope was limited to 5° because of the limited weighing range of the force balance. The jet velocity was selected to yield a jet momentum coefficient, C_{μ} in the range of 0 to 0.032. Additionally, wake surveys were also conducted at two chord lengths downstream of the trailing edge using a pitot static tube. The complete test matrix is shown in Table 1.

Table 1. Test matrix for jet/Gurney flap characteristics on aerodynamic performance

| C_μ | 0 | 0 | 0.004 | 0.008 | 0.016 | 0.032 |
|-----------------|---------------------|------------------|-------|-------|-------|-------|
| Angle of Attack | without Gurney Flap | with Gurney Flap | | | | |
| -5.24° | x o | x o | o | x o | o | x o |
| -3.43° | x o | x o | o | x o | o | x o |
| -1.6° | x o | x o | o | x o | o | x o |
| 1.1° | x o | x o | o | x o | o | x o |
| 2.2° | x o | x o | o | x o | o | x o |
| 5.2° | x o | x o | o | x o | o | x o |

o Lift data
x Wake Survey Conducted

Results and Discussions

The measured lift coefficient is defined as

$$C_l = \frac{\text{Lift}}{(\frac{1}{2}\rho u^2)_{\text{free stream}}} \quad (6)$$

and plotted as a function of angle of attack as shown in Figure 9. The results clearly show the effective lengthening and cambering of the airfoil as discussed earlier. The flow effectors are able to shift the lift coefficient such that zero-lift angle of attack is negative. The effect of the jet flap on the slope of the curve is in the range of 0.08/degree and is very nominal. The analysis done by Spence²⁶ suggests a theoretical 3% increase in the slope of the lift curve for a similar jet momentum coefficient. The effectiveness of the jet actuators has been calculated in terms of lift augmentation ratio (LAR) defined as

$$LAR = \frac{C_{l, \text{jet flap}} - C_{l, \text{Gurney flap}}}{C_\mu} \quad (7)$$

A lift augmentation ratio greater than zero indicate that the lift increment is only due to the jet actuation. An increase in the jet momentum coefficient do increases the lift coefficient as shown in Figure 10, however, at a decreasing rate. Thus, a low jet

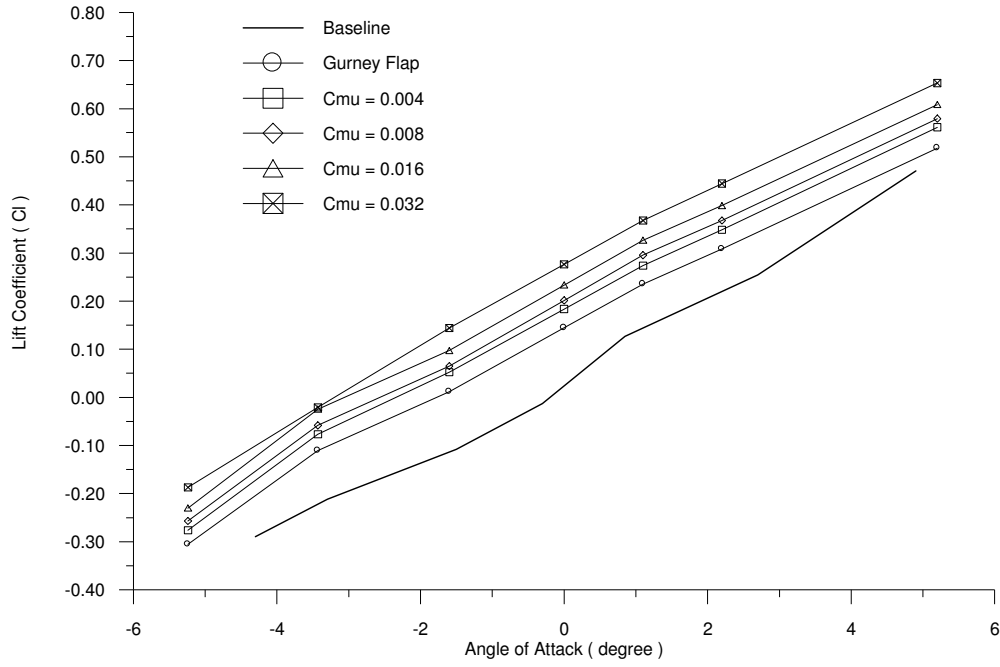


Figure 9. Measured variation of lift coefficient with angle of attack

momentum coefficient is more effective in increasing the lift. The curve fitting of the LAR data shows a C_μ dependency as

$$LAR = 1.007C_\mu^{-0.41} \quad (8)$$

The increment in the 0° angle of attack lift coefficient has a dependency to $\sqrt{C_\mu}$. Additionally, the results also show that the negative shift in zero-lift angle of attack is proportional to $\sqrt{C_\mu}$ and inversely to the slope of C_l vs. angle of attack curve.

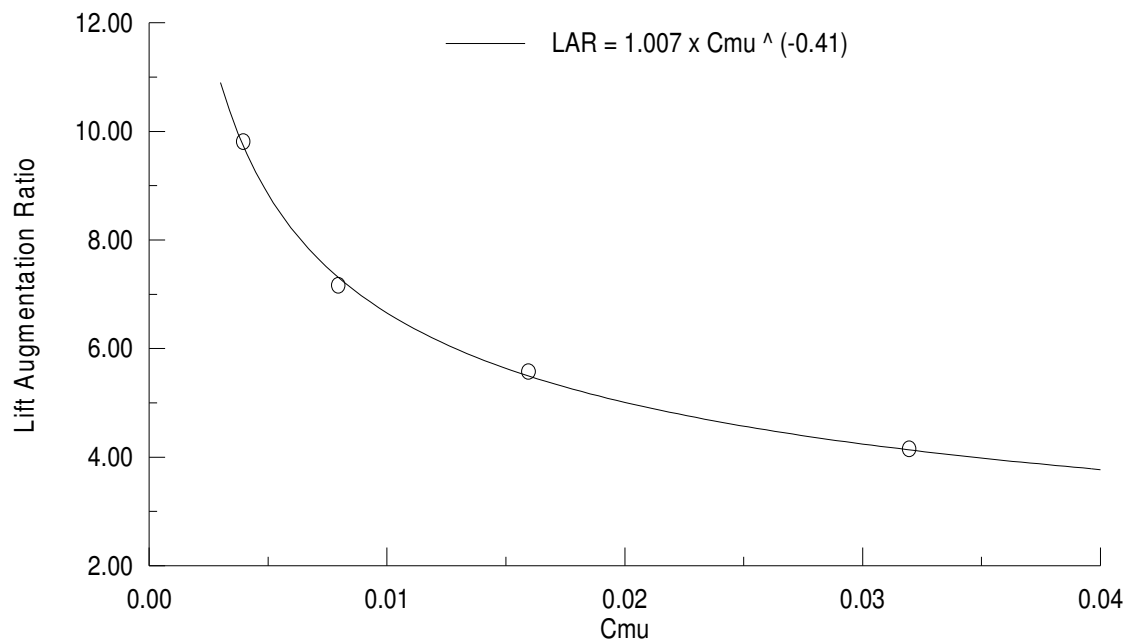


Figure 10. Variation of lift augmentation ratio with C_{μ} at 0° angle of attack

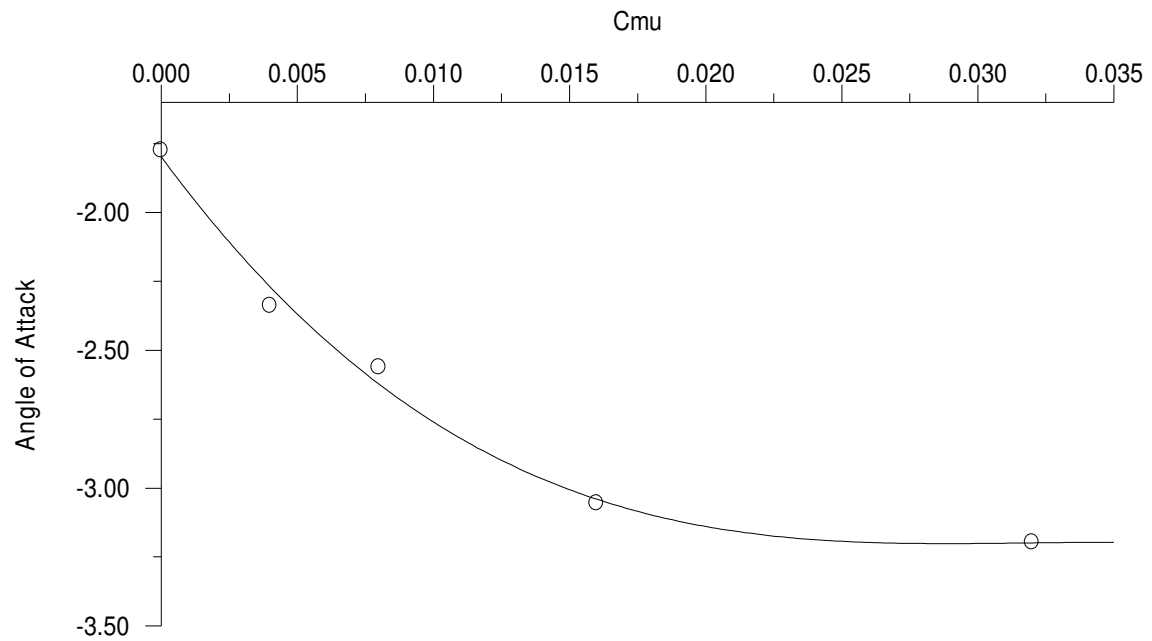


Figure 11. Variation of zero lift angle of attack with C_{μ}

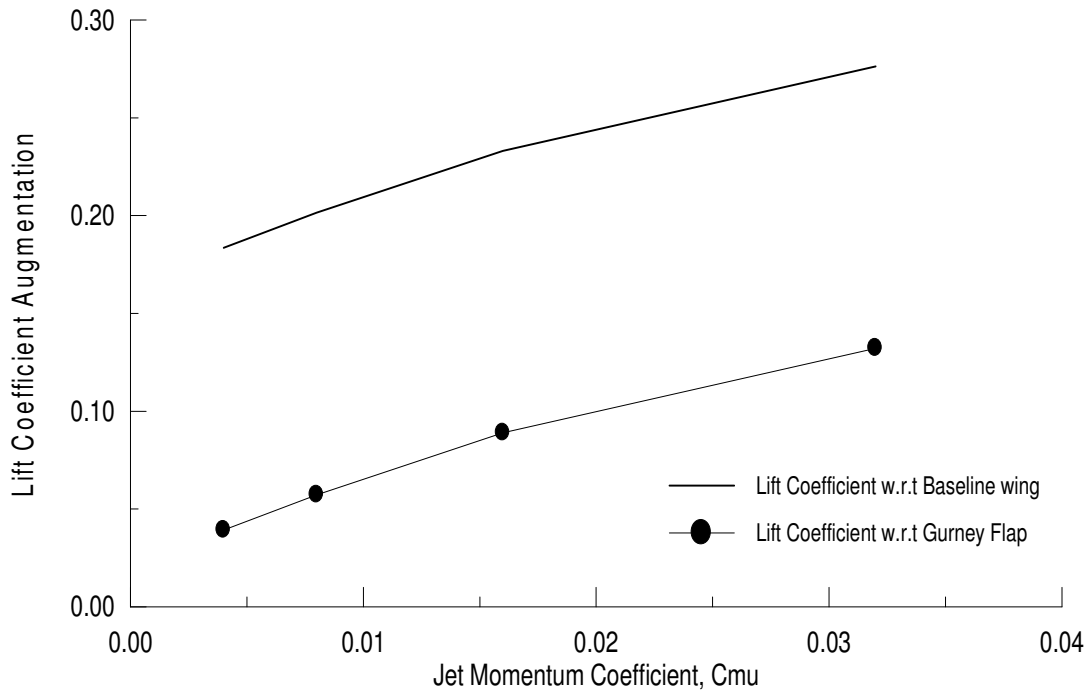


Figure 12. Variation of lift coefficient with C_{μ} at 0° angle of attack

Wake Survey

The effect of the jet flap on the wake was evaluated by the wake surveys conducted at two chord lengths downstream of the trailing edge using a pitot static tube at an increment of 1/12 inch. The survey was done as far as from the trailing edge to render the static pressure effects from that of the upstream of the model negligible, an assumption made by Jones⁵⁶. The application of the momentum principle indicates that the drag on the airfoil in the flow should be equal to the reduction in the linear momentum of the flow. The drag may be estimated as suggested by Pope and Rae⁵⁷.

$$C_d = \frac{2}{c} \int_{y_1}^{y_2} \left(\sqrt{\frac{q}{q_0}} - \frac{q}{q_0} \right) dy \quad (9)$$

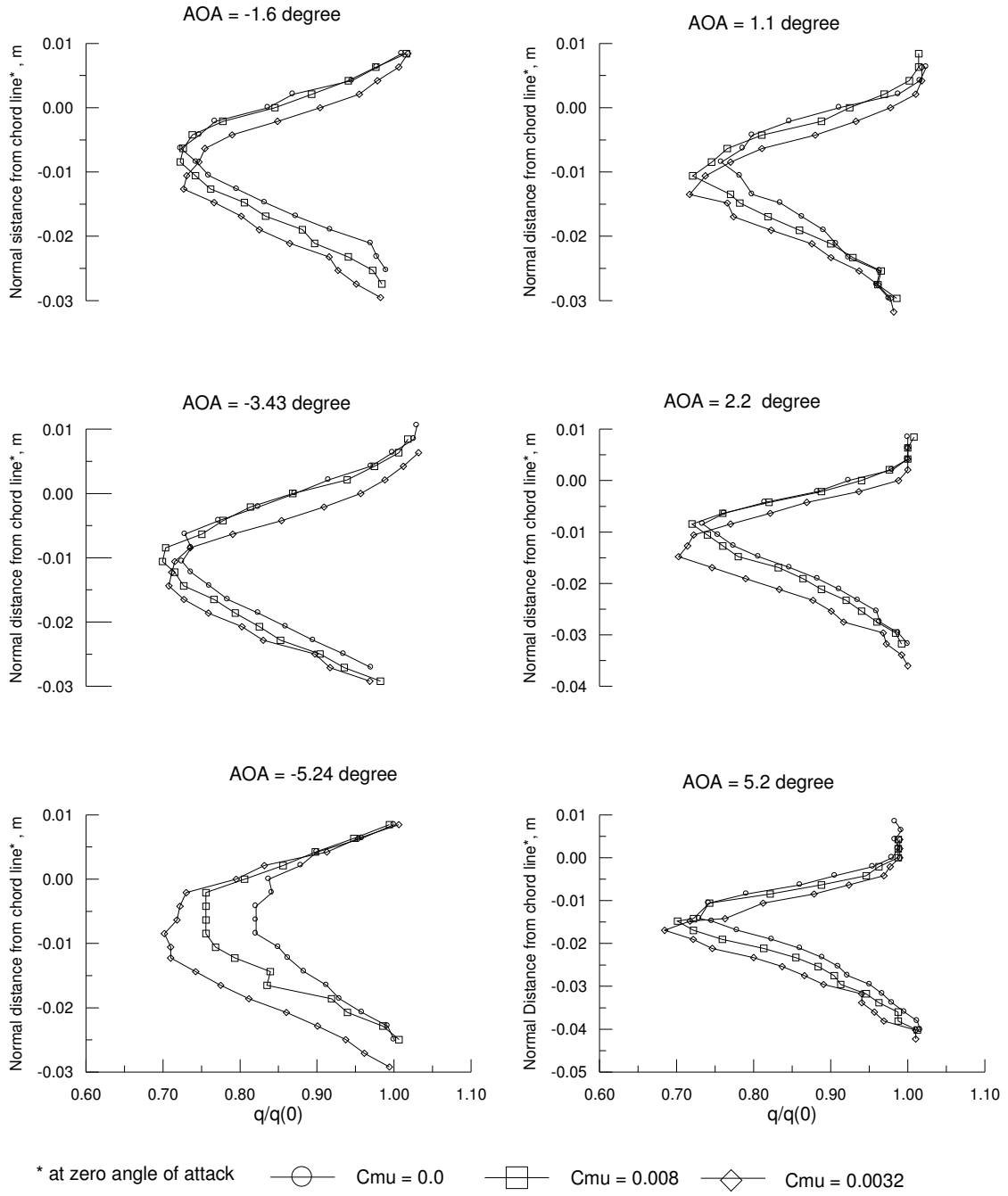


Figure 13. Wake surveys conducted at two chord lengths downstream of the trailing edge

where, c is the chord length of the airfoil, y_1 and y_2 are the integration bound of the wake, q is the dynamic pressure and q_0 is the dynamic pressure of the free stream.

Figure 13 shows the result of the wake surveys for test conditions as mentioned earlier in Table 1. The data show that the jet flap increases the wake width and maximum velocity deficit. Further, the wake position in all the test cases for a given angle of attack is lower than the trailing edge, which explain the higher lift generated by the jet blowing. The plots also reflect the asymmetrical nature of the wake deficit, the wake deficit being larger below the maximum velocity, indicating a formation of vortex street downstream of the jet.

Figure 14 shows the profile drag integrated from the velocity profile. The results indicate that all the jet/Gurney flap combinations have recorded a lower drag than the baseline wing. The drag coefficient has increased for test condition with a jet momentum coefficient greater than zero. The increase in the drag is due to the formation of regulated pattern of the vortex-street⁵⁸.

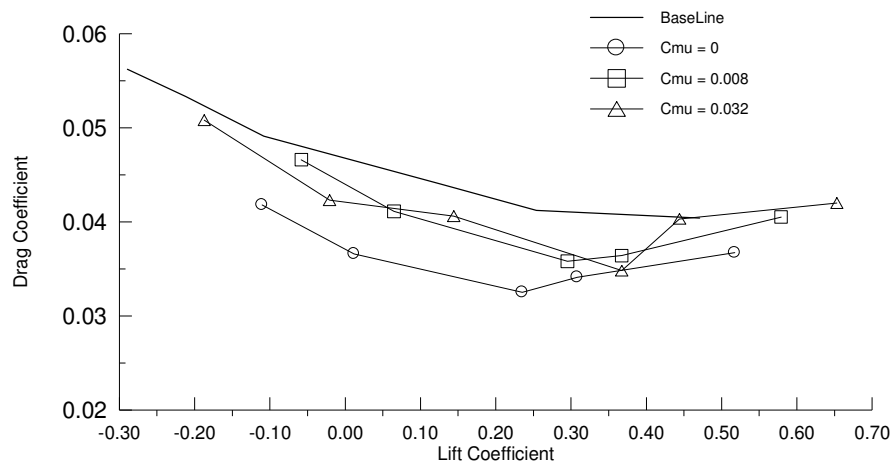


Figure 14. Effect of jet flap on measured drag coefficient

LEADING EDGE PULSED BLOWING

General

This section presents the effect of the leading edge pulsed blowing on the aerodynamic performance characteristics of a NACA 0015 airfoil. The experimental procedure and analysis of the results follow.

Pulser Design

Prior study done by Seifert and Pack⁴⁴ has indicated that in order to benefit from a synthetic jet actuator/pulsed blowing, there must be one to four vortices produced over the airfoil surface at any given time. Seifert has also shown that the most efficient excitation corresponds to the synthetic jet actuator/pulsed blowing at an optimal non-dimensional frequency of about one. The non-dimensional frequency, F^+ is derived from the Strouhal number and is defined as

$$F^+ = f \frac{x_{te}}{U_\infty} \quad (10)$$

where, f is the pulser frequency, x_{te} is the distance of the pulser from the trailing edge and U_∞ is the free stream velocity. The jet momentum coefficient, defining the relationship between momentum of the jet exiting the slot and the momentum of the free stream is

$$C_\mu = \frac{2 h_{slot} U_{slot}^2}{c U_\infty^2} \quad (11)$$

where, h_{slot} is the width of the slot, U_{slot} is the average jet velocity at the slot exit, c is the characteristic length (chord length of the airfoil) and U_∞ is the free stream velocity.

A small modular rotary valve based pulsed blower mechanism is designed and rapid prototyped. The air entered into the centrifugal impeller axially. The horizontal

arrow in Figure 15 shows the exit location of pulsed jet. A rotating shaft with a through slot generates a pulsed jet. The velocity profile generated by the pulser exhibited a near sinusoidal velocity profile as shown in Figure 16. The frequency of the pulsed jet air has been observed to be nearly twice the pulser frequency. The new design has many potential advantages for its application in the current configuration.

- 1) The inlet region provides localized suction for boundary layer control.
- 2) The exit can be either continuous or pulsed blowing for additional flow control
- 3) Jet momentum coefficient and pulsing frequency are decoupled, a significant advantage allowing optimal tailoring specific to the application.
- 4) The actuator is highly compact, localized and operates in a stand-alone fashion.
- 5) The blower functions in a high backpressure environment as is present when providing high velocity fluid through a narrow slot.

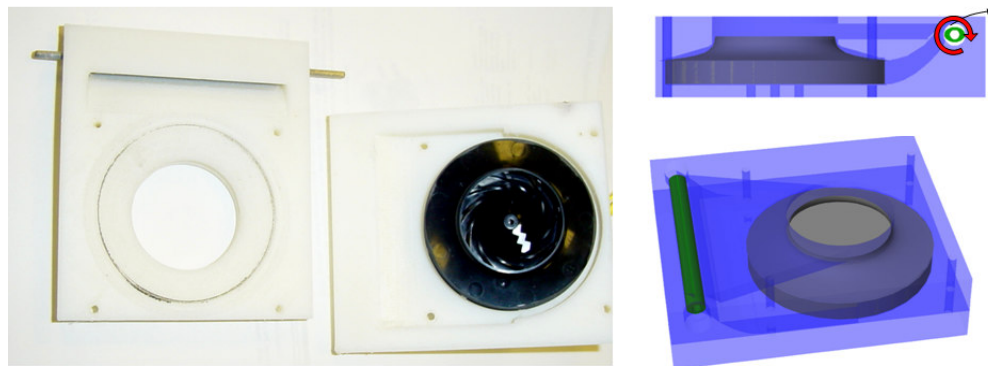


Figure 15. Centrifugal fan based pulsed blower

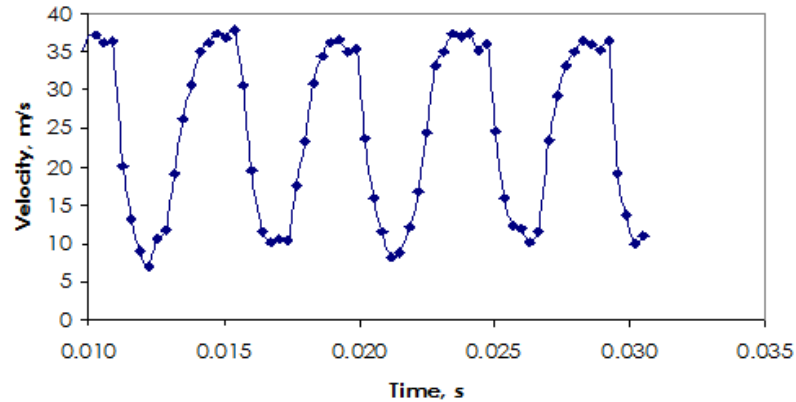


Figure 16. Velocity profile of pulsed air at fan speed of 6000 rpm and a frequency of 225 Hz

Wing Model

In order to test the separation control capability and the performance of the proposed actuator, a wind tunnel model was rapid prototyped from acrylonitrile butadiene styrene (ABS) plastic. NACA 0015 profile was selected because it matched the wing profile of $\frac{1}{3}$ scale Extra 330 model airplane. The wing was equipped with end plates to reduce the three-dimensional effects. The model wing had five pulser valves for the jet exit at every 10% of the chord length location from the leading edge. The pulser shaft was machined from a 6.35 mm diameter Aluminum rod with a 3.18 mm through slot. The pulser shaft was supported in the valve housing using a ball bearing on each end. The pulser shaft was driven by a belt drive mechanism powered by a 12 V DC brushless motor. The specifications of the test setup are given in Table 2. A computer based servo controller board was used to generate the pulse width modulated signal for the brushless motor. The servo controller board takes serial command from a Labview[®] based program as an input and produces the corresponding pulse width modulated signal

with a resolution of $1\mu\text{s}$. The speed of the pulser shaft was monitored using an optical tachometer. Repeated measurements of the pulser frequency suggested an accuracy of $\pm 1\text{ Hz}$ of the set frequency. Figure 17 shows the CAD model of the wing with pressure tapings and the location of the pulser housings.

Table 2. Specification of the experimental setup for pulsed blowing

| | |
|---|--|
| Wing Profile | NACA 0015 |
| Weight of the test setup | 4000 g |
| Chord of the test wing | 310 mm |
| Span of the test wing | 220mm |
| End plate size | 310 mm \times 690 mm (centered with chord of the wing) |
| Center of gravity along the chord | 159.6 mm from trailing edge |
| Center of gravity along the length of the end plate | 304.5 mm from the lower surface |
| Number of exit slot openings and pulser valve | 5 at every 10% from leading edge |
| Length of valve | 200 mm |
| Width of exit slot | 1.5 mm |

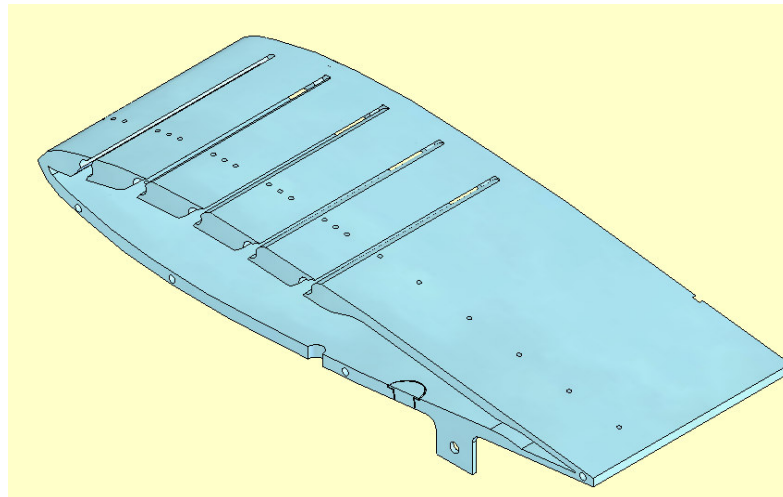


Figure 17. NACA 0015 profile based wind tunnel model



Figure 18. Leading edge pulsed air blowing experimental set up in 3 ft by 4 ft wind tunnel

The wing was designed for the easy installation on a three-component pyramidal balance as shown in Figure 18. The wing surface was pressure tapped with 22 pressure ports on the upper surface and 10 pressure ports on the lower surface. The pressure ports were connected via Tygon[®] tubing of equal length to a 32-channel electronically scanned pressure transducer. Table 3 shows the location of the pressure ports on the wing.

Table 3. Location of pressure ports on the wind tunnel model

| Upper Surface | | | | Lower Surface | |
|---------------|--------------|-------------|--------------|---------------|--------------|
| Port Number | x/c Location | Port Number | x/c Location | Port Number | x/c Location |
| 1 | 0 | 12 | 0.34 | 23 | 0.05 |
| 2 | 0.02 | 13 | 0.36 | 24 | 0.1 |
| 3 | 0.04 | 14 | 0.42 | 25 | 0.2 |
| 4 | 0.06 | 15 | 0.44 | 26 | 0.3 |
| 5 | 0.12 | 16 | 0.46 | 27 | 0.4 |
| 6 | 0.14 | 17 | 0.52 | 28 | 0.5 |
| 7 | 0.16 | 18 | 0.59 | 29 | 0.6 |
| 8 | 0.22 | 19 | 0.68 | 30 | 0.7 |
| 9 | 0.24 | 20 | 0.77 | 31 | 0.8 |
| 10 | 0.26 | 21 | 0.86 | 32 | 0.9 |
| 11 | 0.32 | 22 | 0.95 | | |

The inside of the wing acted as a large settling chamber for air supply to the pulsed blower. During the wind tunnel tests, the plenum pressure was regulated by a British standard 1042 orifice plate⁵⁵ to the desired jet velocity. The compressibility effects of the air in the plenum with the pulser actuation were investigated and the jet exit velocity was calibrated to the plenum chamber pressure for the 10%, 30%, and 50% chord length location of the pulser from the leading edge. The pressure and velocity measurements were done using FlowkineticsTM FKS 1 DP-PBM manometer with an accuracy of 0.1 %. The loss coefficient k , defined as

$$k = \frac{P_0 - 0.5 \times \rho \times U_{jet}^2}{0.5 \times \rho \times U_{jet}^2} \quad (12)$$

where, P_0 is the stagnation pressure and U_{jet} is the jet velocity. The losses were in the range of 2%, 5%, and 9% for pulser at 10%, 30%, and 50% chord location from the leading edge (Figure 19).

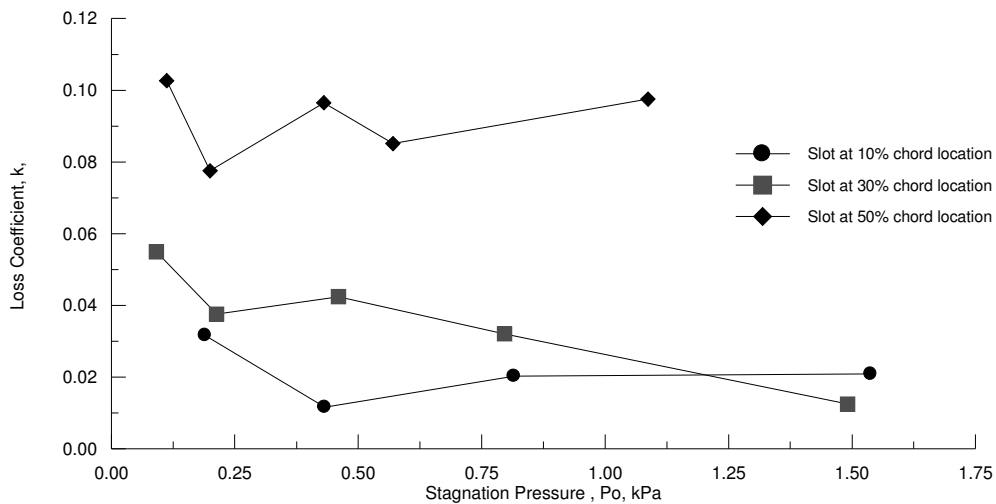


Figure 19. Effect of pulser location on loss coefficient, k

The behavior of the leading edge pulser was studied in a standalone condition to evaluate its performance as a function of non-dimensional pulser frequency, F^+ and the jet momentum coefficient, C_{μ} . Constant temperature hotwire anemometry was used for the characterization of the jet velocity. The hotwire was placed at the entrance of the jet and the velocity profile was recorded for different values of F^+ and C_{μ} . Single film type TSI Inc. 1201 hotwire probe and TSI IFA 300 thermal anemometer system were used. The hotwire was calibrated using TSI 1125 probe calibrator while monitoring the pressure from a FlowkineticsTM FKS 1 DP- PBM manometer. The data were acquired using a Labview[®] based program and a 14-bit data acquisition card. The calibration curve was obtained by using a least square fourth order curve fitting between the known air velocity and the bridge voltage measured by the hotwire. Figures 20 and 21 show the normalized time and velocity graph for the two jet locations. The velocity profile is nearly sinusoidal with little effect due to frequency or the jet momentum coefficient. The span wise flow uniformity was found to be within 90% of the set velocity.

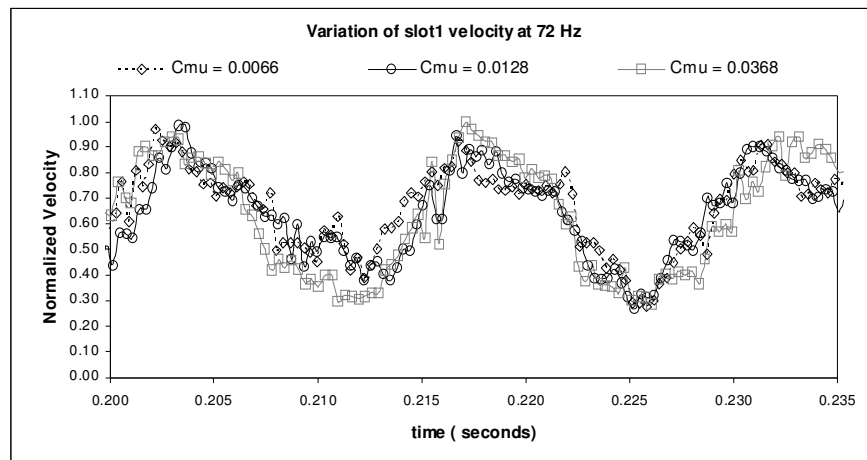


Figure 20. Exit velocity profile at $x/c = 0.1$ at pulsed air frequency of 72 Hz

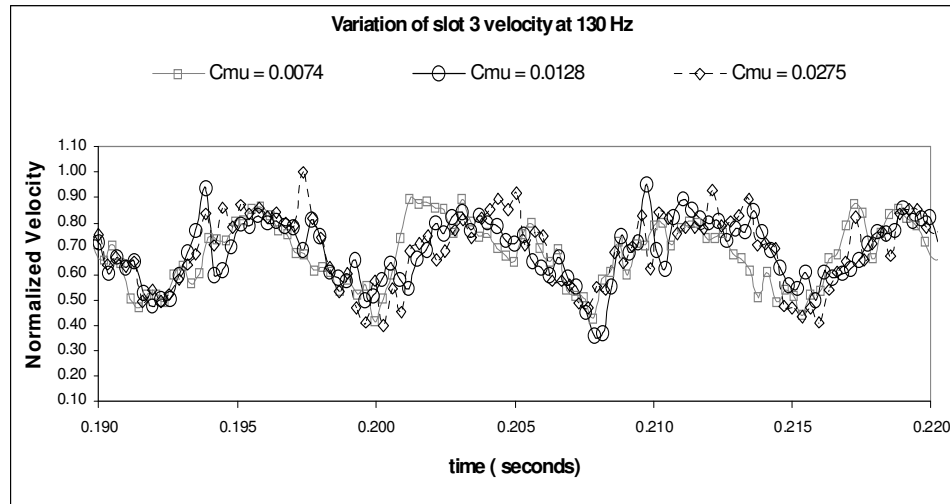


Figure 21. Exit velocity profile at $x/c = 0.5$ at pulsed air frequency of 130 Hz

Wind Tunnel Facility

The aerodynamic performance tests were conducted at Texas A&M University's 3 ft by 4 ft wind tunnel facility at a free stream velocity of 20 m/s, yielding a Reynolds number of 4.2×10^5 based on model chord length. A three-component pyramidal balance was used for the force and moment measurement. The pyramidal balance can measure a maximum drag force of 50 lb and a maximum lift force of 100 lb.

The two forces (lift and drag) as well as pitching moment were measured directly by three strain gauge load cells. The output voltages were measured using a 16-bit A/D board. The balance calibration was checked, using the proof loads, before the experiments and its accuracy was estimated at 0.6% of the full scale for lift, drag and pitching moment.

The wind tunnel turbulence intensity had previously been measured and was found to be less than 0.3%, assuming isotropic turbulence. The flow angularity for this

facility was less than 0.25° . The free stream velocity was measured using a wall mounted Pitot tube with a tip diameter of 3.175 mm. The pressure and velocity measurement were done using FlowkineticsTM FKS 1 DP-PBM manometer with an accuracy of 0.1 %. Wind tunnel corrections for solid and wake blockage were applied using the methodology described in Rae and Pope⁵⁹.

Dedicated software has been written for the acquisition and reduction of the external force balance data. The relative expanded uncertainty in the measurement of the lift and drag coefficient at confidence level of 95 % was 2%.

The pitch angle of the model was changed by using a stepper motor, which was connected to a worm gear mechanism. An optical encoder was connected to the mechanism and its output was fed to a digital read out display. The stepper motor, capable of generating a torque of 5 N-m, was controlled by a micro LYNX[®] 4/7 micro stepping motor controller. The stepper motor had 200 steps per revolution, wherein the micro LYNX[®] allowed micro-stepping up to 51,200 steps per revolution.

The pitching strut was attached to the model through a bronze sleeve near to the trailing edge of the wing. The model angle of attack could be adjusted within an accuracy level of 0.05° at its quarter-chord location. The model was pitched through an angle of attack range of 0.4° to 27.4° . Data were typically recorded at 2° intervals except in the region of the maximum lift coefficient, where a 1° interval was used.

The on-surface flow visualization was done using titanium dioxide suspended in a mixture of kerosene, linseed oil, and oleic acid. In addition to this, tufts were also

placed on the upper surface of the wing. Video and digital images were taken during these tests and were analyzed subsequently to determine the flow field characteristics.

Surface pressure measurements were also done for an angle of attack range of 0.4° to 27.4° at a free stream velocity of 20 m/s. The surface pressures were measured using a 32-channel electronically scanned pressure transducer (ESP) with a range of ± 2.5 kPa. The ESP was calibrated using a reference pressure imposed on the each channel of the ESP. The reference pressure was measured from FlowkineticsTM FKS 1 DP-PBM manometer. The agreement of the two pressures was within 1%. The flow was allowed to stabilize for 5 seconds over the model once the test conditions were changed (i.e., change in the pulser frequency, flow rate or the angle of attack) before the data acquisition. Further, ESP was re-zeroed after every test to reduce the drift. The measured pressures readings were digitized using a 12-bit Analog to Digital board.

Wind Tunnel Test Matrix

The experiments were conducted for the pulser location at 10%, 30% and 50% of the chord location from the leading edge. The jet was emanating from only one slot while the remaining were covered with a vinyl tape to avoid any leakage of the flow. The data from the pyramidal balance and ESP were recorded at F^+ of 0, 0.5, 1.0, and 1.5 and C_μ of 0.0075, 0.015, and 0.0275. For the pulser at 50% chord location, the tests were conducted at C_μ of 0.019 instead 0.0275, because of low pneumatic pressure. The relative expanded uncertainty in the measurement of the jet momentum coefficient, C_μ and F^+ was 5 % and 0.5% at 95% confidence level.

Force Balance Results

Figures 22 to 25 present the effect of the leading edge pulser on the aerodynamic performance of the wing. The results have been presented for same C_{μ} while varying F^+ for three pulser locations in the wind axes, body centered coordinate system. The results show that at lowest jet momentum coefficient, C_{μ} , of 0.0075 steady blowing as well as pulsed blowing has a negative effect on the lift coefficient. A drop in the lift has been observed for most of the cases. Increasing the jet momentum coefficient causes an increase in the lift generated by the airfoil when compared to non-actuated wing. Delay in the onset of flow separation has been observed with an increase in pulser frequency. However, any increase in F^+ beyond one has no significant effects on the lift increment at higher jet momentum coefficients.

The results also indicate that pulsed air actuation at 50% chord location causes a more abrupt stall than the base wing. While the actuation at 10% chord length showed a more docile stall, it is also apparent that the jet blowing at 10% chord location shows an initial “rounding” of the lift curve at approximately 15° . The rounding of the lift curve gives an indication of the gradual thickening of the trailing edge boundary layer and a slow upstream progression of the separation location, leading to a docile stall. It may be because the pulsed jet is able to effectively organize the separated shear layer into coherent structures and keep it in a closer proximity to the surface of the airfoil.

Figures 26 to 30 compare the effect of increasing C_{μ} at constant F^+ for the three locations. The results also indicate that higher jet momentum coefficients lead to higher lift coefficients for all the jet actuation conditions.

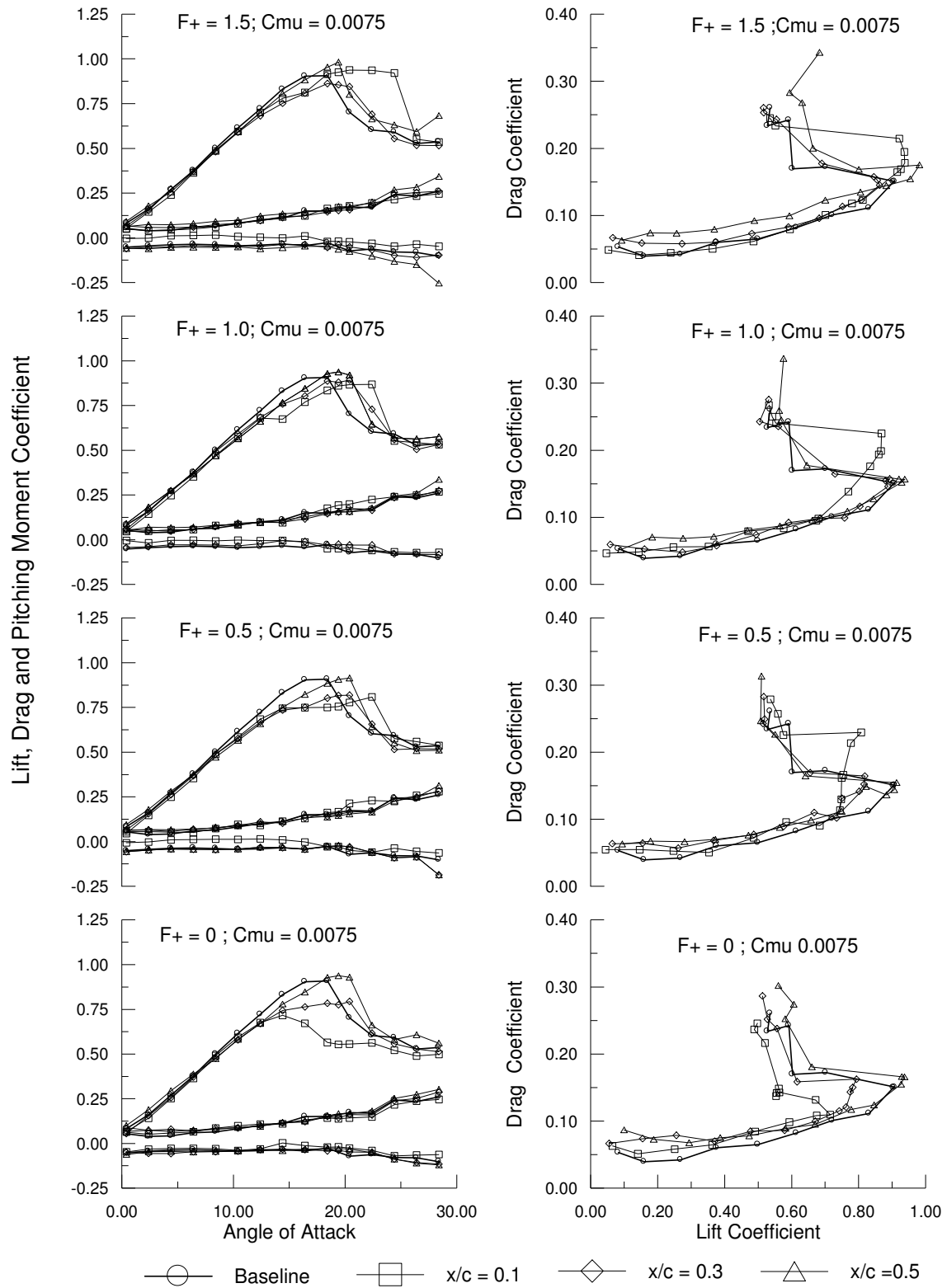


Figure 22. Performance curves of L.E. pulsed blowing at constant $C_{\mu} = 0.0075$

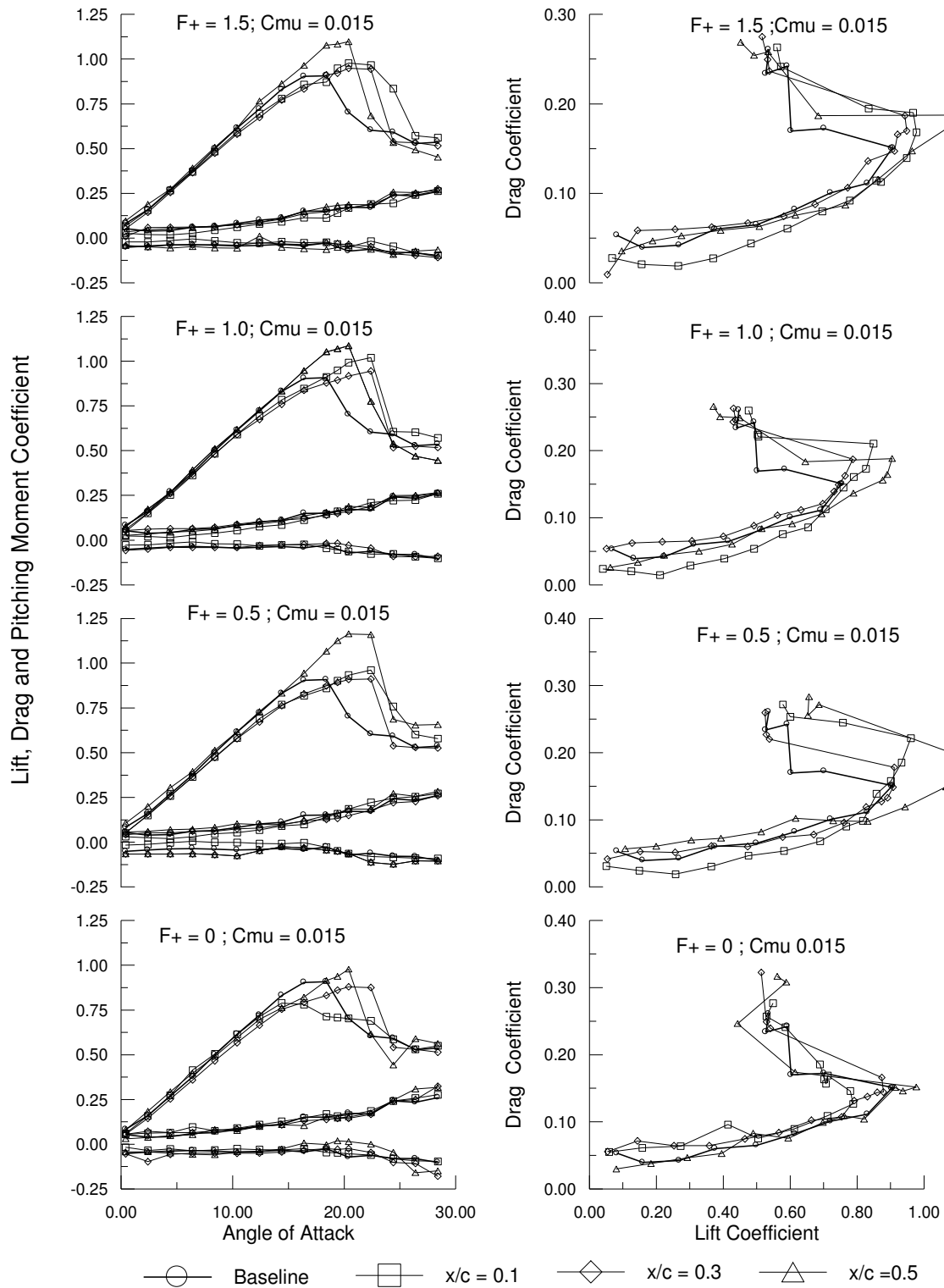


Figure 23. Performance curves of L.E. pulsed blowing at constant $C_{\mu} = 0.015$

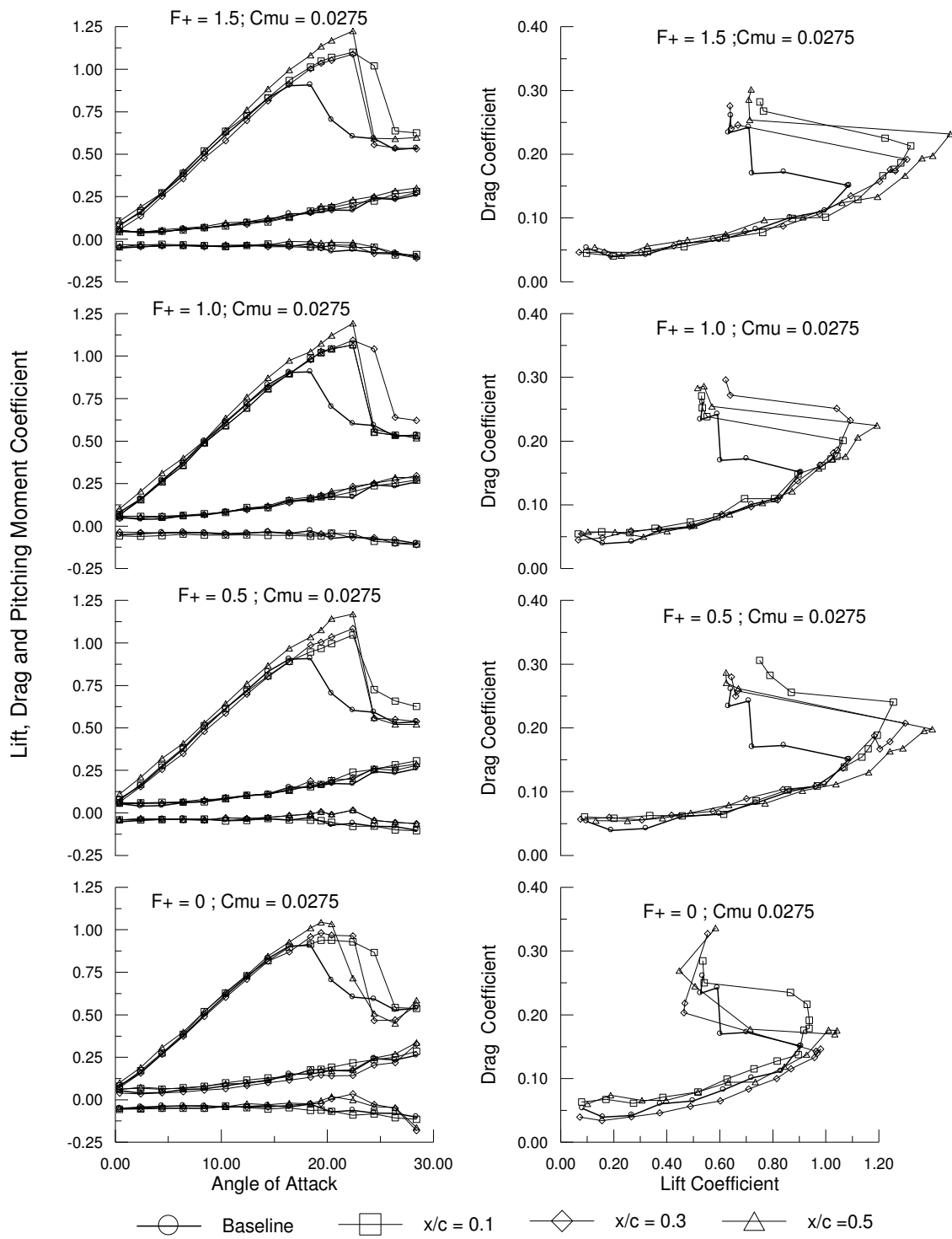


Figure 24. Performance curves of L.E. pulsed blowing at constant $C_{\mu} = 0.0275$

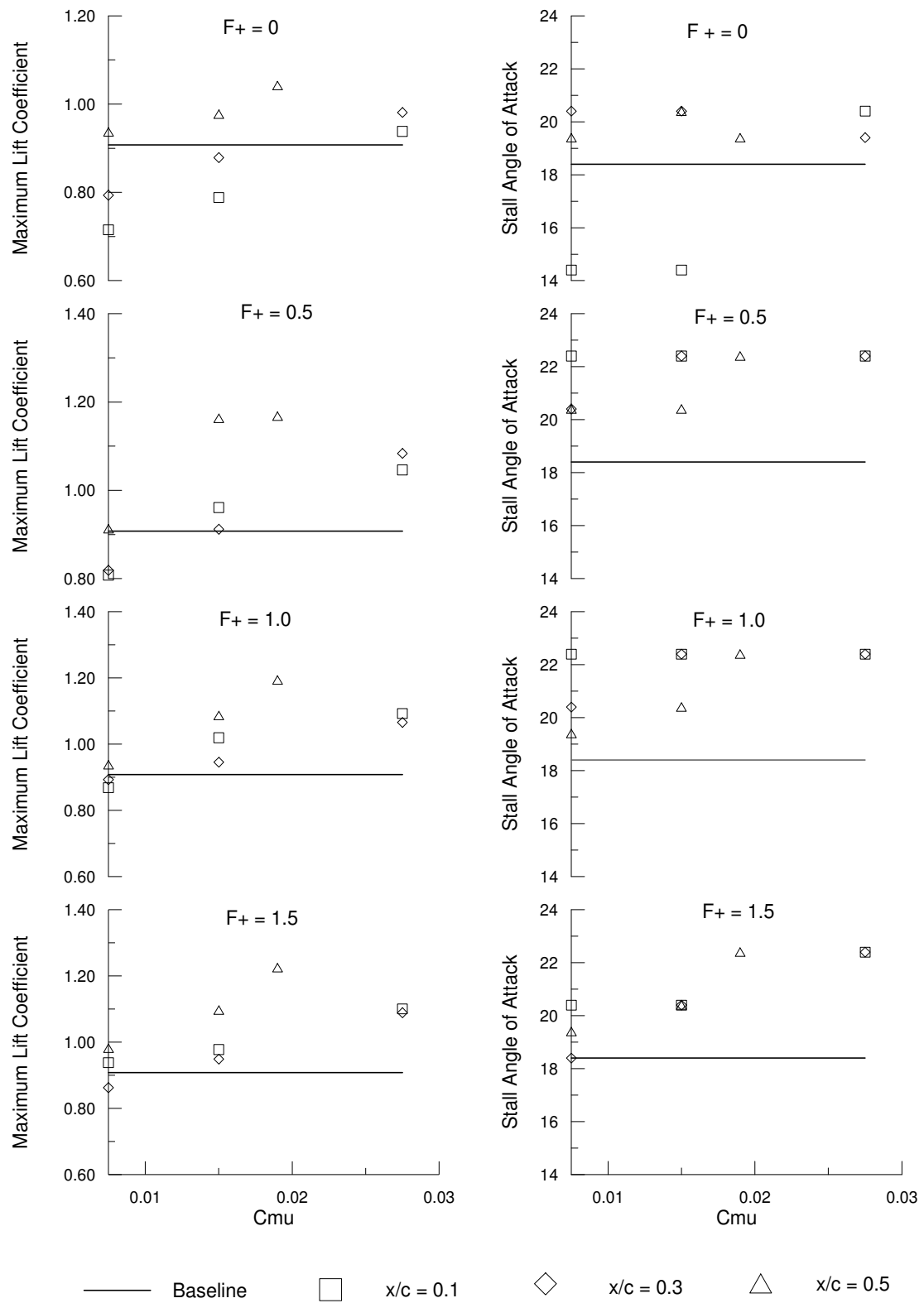


Figure 25. Variation of maximum lift coefficient with C_{μ} at different F^+

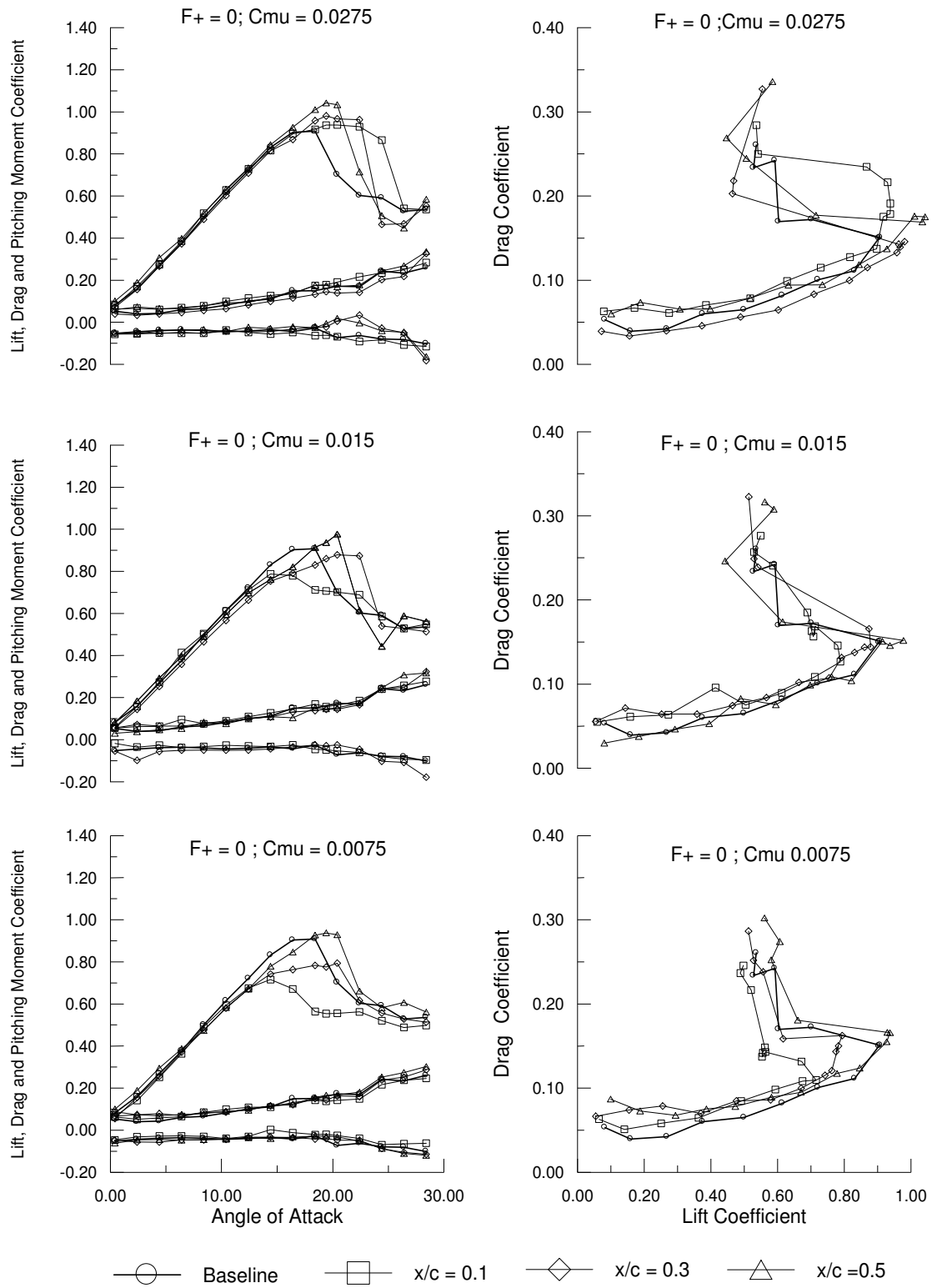


Figure 26. Performance curves of L.E. pulsed blowing at constant $F^+ = 0$

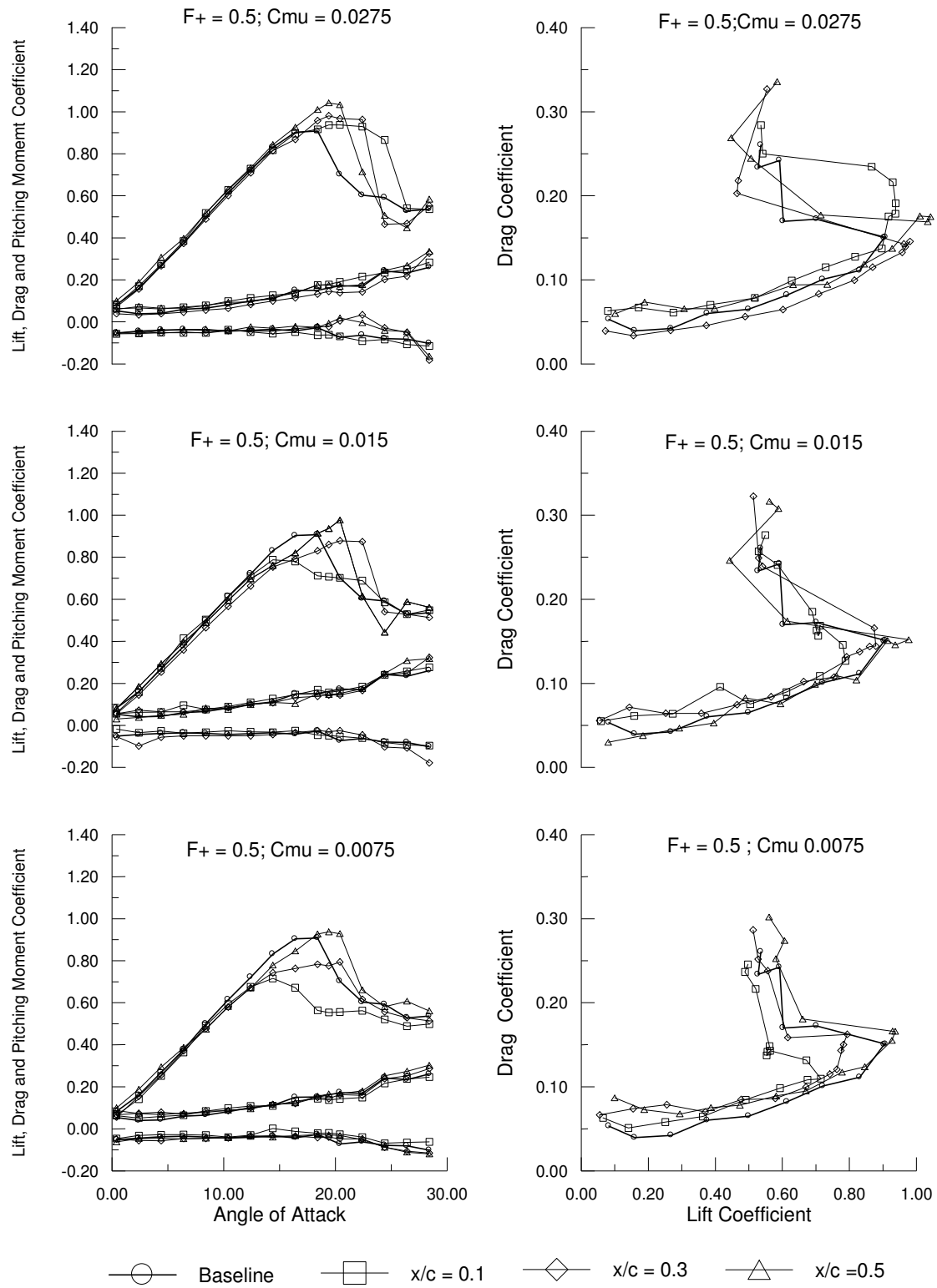


Figure 27. Performance curves of L.E. pulsed blowing at constant $F^+ = 1.5$

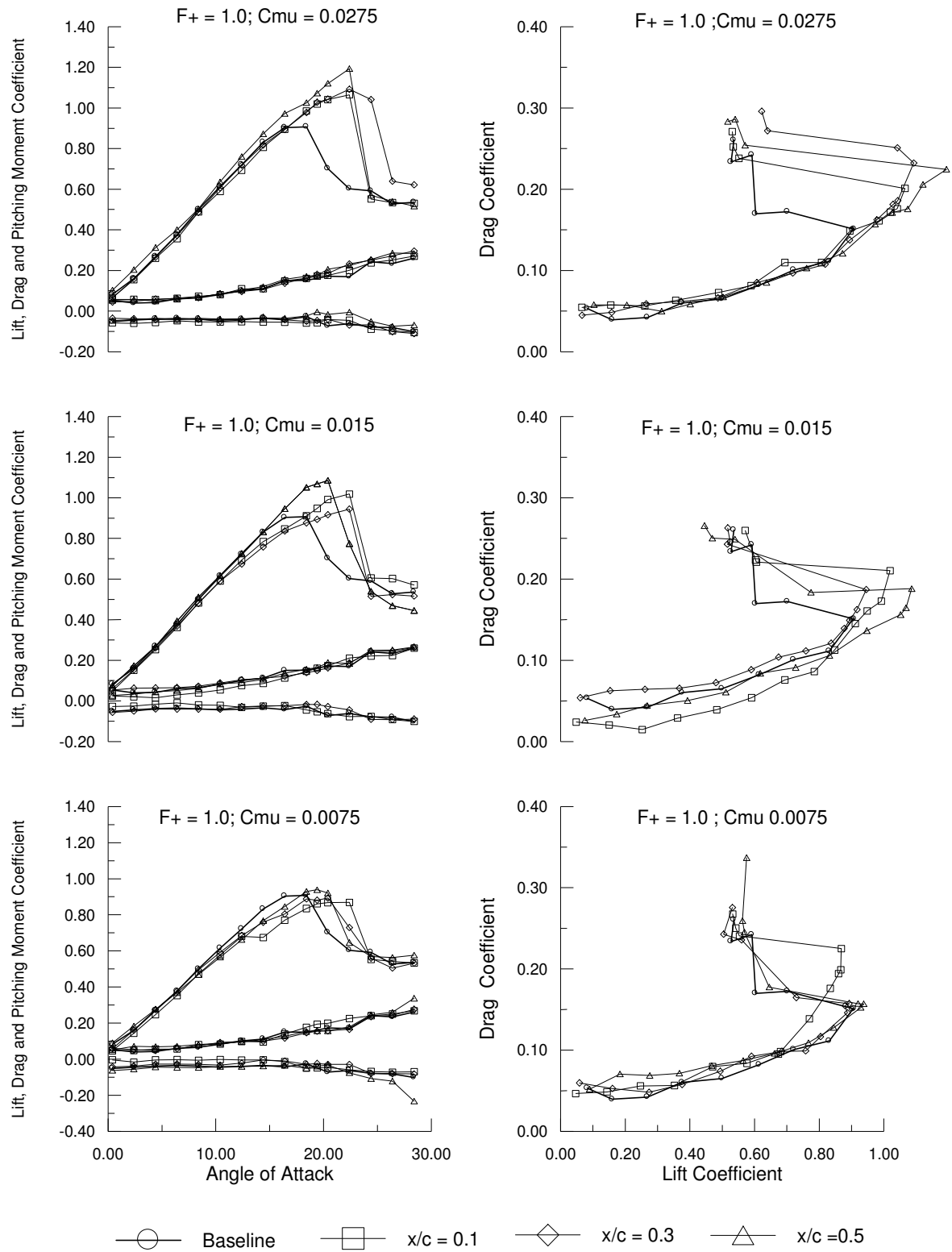


Figure 28. Performance curves of L.E. pulsed blowing at constant $F^+ = 1.0$

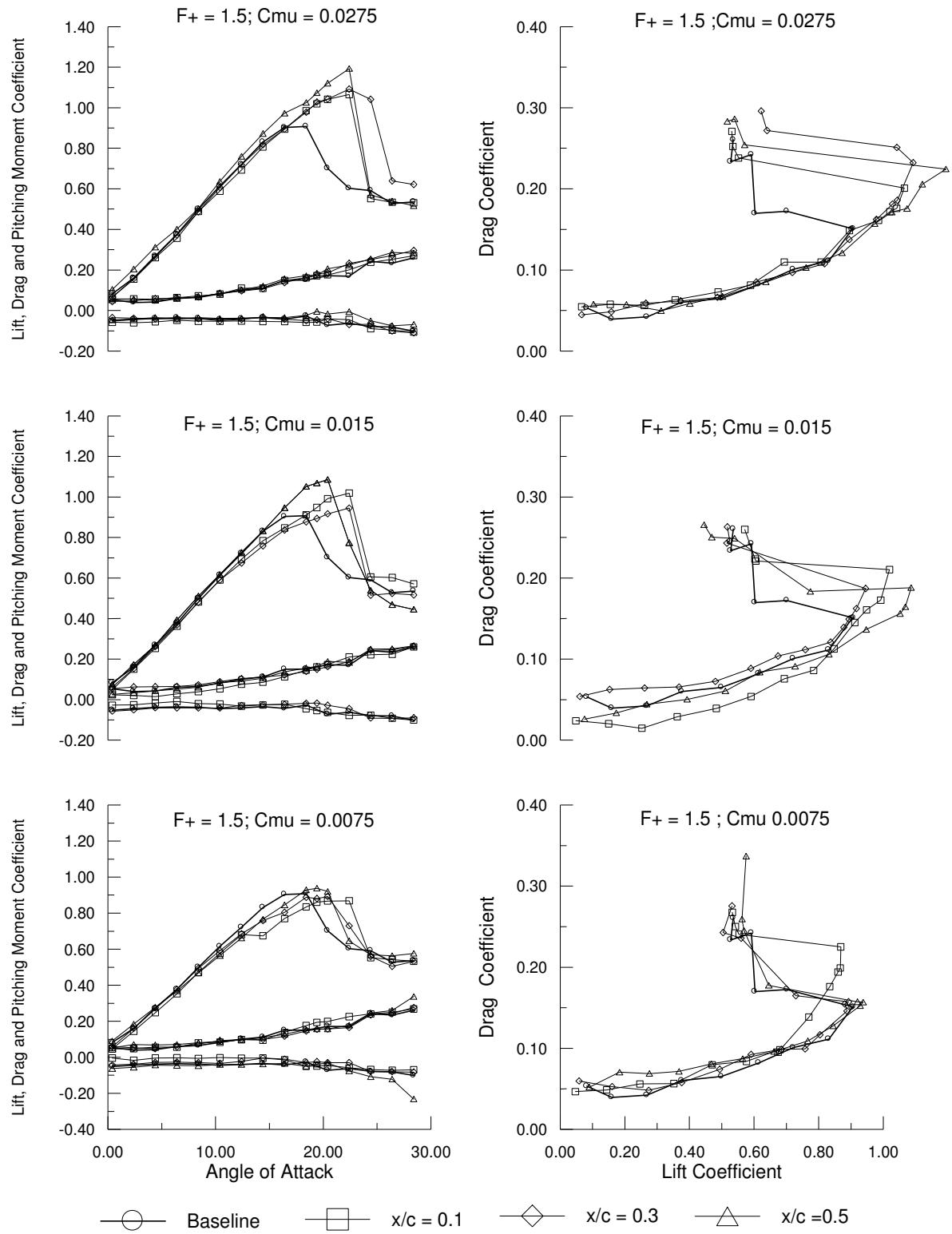


Figure 29. Performance curves of L.E. pulsed blowing at constant $F^+ = 1.5$

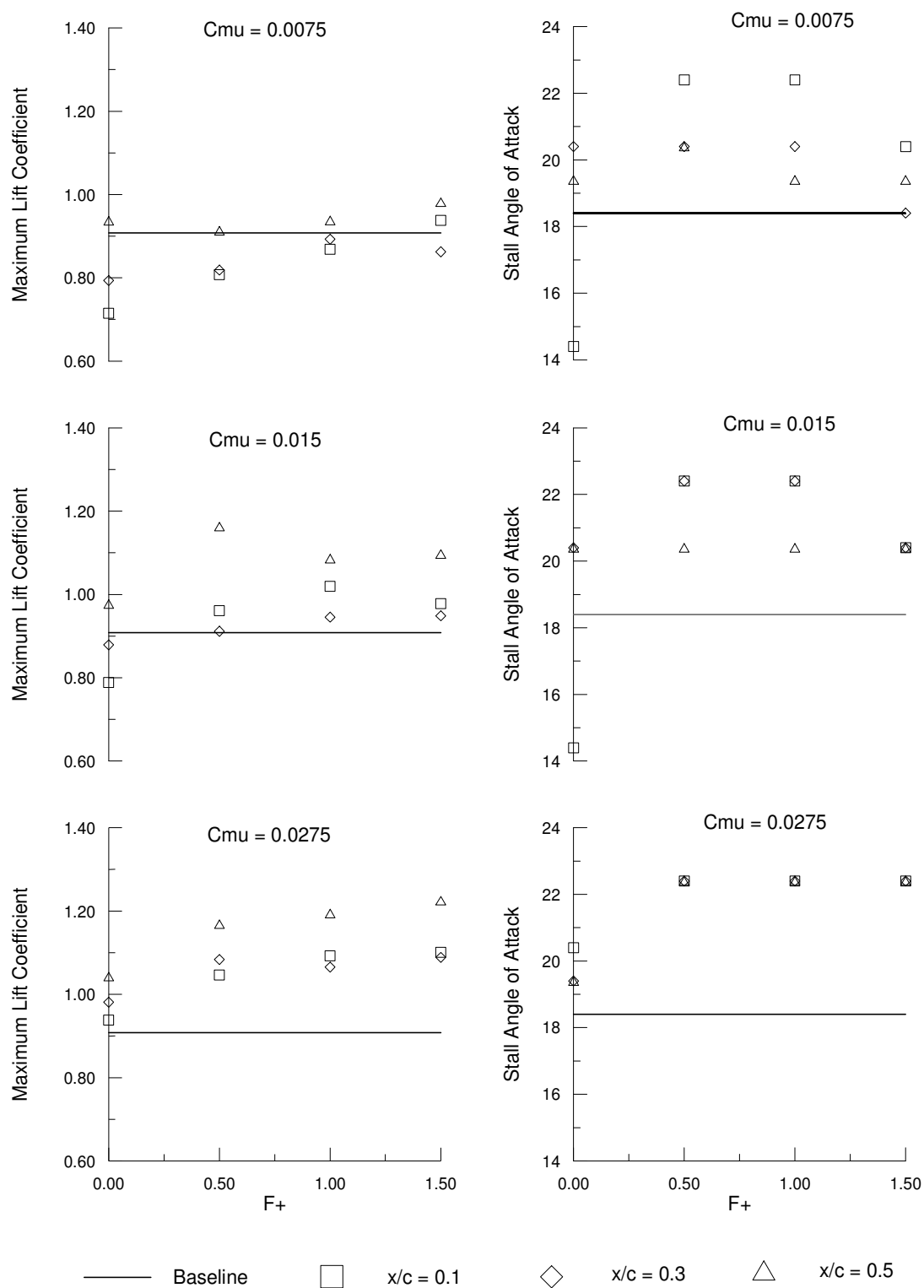


Figure 30. Variation of maximum lift coefficient with F^+ at different C_{μ}

Surface Pressure Measurements

Figures 31 to 33 show the results from the surface pressure measurements made on the wing at a free stream velocity of 20 m/s, both in the attached (angle of attack: 10.4°) as well as in the separated regime (angle of attack: 20.4°). The pressure at each port was sampled and averaged for over 200 times.

The surface pressure distribution on the basic wing in the separated region shows a flat pressure distribution. The flat pressure distribution is an indicator of a massively separated flow on the upper surface of the wing, which extends from 20% of the chord location to the trailing edge of the wing.

The pulsed air blowing has a global effect on the pressure distribution of the entire wing and is evident from the pressure distribution from all the actuated cases. The actuation of the leading edge pulser in the attached flow regime has resulted in a drop of the suction side pressure. However, the gains made by the actuation of the pulsed blower are offset by a corresponding decrease in pressure on the lower surface of the wing causing no observable lift increment.

At 20.4° angle of attack, jet momentum coefficient of 0.0275, the actuation of the pulsed blower causes a large pressure drop on the suction side. The pressure distribution on the lower surface of the wing is also lowered by the pulsed air actuation. However, there is effective pressure difference yielding into higher lift coefficients. The results also indicate that there are marginal gains made by the jet pulsation beyond F^+ of one.

The observation is of practical importance as the in-flight operation of the leading edge actuator can be optimized for a blower fans running at the maximum

continuous operating speed with pulser operating to achieve a maximum jet momentum coefficient, C_{μ} at an effective F^{+} of one. This operation will conserve battery charge, thus extending the test flight durations.

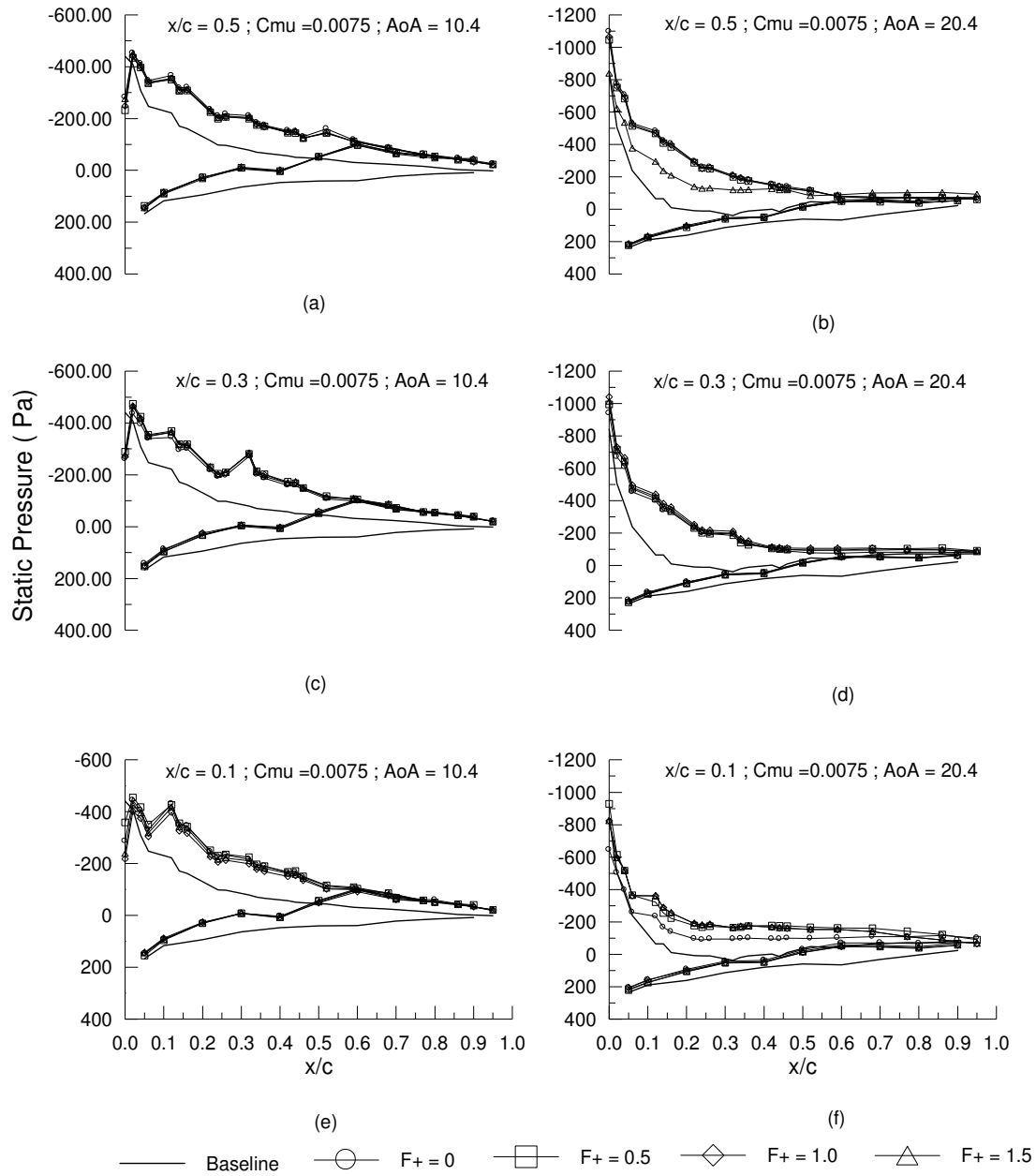


Figure 31. Effect of pulsed air blowing on the wing surface pressure distribution at $C_{\mu} = 0.0075$

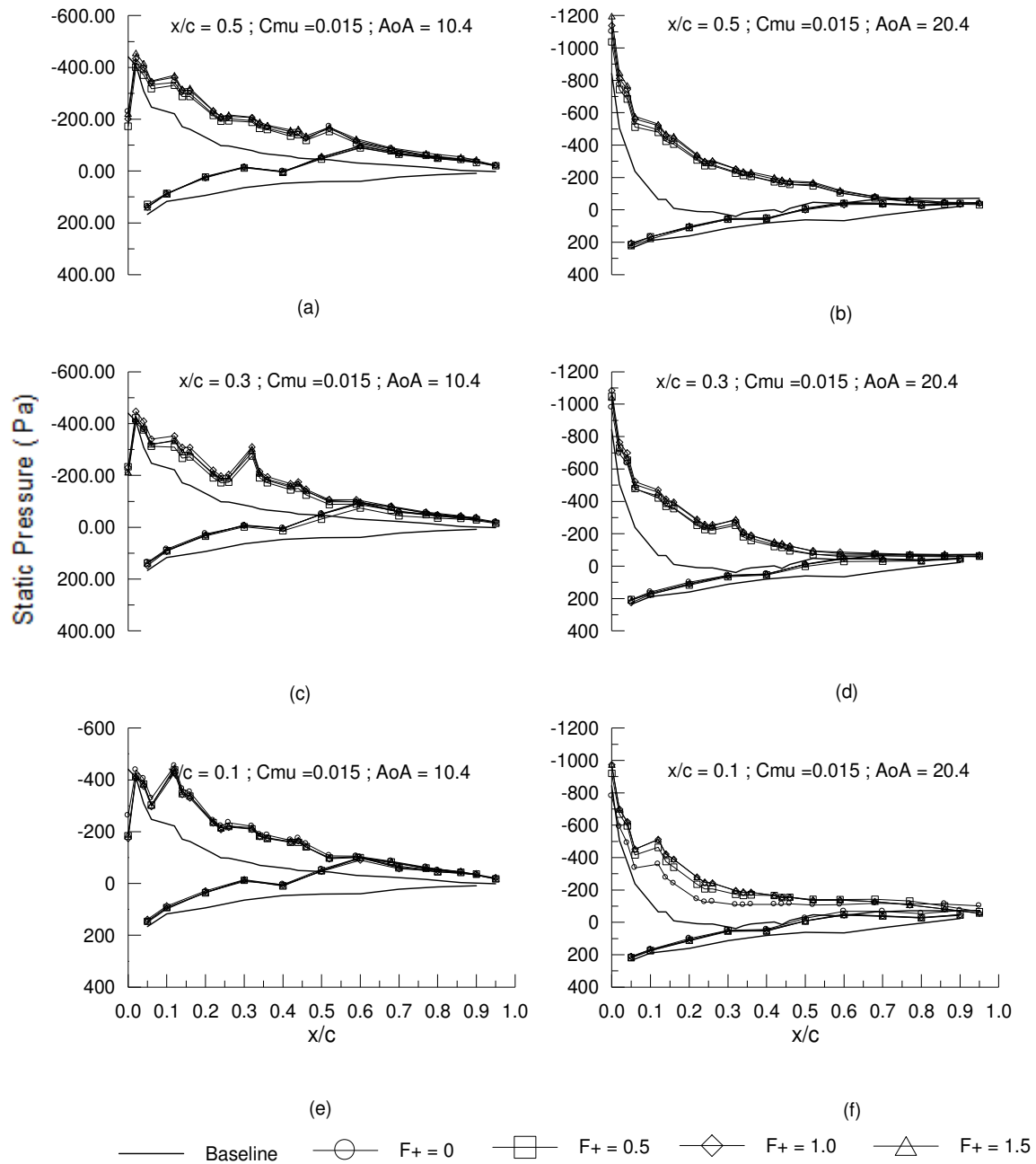


Figure 32. Effect of pulsed air blowing on the wing surface pressure distribution at $C_{\mu} = 0.015$

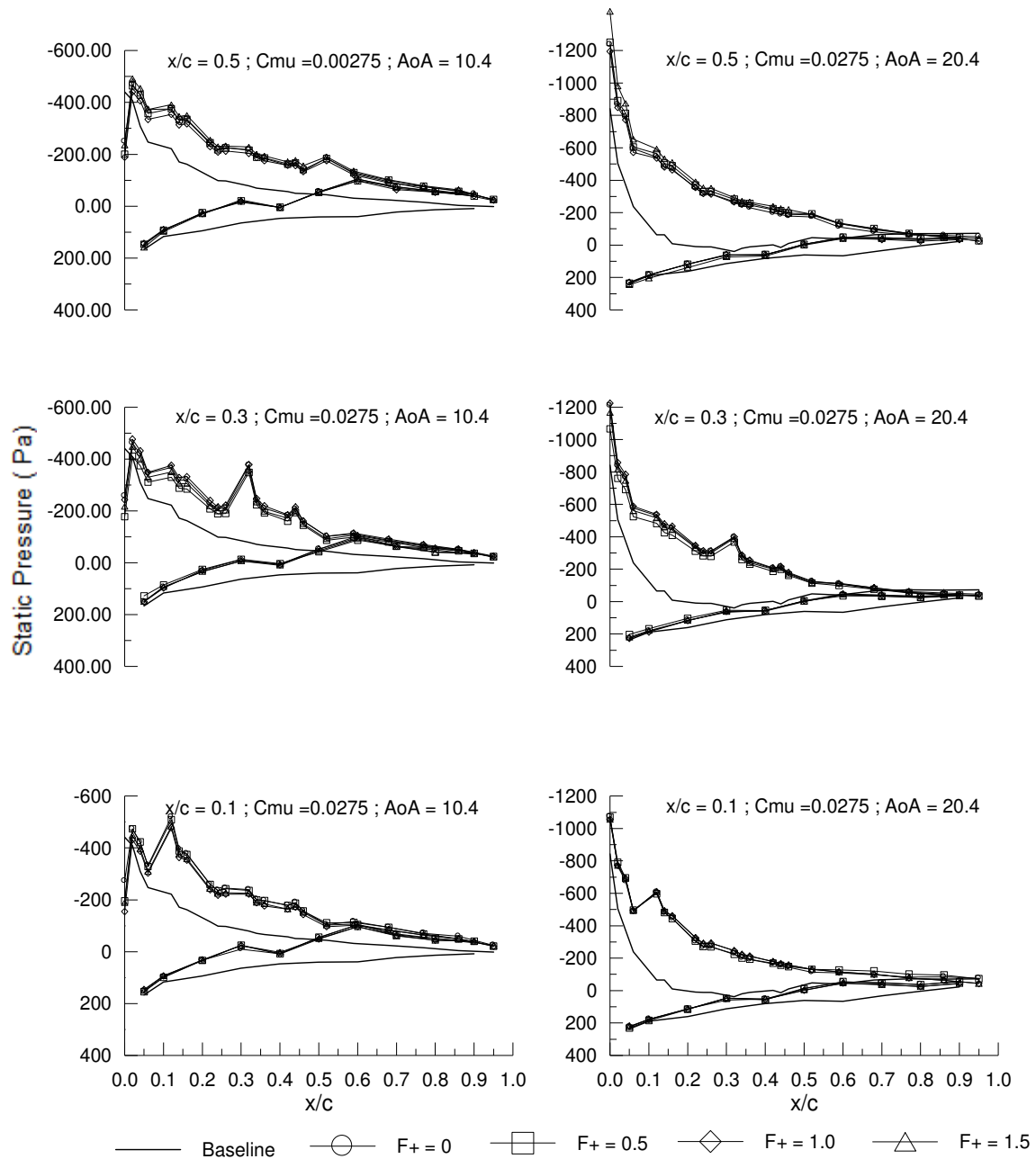


Figure 33. Effect of pulsed air blowing on the wing surface pressure distribution at $C_{\mu} = 0.0275$

Flow Reattachment through Sudden Pulsed Blower Actuation

As shown earlier, the leading edge pulsed blower has no effect on the performance characteristics in the pre-stall angle of attack regime. In order to optimize the flight operating conditions, the continuous operation of the leading edge pulsed air actuator over the entire angle of attack regime is not desirable.

Earlier results show that the pulsed blowing at maximum C_μ and F^+ of one has delayed the stall at both 10% and 50% chord location of the pulser. However, in all the tests performed, the pulser was operating during the entire angle of attack regime.

Ramp-up performance tests of the jet actuator were done to investigate the performance of the leading edge pulsed blowing, when started in the post-stall angle of attack regime. The tests were conducted at $F^+ = 0.5$ for a duration of 2.5 seconds. The data were recorded at 100 samples per second per channel. A lower $F^+ (= 0.5)$ was selected to record the data because of limited scan rate of the ESP. Figures 34 to 36 show the results of the lift coefficient integrated from the corrected pressure measurements at all the pulser locations. Results (Figures 34 and 35) indicate that the jet actuation at 10% and 30% chord location is capable of reattaching the flow instantaneously at the given test conditions. The 50% chord location, however, is not able to re-attach the instantaneously and resulted in lower lift coefficient.

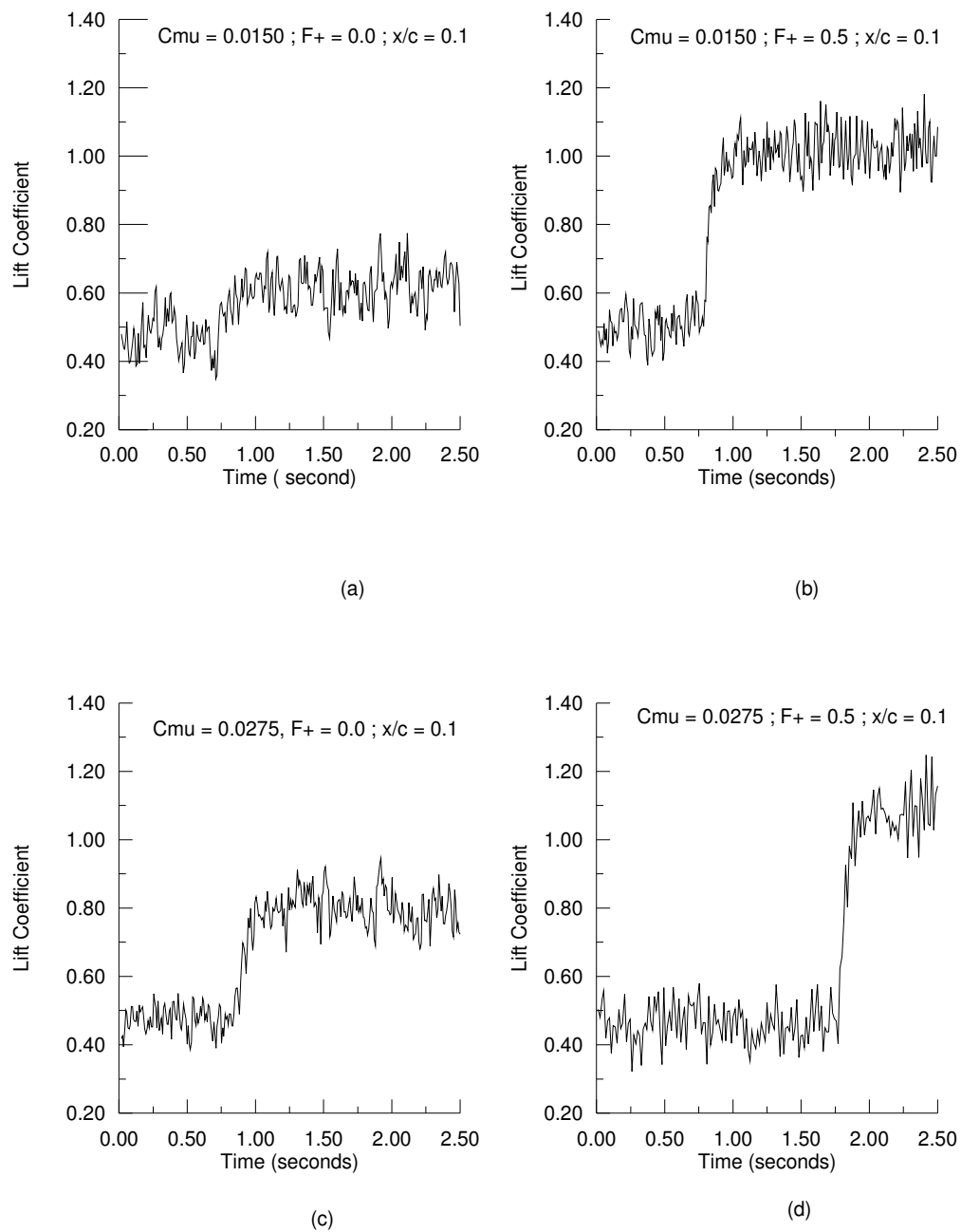


Figure 34. Response of leading edge pulser at $x/c = 0.1$ on sudden actuation

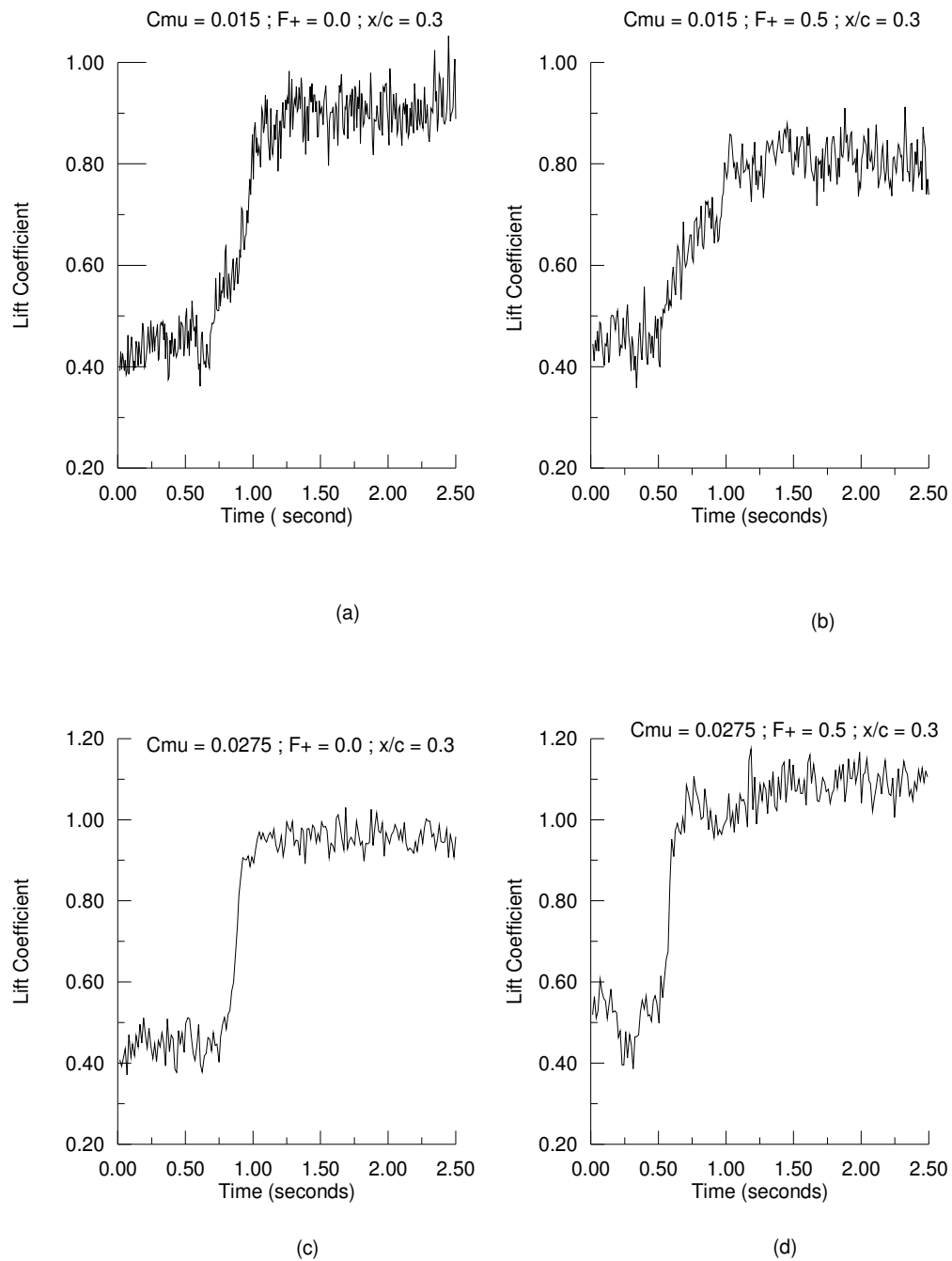


Figure 35. Response of leading edge pulser at $x/c = 0.3$ on sudden actuation

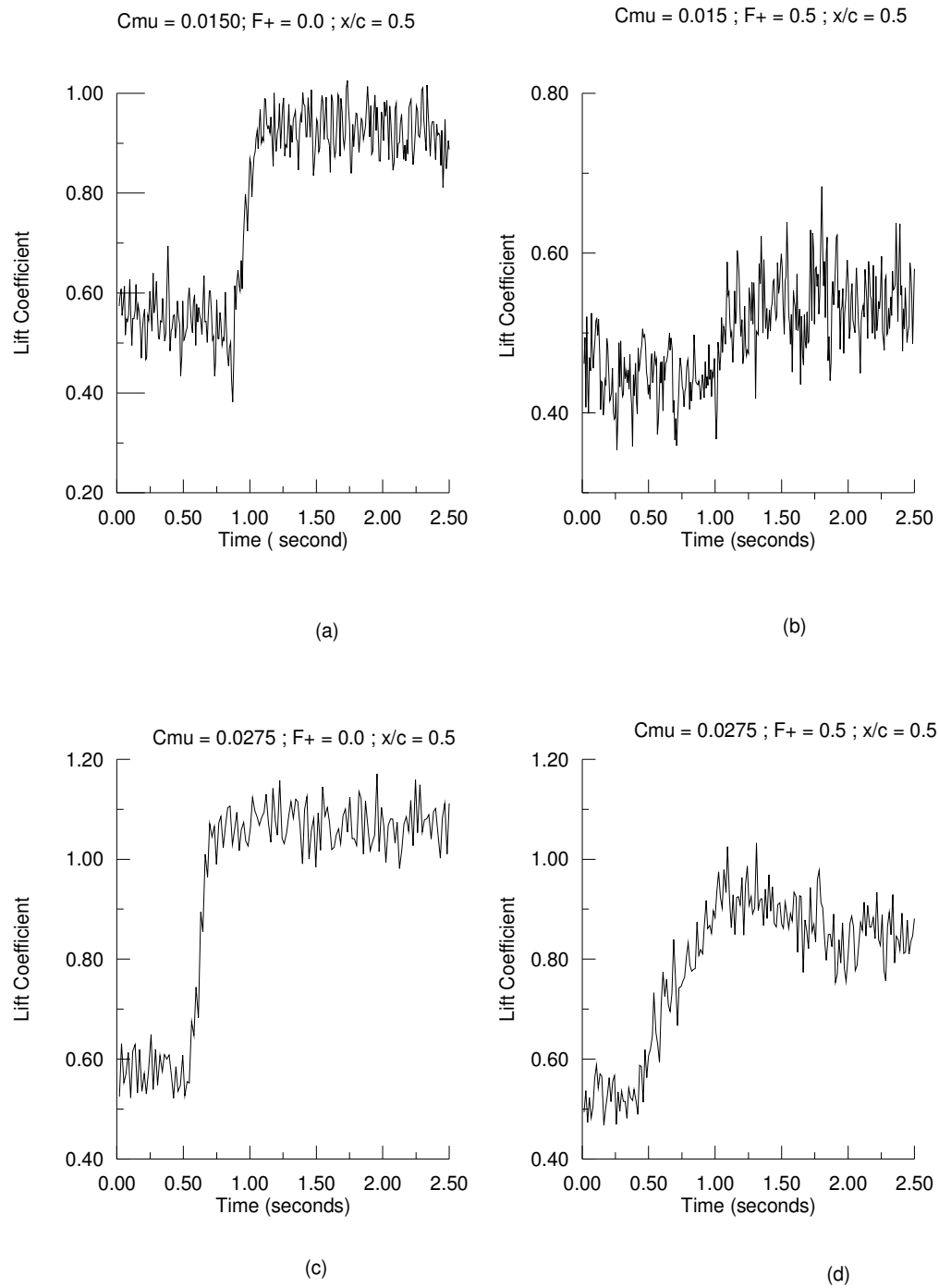


Figure 36. Response of leading edge pulser at $x/c = 0.5$ on sudden actuation

Flow Visualization

Figure 37 shows the result of the tufts placed on the surface of the wing at an angle of attack of 20.4° . The random motion of the tufts clearly shows the separated flow as discussed earlier in the thesis. The Figures 38 to 40 show the flow visualization at various operating conditions. For these tests, the angle of attack was set at 20.4° and the free stream velocity was 20 m/s. The effects of the pulsed blowing are noticeable with the flow being attached to the surface of the wing. In Figure 41, a few flow visualization results using a mixture of oleic acid, linseed oil, kerosene and titanium dioxide are presented.

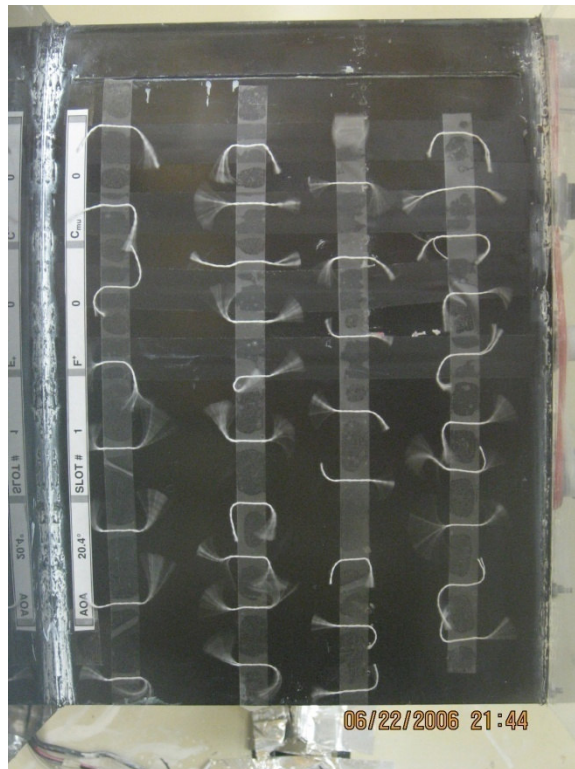
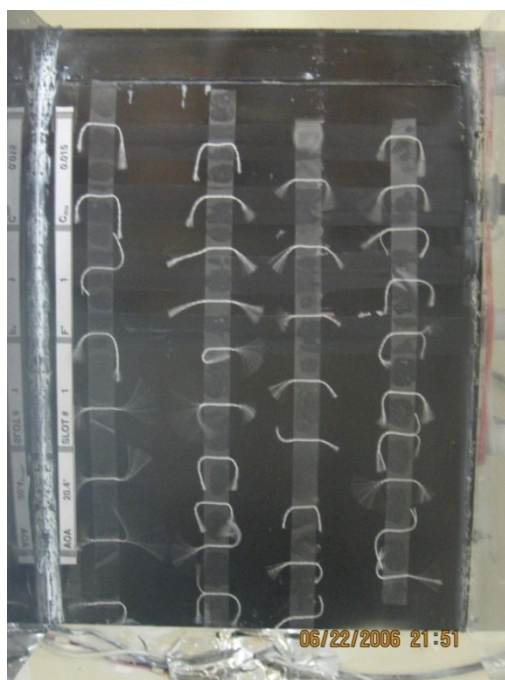
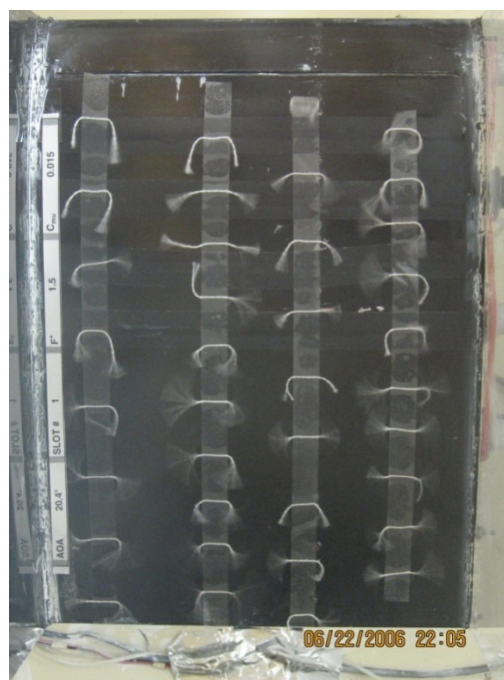


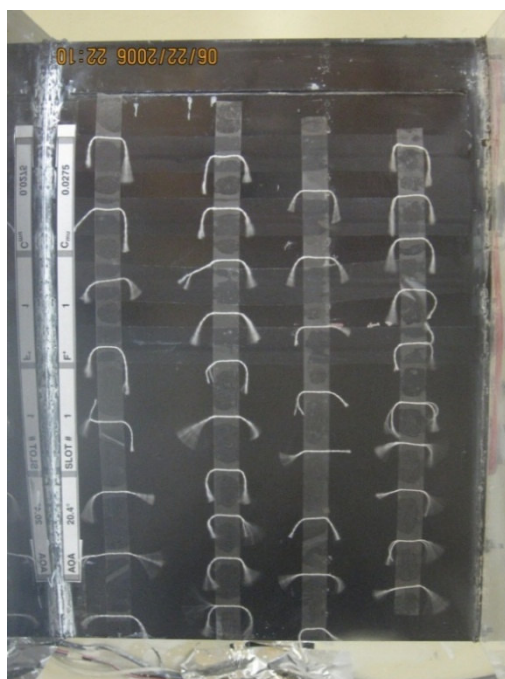
Figure 37. Flow visualization using tufts at 20.4° angle of attack with no actuation



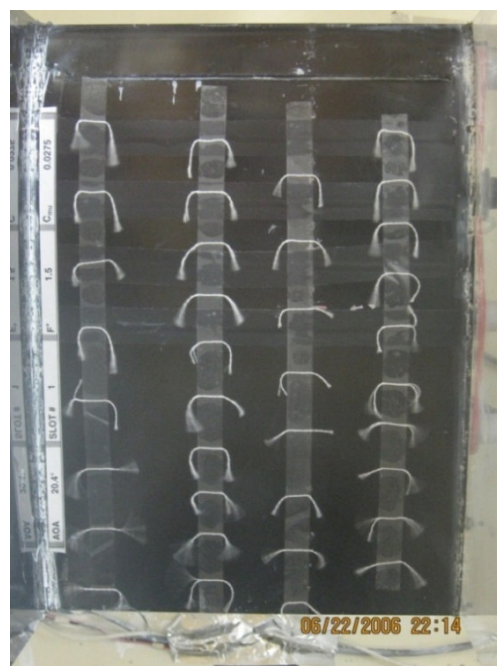
a) $AOA = 20.4^\circ$; $F^+ = 1$; $C_\mu = 0.015$



b) $AOA = 20.4^\circ$; $F^+ = 1.5$; $C_\mu = 0.015$



c) $AOA = 20.4^\circ$; $F^+ = 1$; $C_\mu = 0.0275$



d) $AOA = 20.4^\circ$; $F^+ = 1.5$; $C_\mu = 0.0275$

Figure 38. Flow visualization using tufts at 20.4° angle of attack at $x/c = 0.1$



a) $AOA = 20.4^\circ; F^+ = 1.0; C_\mu = 0.015$



b) $AOA = 20.4^\circ; F^+ = 1.5; C_\mu = 0.015$



c) $AOA = 20.4^\circ; F^+ = 1.0; C_\mu = 0.0275$

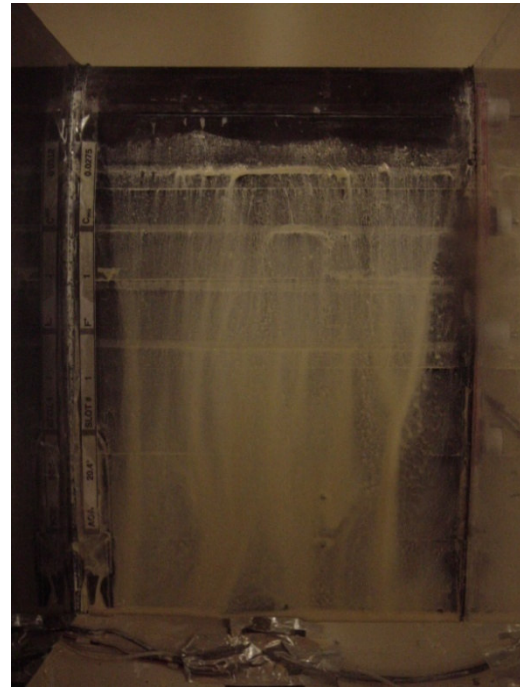


d) $AOA = 20.4^\circ; F^+ = 1.5; C_\mu = 0.0275$

Figure 39. Flow visualization using tufts at 20.4° angle of attack at $x/c = 0.3$



a) AOA = 20.4°; NO BLOWING



b) AOA = 20.4°; $F^+ = 1.0$; $C_\mu = 0.0275$; Slot # 1



c) AOA = 20.4°; $F^+ = 1.0$; $C_\mu = 0.0275$; Slot # 2



d) AOA = 20.4°; $F^+ = 1.0$; $C_\mu = 0.019$; Slot # 3

Figure 41. Flow visualization at various operating conditions

THE TEST VEHICLE

A $\frac{1}{3}$ scale Extra 330 model airplane has been selected to demonstrate the application of the active flow control technology. The fuselage of the airplane is all lightweight ply and balsawood construction with built-up balsawood constructed wings, elevator and rudder; fiberglass cowl and wheel covers. The main landing gear is made up of Aluminum and has metal wing tube. The model airplane comes as all most ready to fly kit and requires assembly of the various components and the servos as shown in Figure 42. The specifications of the airplane are given in Table 4.

Table 4. Specifications of $\frac{1}{3}$ scale Extra 330 model airplane.

| Model | Extra 330S |
|------------------------|---|
| Wing Profile | NACA 0015 |
| Vehicle Span | 2464 mm |
| Vehicle Weight | 12.5 kg |
| Vehicle Length | 2110 mm |
| Wing Loading | 10.3 kg/m ² |
| Engine Type | Air Cooled; 2 Stroke cycle type gasoline engine |
| Propeller Size (inch) | 24 × 10 |

The vehicle has been selected because of the following salient features:

- 1) It has a conventional planform similar to many existing unmanned aerial vehicles. The technology developed on this planform should not be limited to a specific configuration.
- 2) The aircraft has a wing with a thick profile. This gives sufficient volume for incorporation of the fluidic actuators.

- 3) The fuselage has large volume near the tail giving space to install a blowing system for replacement of the elevators.

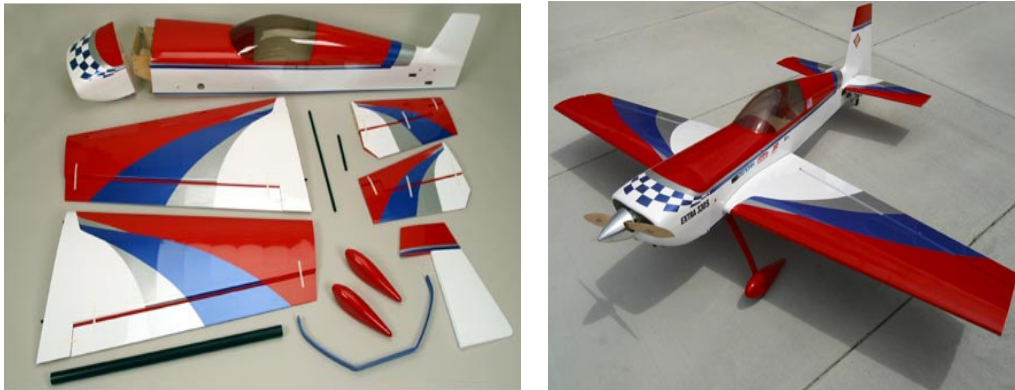


Figure 42. A 1/3 scale Extra 330 model airplane

A Zenoah G800BPU, two-stroke cycle, spark ignited gasoline engine, has been used in airplane. The fuel tank for the engine has been placed in fuselage and has a capacity of 32 fl oz, which allows for 10-minute test flight duration. The specifications of the engine are given in Table 5.

Table 5. Zenoah G800 BPU engine specifications

| Model | Zenoah G800BPU |
|-----------------------|--|
| Type | Air cooled two stroke cycle; opposed cylinder type gasoline engine |
| Displacement | 80 cm ³ |
| Compression Ratio | 8.3:1 |
| Maximum Output | 7.5 PS @10000 rpm |
| Operating Speed Range | 1800 – 10000 rpm |
| Weight | 3.6 Kg with mufflers and spring starter |
| Ignition System | CDI type flywheel magneto |

The vehicle's center of gravity with full fuel load and batteries has been established at the quarter chord location of the wings as shown in Figure 43. In order to

maintain the location of the center of gravity of the plane, ballast weight has been added in the engine compartment. The location of the center of gravity of vehicle will be maintained at the quarter-chord wing location for all the vehicle configurations.

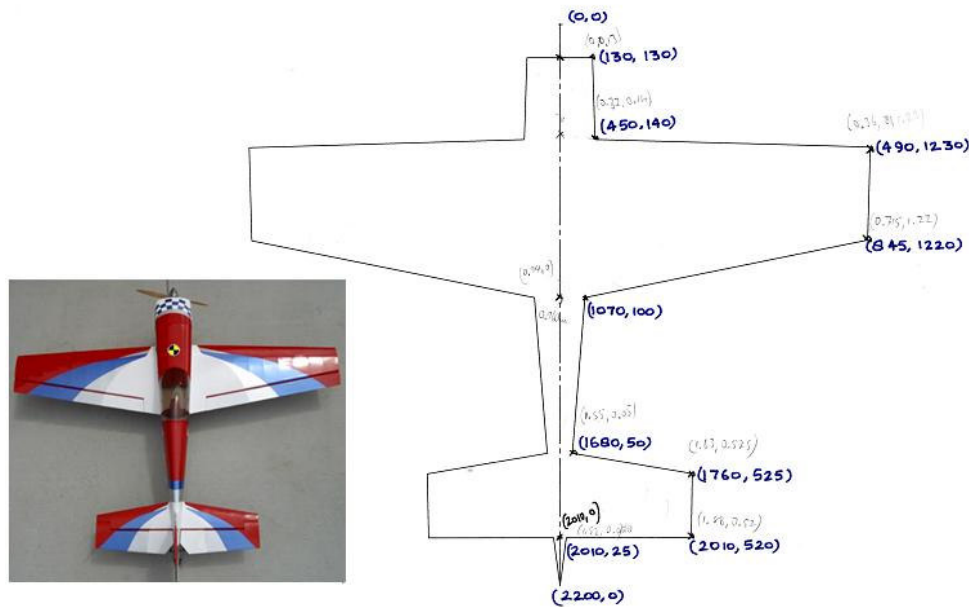


Figure 43. Top view of $\frac{1}{3}$ scale Extra 330 model airplane

The Extra 330 “Basic” Wing

The original wing of the $\frac{1}{3}$ scale extra 330-model airplane has a NACA 0015 profile and a span of 1090 mm (Figure 44). The wing’s skeleton is made up of balsawood and lightweight ply. The wing has eleven equally spaced ribs and two leading edge spars that are cross linked to each other using spider webs. The wing is secured to the fuselage using an Aluminum wing tube, a bolt and two guide pins. The left wing of the vehicle also has a pitot static probe to measure the free stream velocity. The wing skeleton has been covered by a Monokote[®] polyethylene film. The control surfaces of

the vehicle are controlled by digital servos. Table 6 shows the specification of the various servos that have being used in the vehicle.

Table 6. Specification of servos used in the basic configuration of the test vehicle

| Control Surface | Servo Type | Rated Torque | Quantity |
|-----------------|------------|--------------|------------|
| Throttle | Digital | 88 oz/in | 1 |
| Aileron | Digital | 155 oz/in | 2 per wing |
| Elevator | Digital | 155 oz/in | 1 per wing |
| Rudder | Digital | 155 oz/in | 2 |

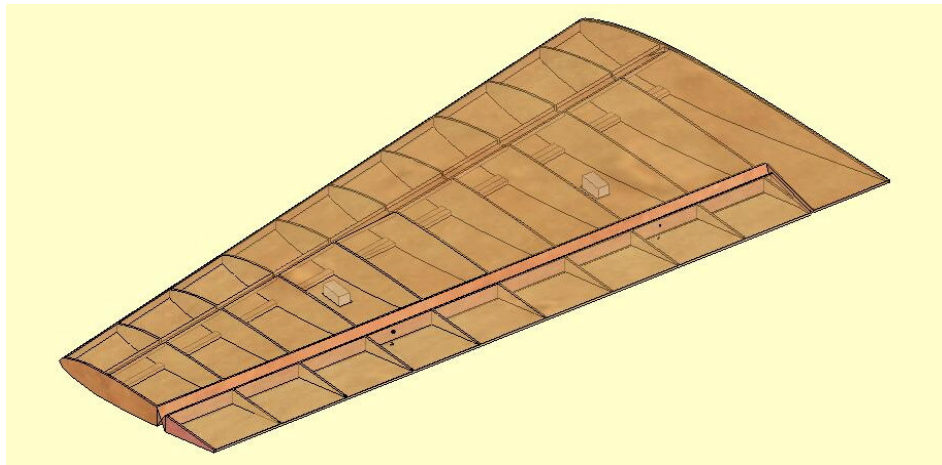


Figure 44. CAD model of the original wing

The Wing with Fluidic Actuators

The wing, with the fluidic actuators, has been designed to have the following three functions:

- 1) Trailing edge flow manipulation to alter the wing's circulation. This mimics the functioning of an aileron and generates localized lift manipulation resulting in aircraft roll.
- 2) Flow control to suppress upper surface flow separation.
- 3) Improved stealth through the removal of contour breaks in the wing.

Performance enhancement will be due to significant increase in the aircraft's flight range and ability to loiter. The leading edge flow control actuators will allow for a high angle of attack controllable flight. This will facilitate improvement in aircraft performance by realizing a short take-off and landing capability. The trailing edge actuators may reduce the weight of the vehicle when compared to the conventional control surface. The wing geometry and the major structural members including spar, wing tube and the root side of the wing have not been modified from the original geometry.

Leading Edge Actuators

The leading edge pulser has been placed at 15% chord location as shown in Figure 45. The decision to place the pulser at this location has been made on the basis of the wind tunnel test results discussed earlier in the thesis. The 10% chord location of the leading edge pulsed air blowing has a subtle angle of attack range over which it is effective and has the ability to re-attach the flow instantaneously when compared to 50% chord location. The 10% chord location of the pulsed air blowing, though, has slightly lower lift coefficients compared to aft location. The location of the wing spar is another major design parameter that has dictated the location of the pulsed blower mechanism.

The actuator mechanism consists of two centrifugal plastic impellers, driven by 12V DC brushless motors, that operate in tandem to pressurize the air (Figure 46). The air is being drawn from the leading edge on the pressure (lower) side of the wing. An Aluminum wire mesh has been used to cover the wing opening (Figure 47). The space between the Monokote[®] polyethylene film skin of the wing and the upper plate of the impeller housing acts as the settling chamber/plenum. The housing for the two impellers is a volute design that later merge to form a single delivery manifold.

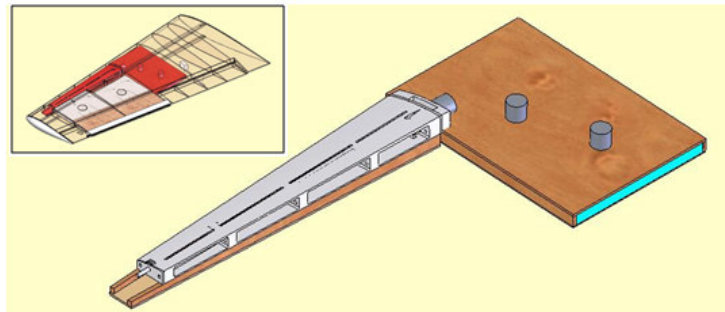


Figure 45. Leading edge actuator at 15 % chord length location

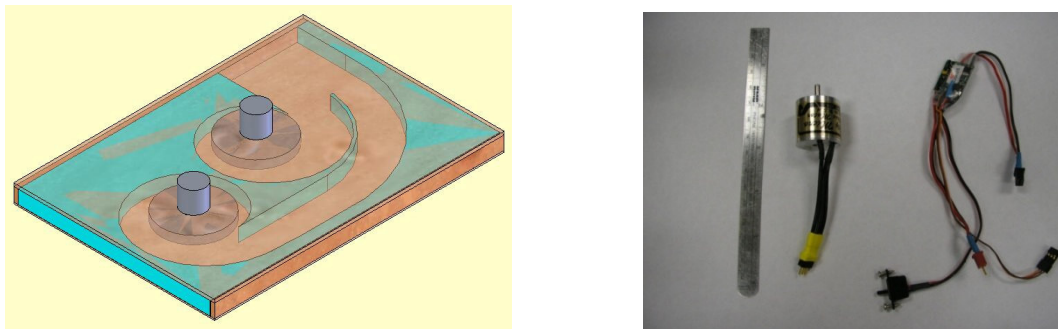


Figure 46. Two impeller fan housing and brushless motors

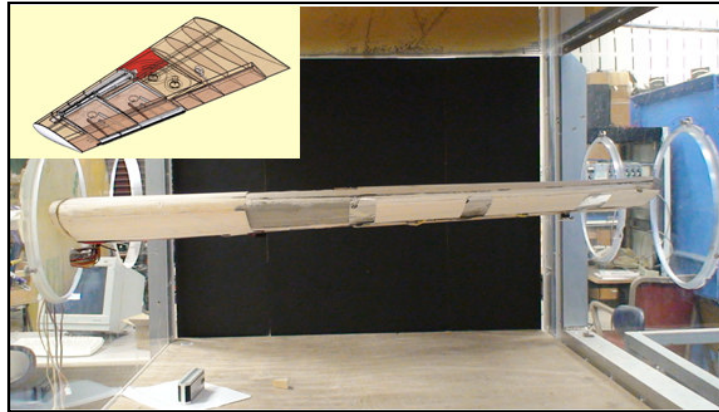


Figure 47. Intake manifold for the leading edge pulsed blowing

To avoid the slip between the motor shaft and the impeller hub at high rotational speeds, an Aluminum insert (Figure 48) has been used to connect the impeller to the motor shaft. The speed of each impeller is monitored using an optical sensor located underneath the impeller.



Figure 48. Impeller with aluminum insert

The delivery manifold, made up of bass wood and acrylonitrile butadiene styrene (ABS) plastic, spans 440 mm along the wingspan and ends at 100 mm from the wing tip. To achieve a span wise uniformity of the flow, the cross sectional area of the delivery manifold reduces in a ratio of 3:1 from the root side to the tip side of the wing. The flow

has span wise velocity uniformity within 90% of the set velocity. The upper surface of the delivery manifold has the same contour as that of the wing surface. The air exits tangentially to the surface from four 1.75 mm wide slots that span along the delivery manifold. (Figure 49).

The pulser shaft (Figure 50), machined from a 9 mm diameter Aluminum rod, is 440 mm long and has a 25 mm long, 4.8 mm in diameter pin on the each end. The shaft also has a 3.175 mm wide through slot with three support ribs. The ribs have been provided to prevent the shaft walls from bulging at high rotational speeds.

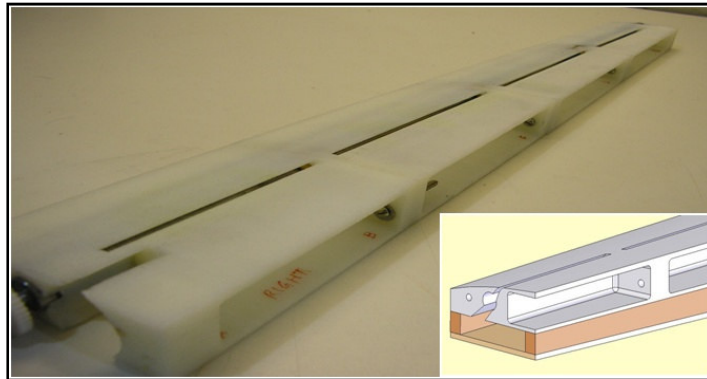


Figure 49. The pulser housing; inset: exit jet slot geometry and delivery manifold

To reduce the eccentricity in rotation of the pulser shaft, it is supported by a ball bearing at each end and three oil-impregnated bronze sleeve bushings (Figure 50). The pulser shaft is driven by a 12 V DC brushless motor by a gear train (Figure 50). The 1:2 gear reduction provides sufficient torque to overcome the starting torque of the pulser shaft. The speed of the pulser shaft is monitored using an optical sensor on the driven gear.

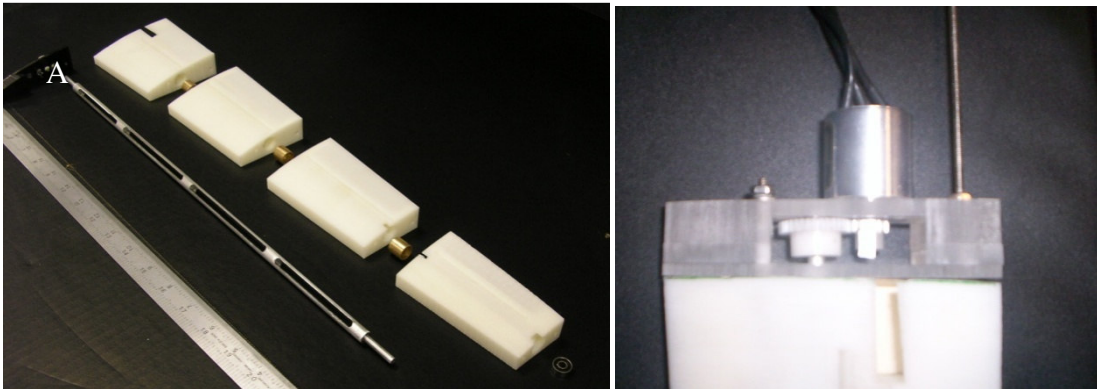


Figure 50. The pulser shaft and its driving mechanism

Trailing Edge Jet Blower

The trailing edge jet flap spans 440 mm, 100 mm from the wing tip as shown in Figure 51. The span wise location of the jet flap is same as that of the leading edge jet blower. Seven ribs (from the tip side) have been removed without damaging the spars to install the trailing and leading edge actuator housing.

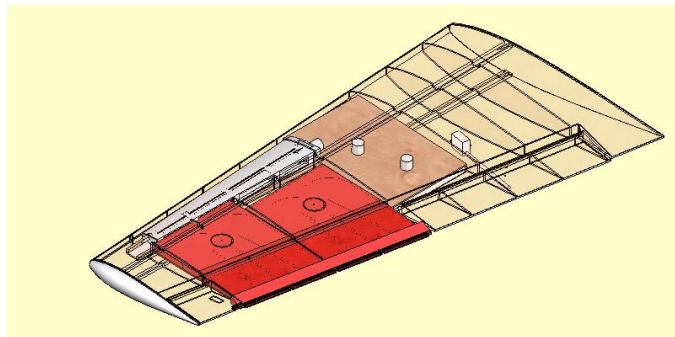


Figure 51. Location of trailing edge jet blower assembly

The removed ribs have been replaced with 3 mm thick lightweight plywood ribs, as shown in Figure 52. The new ribs have a higher load bearing capacity to support the

entire weight of the actuators. The ribs 2 through 5 (Figure 52) have a cut on the leading edge side to accommodate the delivery manifold of the leading edge pulsed air blowing mechanism. Ribs 4 and 5 have been cut to less than half of their full length as they interfere with the trailing edge motor mount. The length of the aileron has also been reduced to in-board 400 mm from the current 980 mm and is attached to the main wing by two hinge points as shown in Figure 53.

The air for the trailing edge jet blowing is drawn from the wing tips. To facilitate the induction of the air, the wing tip has been modified as shown in Figure 53. The two intermediate support panels on the wing tip rib provide support to the end of wing spars. An end cap, made from aluminum wire mesh, has been provided to cover the opening in the wing tip rib to prevent any debris entering into the impeller hosing as shown in Figure 54.

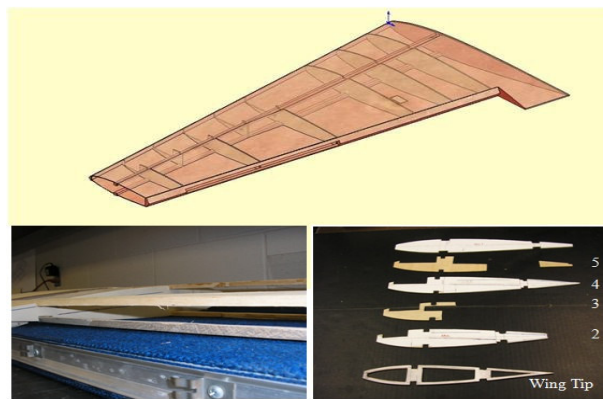


Figure 52. Modified wing structure and the ribs

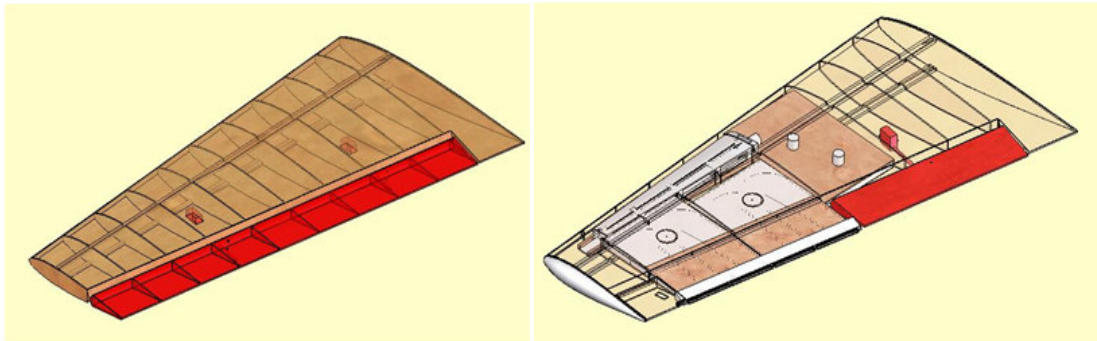


Figure 53. Full and reduced aileron

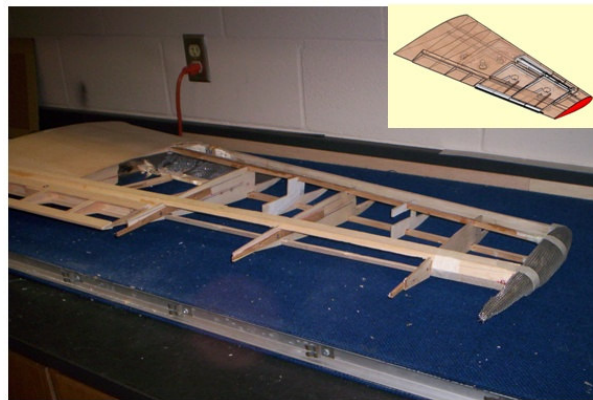


Figure 54. Trailing edge wire mesh intake manifold and modified wing structure

The trailing edge jet blower assembly (Figure 55) is made up of two independent units for pressurizing the air. The two-part modular design reduces the structural modifications to be made in the original wing and has a better serviceability.

The base plate is made up of 3 mm thick lightweight plywood and acts as the mounting plate for the fan motor. An optical sensor is also mounted on the lower surface to monitor the speed of the impeller. The upper plate is made up of 1.5 mm thick lightweight plywood and is divided into two halves for ease in serviceability in case of impeller/sensor failure. Five walls supporting the upper and the lower surface of the housing taper in height from 12.5 mm to 5 mm on the trailing edge side to increase the

flow velocity. The walls also straighten the flow such that there is minimal span wise velocity component of the exit jet. The flow has 90% flow uniformity for each jet blower unit.

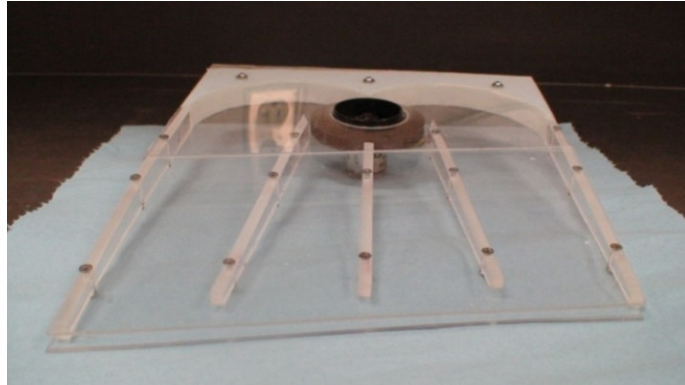


Figure 55. Trailing edge jet blower assembly in Plexiglass®

The mouthpiece for the trailing edge jet has been machined from lightweight, structurally stable wood. It has a 4.8 mm wide through slot for the flow of air. The jet flap has been machined from a 2.5 mm thick, 10 mm wide steel plate. It has been mounted to the mouthpiece at three locations along the span using Aluminum bushings.

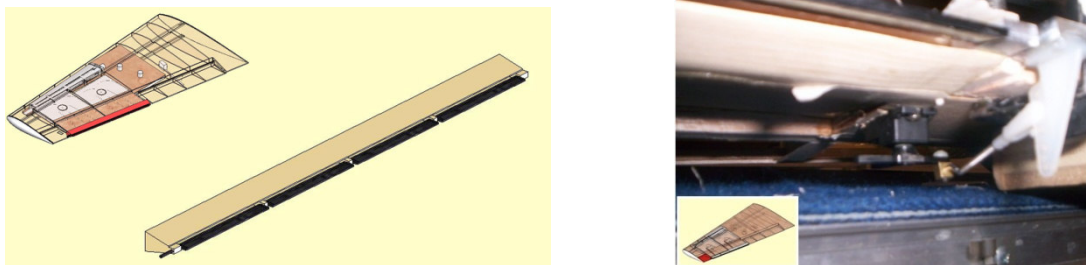


Figure 56. Trailing edge jet flap and servo mechanism for jet flap deflection control

The final gap between the walls of the mouthpiece and the jet flap is 2.75 mm at its maximum deflected position of $\pm 45^\circ$ and acts as 1% Gurney flap. A digital servo, located on the tip side of the wing (Figure 56), controls the deflection of the flap as shown in Figure 57. Because of the limited availability of input/output channels in the flight controller, there is no feedback control to monitor the position of the flap. The rated torque and type of servo used for different control surfaces is given in Table 7.



Figure 57. Flow visualization of the trailing edge jet at different deflection angles

Table 7. Specification of servos used in the test vehicle with fluidic actuators

| Control Surface | Servo Type | Rated Torque | Quantity |
|-----------------|------------|--------------|------------|
| Throttle | Digital | 88 oz/in | 1 |
| Aileron | Digital | 155 oz/in | 1 per wing |
| Elevator | Digital | 155 oz/in | 1 per wing |
| Rudder | Digital | 155 oz/in | 2 |
| Jet Flap | Digital | 23 oz/in | 1 per wing |

Optical Tachometers

To measure the speed of the various rotating components, an optical sensor, OPB608A, from Optek Technology Inc. has been used. The sensor is a reflective switch

that consists of an infrared light emitting device and an NPN silicon phototransistor mounted side-by-side on a parallel axis in a black opaque plastic housing.

The sensor can measure a frequencies up to 300 Hz within a distance of 0.050 inch to 0.375 inch between sensor and reflective surface. A common collector circuit has been used to read out the analog voltage from the sensors. The voltage out is read into a National Instruments[®] data acquisition system and Labview[®] based program. Figure 58 shows the physical dimensions and the control circuit for the optical sensor.

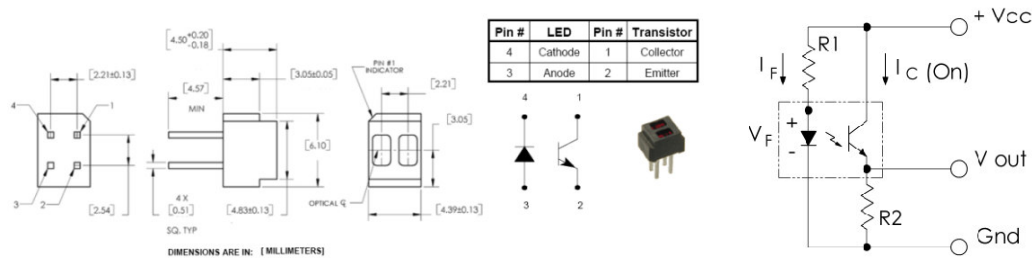


Figure 58. Optical sensor and its control circuit

In-flight Pressure Measurement

In order to facilitate the use of on-board air data system, a standard five-hole pressure probe from Aeroprobe Inc. has been installed on the outboard side of the left wing (Figure 59). The jet momentum coefficient from the leading and trailing edge actuators was measured using a miniature pitot tube, installed upstream of the jet exit. The pressure ports are connected to the miniature pressure transducers, capable of measuring ± 2.4 kPa, using micro bore Tygon[®] tubing. The jet velocity is obtained by using a calibration curve between the set velocity and the voltage sensed by the transducer.

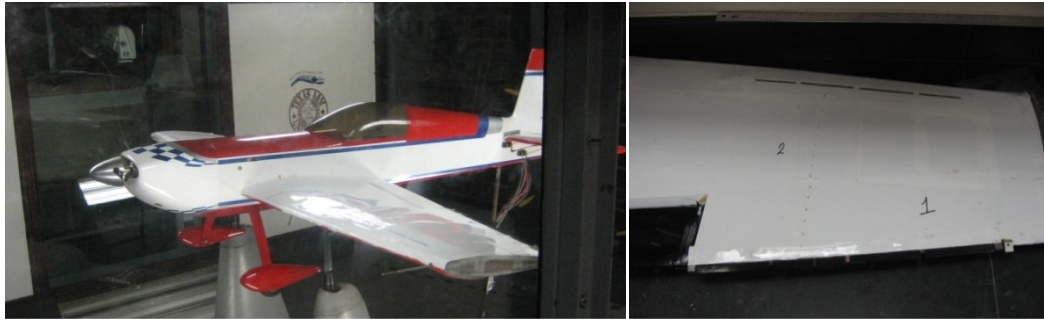


Figure 59. 5-Hole probe and pressure ports on the upper surface of the wing

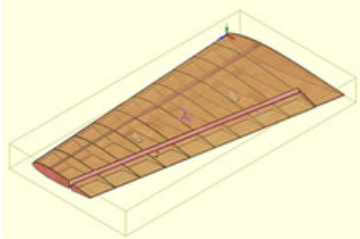
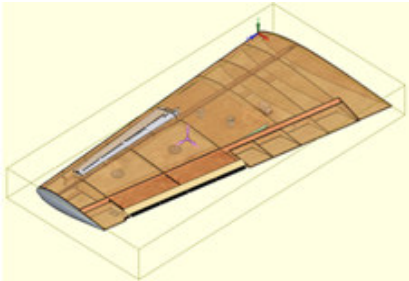
Final Assembly

During the final assembly of the wing, a consideration has been given to the serviceability of the individual components. The impeller housings have been attached to the wing ribs using screws and adhesive transfer tapes. A two-part epoxy has been used to bond the wing ribs, trailing edge mouthpiece, and wire mesh intake manifold to the wing structure. To reduce the transfer of vibrations from the pulser assembly to wing, a rubber pad is placed between pulser assembly and wing ribs. The wing is covered by a Monokote[®] polyethylene film. The wiring harness for the various electrical components in the wing has been assembled from the following wires

- 1) A three conductor 18 AWG (American Wire Gauge) wire is used to power the motors.
- 2) A four conductor 28 AWG wire is used to connect the sensors to the circuit boards.
- 3) A three conductor 26 AWG wire is used to connect the solenoids to the circuit boards.

Standard RC interconnects are used in the wiring harness. A custom designed avionics package is being developed by Aeroprobe Inc. for the future test flights. Table 8 compares the mass and center of gravity of both conventional and wing with fluidic actuator.

Table 8. Comparison of the conventional wing and the wing with fluidic actuators

| Property | | Original wing | Wing with Fluidic Actuators |
|---|---|---|---|
| Configuration | |  |  |
| Mass | | 1000 gm | 2500 gm |
| Center of Gravity (from leading edge tip on root side) | x | 254 mm | 233mm |
| | y | -6.0 mm | 1 mm |
| | z | 474 mm | 561 mm |

WIND TUNNEL TESTING OF THE VEHICLE

Facility Description

The wind tunnel tests were conducted at 8 ft by 10 ft Oran W. Nicks low speed wind tunnel facility at Texas A&M University. For the acquisition of force and moment data, the model was mounted, using a three-strut support, on an external balance located immediately below the test section as shown in Figure 60. The two main struts of the system were spaced 34 inches laterally and were pivoted to the wing. A pitch strut was used to rotate the model about the trunnion to change the angle of attack. The trunnion point was set at 42 inches above the test section floor and corresponded to the moment resolving center of the external balance. Fairings were used to allow for tare and interference measurements. The tunnel flow was controlled and measured in terms of dynamic pressure. The wind tunnel flow characteristics are shown in Table 9.



Figure 60. Mountings for the airplane in the low speed wind tunnel

The external balance, located directly beneath the test section, is a six-component, pyramidal, virtual center, electro-mechanical balance, which resolves all aerodynamic forces acting upon the test model in to three orthogonal forces and their

Table 9. Flow characteristics of the O. W. Nicks Low Speed Wind Tunnel

| Parameter | | Specification |
|-----------------------------|-------|---------------------------|
| Maximum Tunnel Velocity | | 300 ft/s |
| Dynamic Pressure Variation | | $\pm 0.4\%$ |
| Dynamic Pressure Resolution | | $\pm 0.5 \text{ lb/ft}^2$ |
| Flow Angularity | | $\pm 0.25^\circ$ |
| Static Pressure Gradient | | 0 |
| Turbulence Factor | | 1.1 |
| Turbulence Intensity | | Under 1% |
| Boundary Layer Thickness | Entry | 1.5 inches |
| | Exit | 3.5 inches |

associated moments. These components are measured about the wind oriented axes coordinate system having its origin at the balance-resolving center. The balance center corresponds to the geometric center of the test section (42 inches from the floor, 60 inches from the sidewalls and at the center of the turntable). Balance components are linear and repeatable within 0.10%. The range, accuracy and resolution of the force and moment measurement capability are given in Table 10.

Table 10. O.W. Nicks Low Speed Wind Tunnel external balance specification

| Component | Range | Accuracy | Resolution |
|-----------------|---------------------------|--|------------------|
| Pitch | -35° to 35° | $\pm 0.05^\circ$ | $\pm 0.01^\circ$ |
| Yaw | -120° to 190° | $\pm 0.05^\circ$ | $\pm 0.01^\circ$ |
| Lift Force | -1000 lbs to 3000 lbs | $\pm 0.10 \text{ lb}$ or 0.1% of the applied load | 0.01 lb |
| Drag Force | -1000 lbs to 1000 lbs | $\pm 0.10 \text{ lb}$ or 0.1% of the applied load | 0.01 lb |
| Side Force | -1000 lbs to 1000 lbs | $\pm 0.10 \text{ lb}$ or 0.1% of the applied load | 0.01 lb |
| Pitching Moment | -2000 lb-ft to 2000 lb-ft | $\pm 0.10 \text{ lb-ft}$ or 0.1% of the applied load | 0.01 lb-ft |
| Yawing Moment | -1000 lb-ft to 1000 lb-ft | $\pm 0.10 \text{ lb-ft}$ or 0.1% of the applied load | 0.01 lb-ft |
| Rolling Moment | -2000 lb-ft to 2000 lb-ft | $\pm 0.10 \text{ lb-ft}$ or 0.1% of the applied load | 0.01 lb-ft |

A Labview[®] based program was used to control the fluidic actuators using National Instrument[®] 14-bit data acquisition card and a serial-port servo controller board and the conventional control surfaces of the airplane (Figures 61-62). The program had the capability to generate the pulse width modulated signals to start, ramp-up, and safely stop the leading edge and trailing edge actuators.

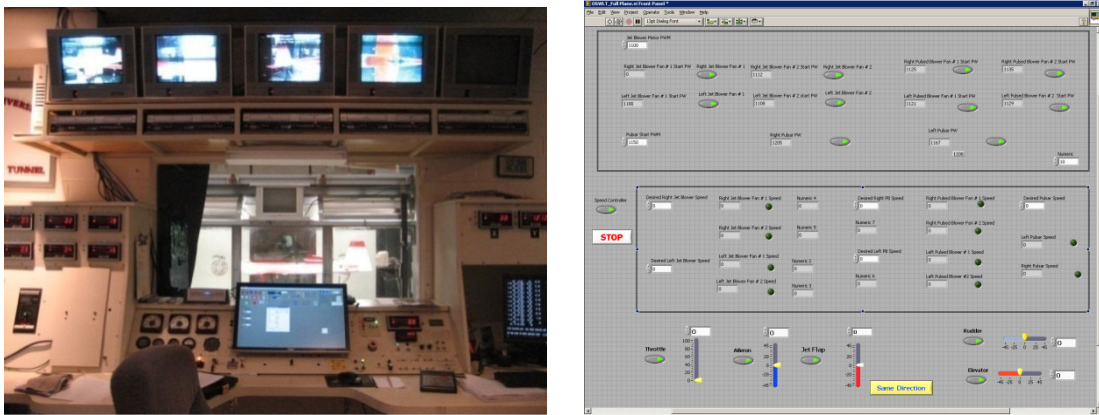


Figure 61. Control Station and the Labview[®] based program to control the vehicle

Wind Tunnel Test Matrix

The performance evaluation of the vehicle was carried out at take-off/landing speed of 17 m/s and cruising speed 30 m/s yielding a Reynolds number of 4.67×10^5 and 8.28×10^5 respectively. The tests were done with engine-off and the propeller of the vehicle was removed. The initial tests were conducted for both the full and in-board reduced ailerons, as described in Tables 11 and 12, to establish the performance characteristics of the conventional flight configuration.

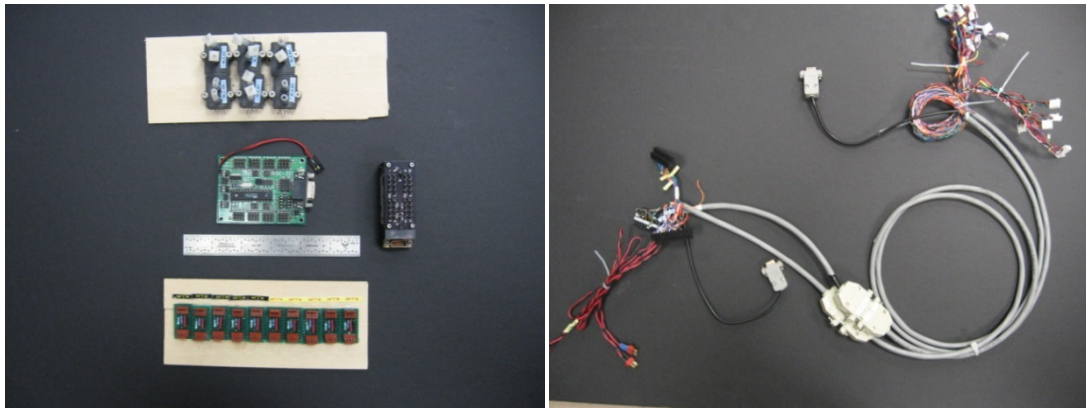


Figure 62. Electronic components and wiring harness

Table 11. Low speed wind tunnel test matrix using conventional wings

| Run No | Free Steam velocity(m/s) | Angle of Attack | Aileron Position | | Elevation Position | |
|--------|--------------------------|-----------------|------------------|---------|--------------------|---------|
| | | | Left | Right | Left | Right |
| 5 | 17 | -2° to 22° | Neutral | Neutral | Neutral | Neutral |
| 6 | 30 | -2° to 5° | Neutral | Neutral | Neutral | Neutral |
| 7 | 30 | -2° to 5° | Neutral | Neutral | +15° | +15° |
| 8 | 30 | -2° to 5° | Neutral | Neutral | -15° | -15° |
| 9 | 30 | -2° to 5° | +15° | -15° | Neutral | Neutral |
| 10 | 30 | -2° to 5° | +15° | -15° | +15° | +15° |
| 11 | 30 | -2° to 5° | +15° | -15° | -15° | -15° |
| 12 | 17 | -2° to 15° | Neutral | Neutral | Neutral | Neutral |
| 13 | 17 | -2° to 15° | Neutral | Neutral | +15° | +15° |
| 14 | 17 | -2° to 15° | Neutral | Neutral | -15° | -15° |
| 15 | 17 | -2° to 15° | +15° | -15° | Neutral | Neutral |
| 16 | 17 | -2° to 15° | +15° | -15° | +15° | +15° |
| 17 | 17 | -2° to 15° | +15° | -15° | -15° | -15° |

Table 12. Low speed wind tunnel test matrix using wings with reduced ailerons

| Run No | Free Steam velocity(m/s) | Angle of Attack | Aileron Position | | Elevation Position | |
|--------|--------------------------|-----------------|------------------|---------|--------------------|---------|
| | | | Left | Right | Left | Right |
| 18 | 30 | -2° to 5° | Neutral | Neutral | Neutral | Neutral |
| 19 | 30 | -2° to 5° | +15° | -15° | Neutral | Neutral |
| 20 | 17 | -2° to 15° | Neutral | Neutral | Neutral | Neutral |
| 21 | 17 | -2° to 15° | +15° | -15° | Neutral | Neutral |
| 22 | 30 | -2° to 5° | +30° | -30° | Neutral | Neutral |
| 23 | 17 | -2° to 5° | +30° | -30° | Neutral | Neutral |

The behavior of the leading edge pulser was studied in a standalone condition to document its performance as a function of the pulser frequency, F^+ and the jet momentum coefficient, C_μ . The hot wire anemometry data were acquired using a single wire TSI Inc. 1201 hot wire probe installed in TSI IFA 300 thermal anemometry system. The hot wire was placed at the downstream of the pulser near the jet exit on the surface of the wing. The hot wire was calibrated using TSI 1125 probe calibrator while monitoring the pressure using a Flowkinetics™ FKS 1 DP-PBM manometer. The calibration curve was obtained using a least square, fourth order curve fitting a quadratic relation between the known air velocity to the measured bridge voltage measured by the hot wire. The velocity profile of the exit jet is shown in Figure 63.

The pulser was operated at 2500 ± 25 rpm to achieve F^+ value of one at 17 m/s based on mean chord length of 410 mm. The pulsed blower motors were operated at 11000 ± 50 rpm yielding a $C_\mu = 0.0275$ at free stream velocity of 17m/s. The trailing edge jet blower motors were also run at 11000 ± 50 rpm yielding a $C_\mu = 0.0075$ and 0.0024 at the free stream velocity of 17m/s and 30 m/s respectively.

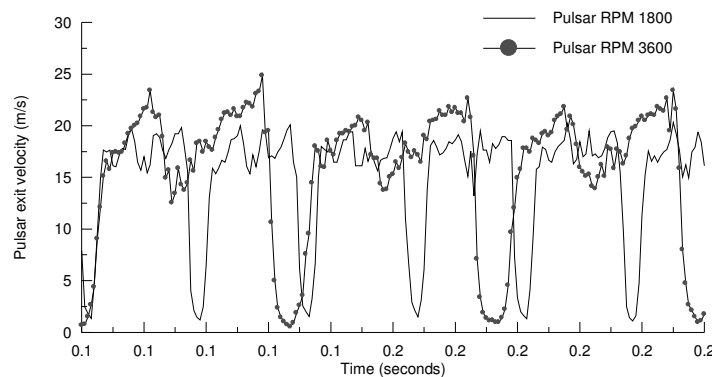


Figure 63. Pulsar velocity profile at fan speed of 12000 rpm

A few tests were also conducted to measure the performance of the vehicle at sideslip angles of 9° and 11° respectively. The complete test matrix for the effect of fluidic actuators on the performance of the vehicle has been presented in Table 13.

Table 13. Low speed wind tunnel test matrix using wings with fluidic actuators

| Run No | Free Stream velocity (m/s) | Angle of Attack | Jet Flap Position | | Trailing Edge C_μ | F + | Leading Edge C_μ |
|-----------------|----------------------------|--------------------------|-------------------|-------------|-----------------------|-----|----------------------|
| | | | Left | Right | | | |
| 24 | 30 | -2° to 5° | Neutral | Neutral | 0.0024 | 0 | 0 |
| 25 | 30 | -2° to 5° | $+45^\circ$ | -45° | 0.0024 | 0 | 0 |
| 26 | 30 | -2° to 5° | -45° | -45° | 0.0024 | 0 | 0 |
| 28 | 17 | -2° to 15° | $+45^\circ$ | -45° | 0.0075 | 0 | 0 |
| 29 | 17 | -2° to 15° | -45° | $+45^\circ$ | 0.0075 | 0 | 0 |
| 30 | 30 | -2° to 5° | $+45^\circ$ | -45° | 0 | 0 | 0 |
| 31 | 17 | -2° to 15° | $+45^\circ$ | -45° | 0 | 0 | 0 |
| 33 [#] | 30 | -2° to 5° | $+45^\circ$ | -45° | 0.0024 | 0 | 0 |
| 34 [#] | 30 | -2° to 5° | -45° | $+45^\circ$ | 0.0024 | 0 | 0 |
| 36 [*] | 17 | -2° to 22° | $+45^\circ$ | -45° | 0.0075 | 1 | 0.0275 |
| 37 [*] | 17 | -2° to 22° | -45° | $+45^\circ$ | 0.0075 | 1 | 0.0275 |
| 39 | 17 | -2° to 22° | Neutral | Neutral | 0.0075 | 1 | 0.0275 |
| 40 | 17 | -2° to 22° | $+45^\circ$ | -45° | 0.0075 | 1 | 0.0275 |
| 41 | 17 | -2° to 22° | -45° | -45° | 0.0075 | 1 | 0.0275 |
| 42 | 17 | -2° to 22° | -45° | $+45^\circ$ | 0.0075 | 1 | 0.0275 |
| 43 | 30 | -2° to 5° | -45° | $+45^\circ$ | 0.0024 | 0 | 0 |

Side Slip angle -9° ; * Side Slip angle -11°

Discussion of Test Results

The data reduction for the tests was done by Oran W. Nicks low speed wind tunnel facility using their proprietary software. The results are presented in the wind axes body-centered coordinate system. Further, the results discussed for the performance of the fluidic actuators do not include the effect of the prop wash, which would have been generated by the operation of the propeller.

Figure 64 shows the performance characteristics of the vehicle during the leading edge pulsed air actuation at take-off /landing speed of 17 m/s. No improvement has been observed in the lift and pitching moment characteristics of the vehicle in pre-stall regime of the conventional vehicle. The simultaneous actuation of the leading edge and trailing edge jet blower, however, has delayed the stall of the vehicle from 12° to 21° angle of attack with a 13% increase in the lift coefficient.

Figure 64 also indicates a dip in the measured lift from 16° to 19° . This may be due to the stalling of the elevators and the non-actuated part of the wing. The tests also indicate that the leading edge pulsed air blowing has performed equivalently well during the sideslip tests at -9° and -11° . The C_d vs. C_l curve in Figure 64 shows that the application of the fluidic actuator reduces the drag from 12° to 21° angle of attack. The decrease in drag coefficient is due to the reduction the pressure drag by the suppressing the separated flow.

Figure 65 shows the performance characteristics of the reduced ailerons and jet flap during the cruising speed of 30 m/s. The results indicate that the rolling moment generated by a 15° deflection of the reduced ailerons is 1/6 of the rolling moment (= 0.074) generated by the full aileron for the same deflection angle. The rolling moment coefficient increases to -0.0275 when the reduced ailerons are deflected by 30° . A similar trend is observed for landing/take-off speed of 17m/s as shown in Figure 66.

The differential actuation of the jet flap indicates a lower rolling moment coefficient than the conventional ailerons. The peak rolling moment coefficient generated during the cruise speed of 30m/s with fans running at 11000 ± 50 rpm (C_{μ} =

0.0024) and the jet flap being deflected differentially by 45° (at 0° sideslip angle) was -0.0075. The rolling moment coefficient generated by the full ailerons at 15° deflection is -0.0745. The rolling moments generated by the trailing edge actuator at a take-off/landing speed of 17 m/s ($C_\mu = 0.0075$) is -0.012, a 60% improvement over the previous test case. The results with pulsed blower actuation (Figure 64) also indicate a similar performance of the jet flap. The results shown in Figures 9, 64-66, thus indicate that higher jet momentum coefficients will be required to increase the roll control ability. The effect of both the jet flap ejecting air in the downward direction to augment the lift coefficients is shown in Figure 66. The jet flaps are able to increase the lift coefficient and delay the stall for 12° to 15° .

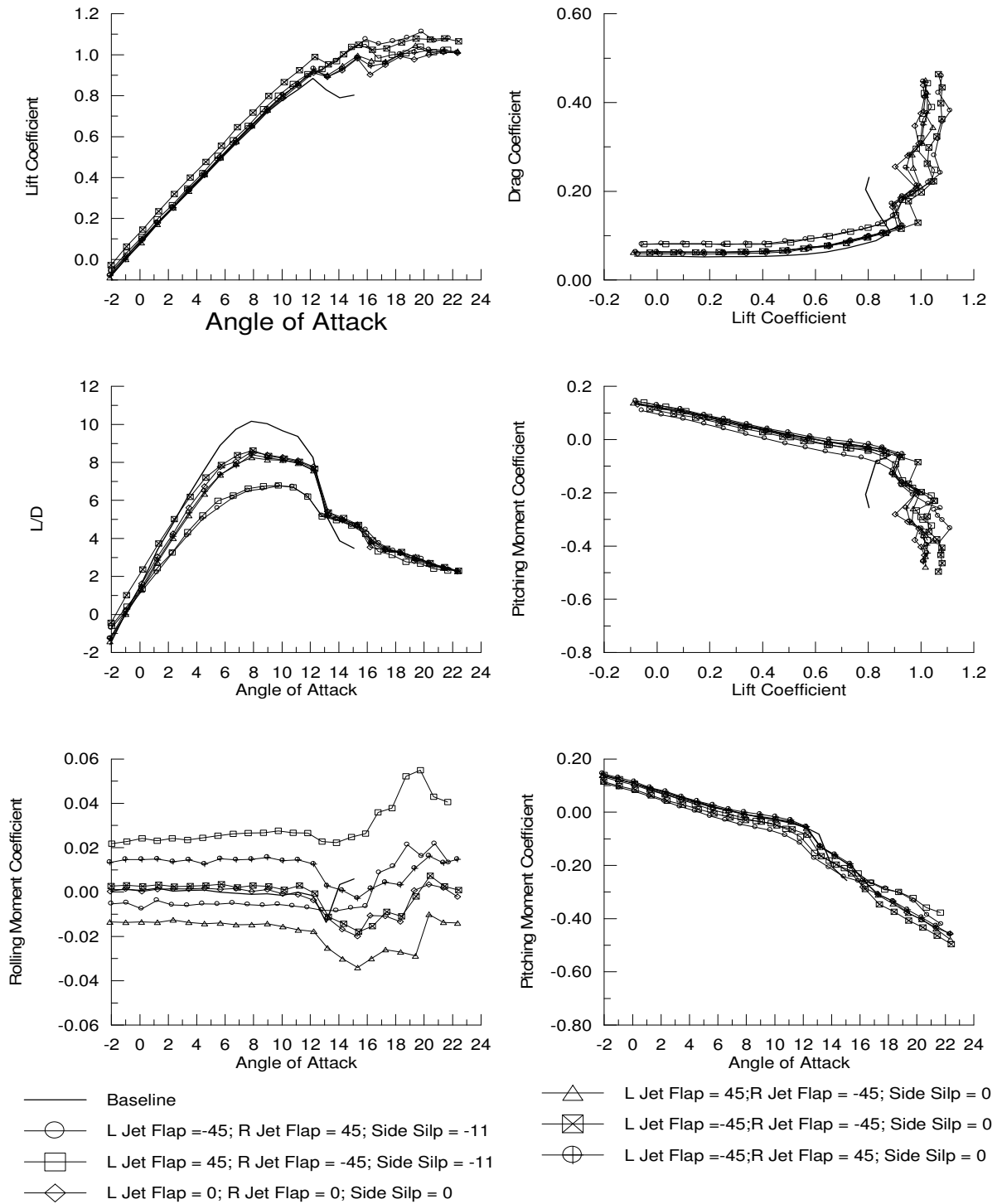


Figure 64. UAV performance at free stream velocity of 17 m/s, leading edge pulser $C_{\mu} = 0.0275$, $F^{+} = 1.0$; trailing edge jet blower $C_{\mu} = 0.0075$

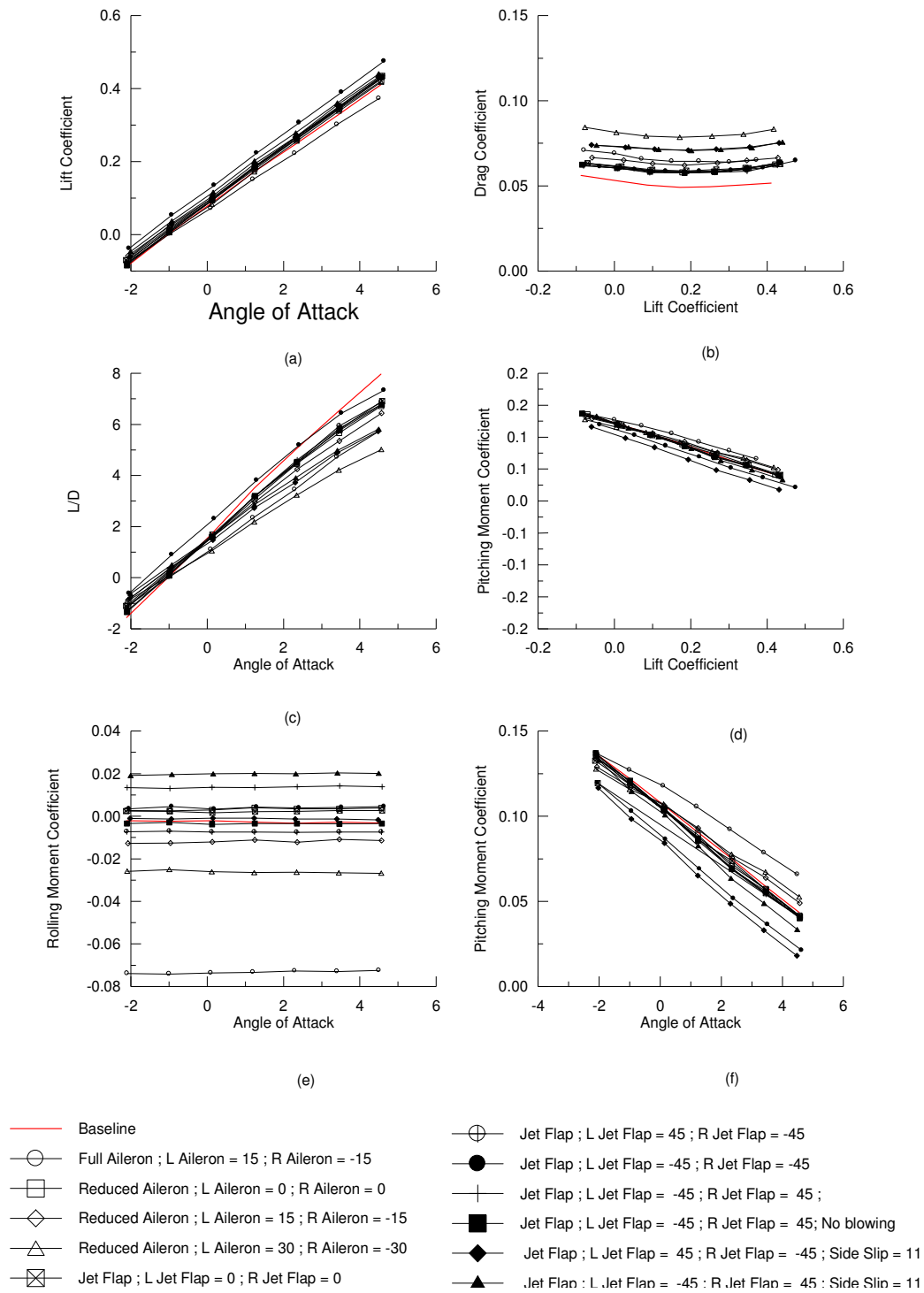


Figure 65. UAV performance with trailing edge actuators at free stream velocity of 30 m/s, trailing edge jet blower $C_{\mu} = 0.0024$

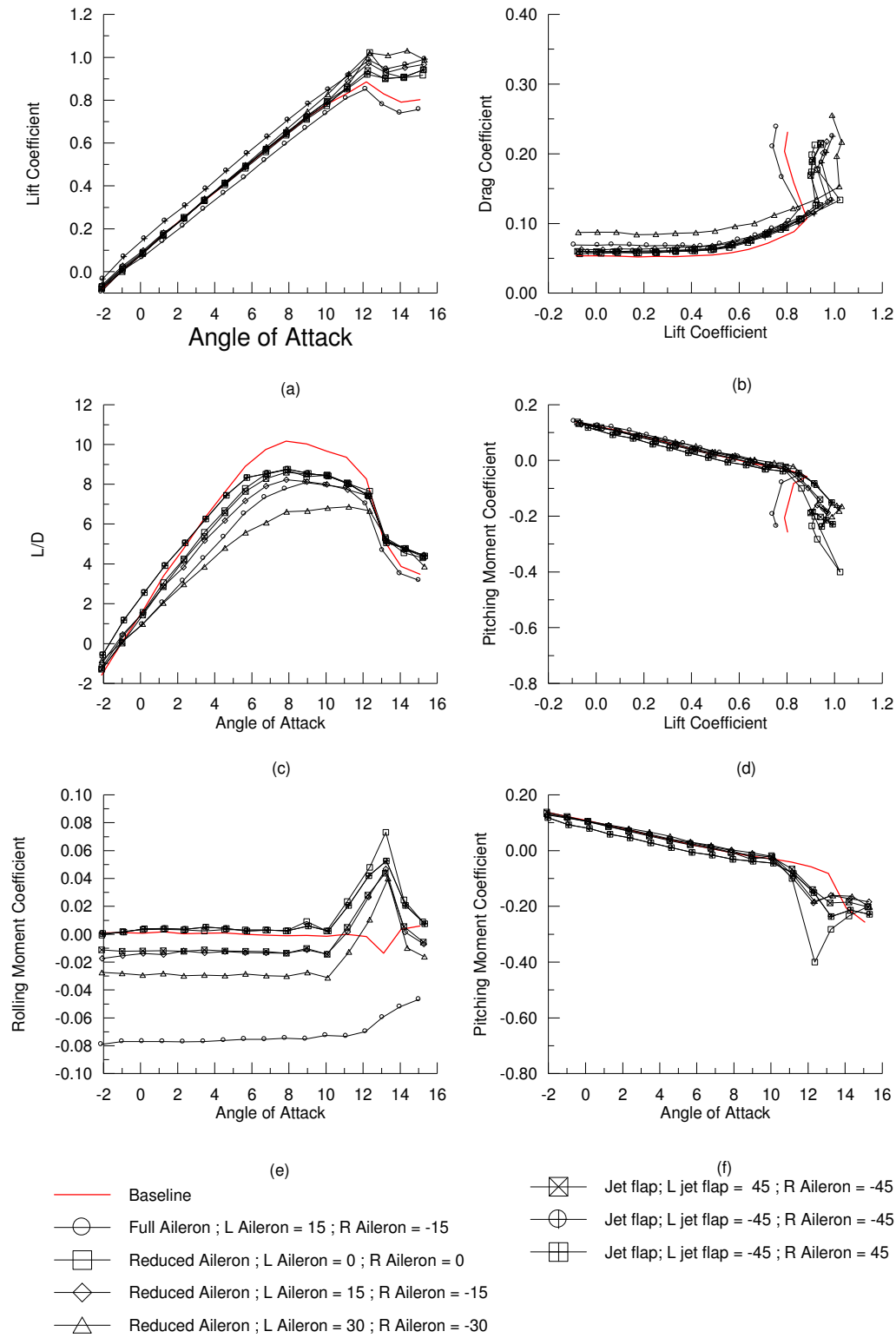


Figure 66. UAV performance with trailing edge actuators at free stream velocity of 17 m/s, trailing edge jet blower $C_{\mu} = 0.0075$

CONCLUSIONS AND RECOMMENDATIONS

Conclusions

This thesis presents a study on the effect of the flow control techniques on an unmanned aerial vehicle using fluidic actuators for the purpose of the flow separation delay and “hinge-less” control. The fluidic actuators constituted leading edge pulsed air blower at 15% chord location and trailing edge jet blower, capable of blowing air at $\pm 45^\circ$ from the chord line.

The location of the actuator mechanism, jet momentum coefficient and the pulsation frequency has dictated the maximum lift and angle of attack range over which the desired performance enhancement has been achieved. The actuation of the trailing edge jet actuators at low angle of attack regime indicated sufficient lift and pitching moment authority for the hinge-less control.

The full scale testing of the unmanned aerial vehicle with the fluidic actuators at the low speed wind tunnel testing demonstrated the delay of the stall of vehicle from around angle of attack of 12° to 21° . A 60% reduction in the length of the aileron on the outboard side led to 80% reduction in the rolling moments. The data have also indicated that the trailing edge actuators were able to demonstrate the roll control capability at jet momentum coefficient of 0.0024 at the cruising speed of 30 m/s.

Recommendations

The current design of the trailing edge jet limits the maximum jet momentum coefficient to 0.0024 at the cruising speed of 30 m/s and the jet deflection angle to $\pm 45^\circ$. Improvements can be made in the trailing edge design to increase the exit velocity and deflect the jet to higher angles to increase the roll control ability.

The wind tunnel tests were done without the operation of the propeller. Thus, the effects of the prop wash were not established during the test. Additional, in-flight test with the conventional wings and with reduced ailerons should be performed to establish the prop wash effects.

REFERENCES

1. Chang, R. C., Hsiao, F. B., and Shyu, R. N., "Forcing Level Effects of Internal Acoustic Excitation on the Improvement of Airfoil Performance," *Journal of Aircraft*, Vol. 29, No. 5, 1992, pp 823-829.
2. Klausmeyer, S. M., Papadakis, M., and Lin, J. C., "A Flow Physics Study of Vortex Generators on a Multi Element Airfoil," *AIAA Paper 1996-0548*, 34th Aerospace Sciences Meeting and Exhibit, Reno, NV, January 15-18, 1996.
3. Rong F. Huang and Shih W. Mao, "Separation Control on a Cantilever Wing with a Self-Excited Vibrating Rod," *Journal of Aircraft*, Vol. 39, No .4, 2002, pp 609-615.
4. Tillman, T. G. and Hwang, D. P., "Drag Reduction on a Large-Scale Nacelle Using a Micro-Blowing Technique", *AIAA Paper 1999-0130*, AIAA Aerospace Sciences Conference, Reno, NV, 1999.
5. Kruger, W., "Drag Reduction by Suction of the Boundary Layer Separated Behind Shock Wave Formation at High Mach Numbers," *NACA Technical Memorandum 1168*, 1947.
6. Seifert, A., Bachar, T., and Wynanski, I., "The Effects of Forced Oscillations on the Performance of Airfoils," *AIAA Paper 1993-3264*.
7. Sun, M. and Hamdani, H., "Separation Control by Alternating Tangential Blowing/Suction at Multiple Slots," *AIAA Paper 2001-0297*, 39th Aerospace Sciences Meeting, 2001.

8. Ashpis, D. E., and Reshotko, E., "The Vibrating Ribbon Problem – Revisited," *Journal of Fluid Mechanics*, Vol. 213, April 1990, pp 531-547.
9. Choi, K. S. and Clayton, B. R., "The Mechanism of Turbulent Drag Reduction with Wall Oscillation," *International Journal of Heat and Fluid Flow*, Vol. 22, 2001, pp 1-9.
10. Gilarranz, J. L., Traub, L. W., and Rediniotis, O. K., "Characterization of a Compact, High-Power Synthetic Jet Actuator for Flow Separation Control," 40th AIAA Aerospace Sciences Meeting & Exhibit, Reno, NV, Jan. 14-17. 2002.
11. Gilarranz, J. L. and Rediniotis, O. K., "Compact, High-Power Synthetic Jet Actuators for Flow Separation Control," *AIAA Paper* 2001-0737.
12. Amitay, M., Smith, D. R., Kibens, V., Parekh, D. E., and Glezer, A., "Aerodynamic Flow Control Over an Unconventional Airfoil Using Synthetic Jet Actuators," *AIAA Journal*, Vol. 39, No. 3, 2002, pp 361-370.
13. Modi, V. J., Munshi, S. R., Bandyopadhyay and Yokomizo T., "High Performance Airfoil with Moving Surface Boundary Layer Control," *Journal of Aircraft*, Vol. 35, No. 4, 1998, pp 544-553.
14. Amitay, M., Washburn, A. E., Anders, S. G., Parekh, D. E., and Glezer, A., "Active Flow Control on the Stingray UAV: Transient Behavior," *AIAA Paper* 2003-4001, 33rd AIAA Fluid Dynamics Conference and Exhibit, Orlando, FL, 2003.
15. Parekh, D. E., Williams, S. P., Amitay, M., Glezer, A., Washburn, A. E., Gregory, I. M., and Scott, R. C., "Active Flow Control on the Stingray UAV:

Aerodynamic Forces and Moments,” *AIAA Paper* 2003-4002, 33rd AIAA Fluid Dynamics Conference and Exhibit, Orlando, FL, 2003.

16. Liebeck, R. H., “Design of Subsonic Airfoils for High Lift,” *Journal of Aircraft*, Vol. 15, No. 9, 1978, pp 547-561.
17. Neuhart, D. H., and Pendergraft, O. C., “A Water Tunnel Study of Gurney Flaps,” *NASA TM -4071*, Nov 1998.
18. Roy Myose, Ismael Heron, and Michael Papadakis, “Effect of Gurney Flaps on a NACA 0011 Airfoil,” *AIAA Paper* 1996-59, 34th Aerospace Sciences Meeting and Exhibit, Reno, NV, Jan. 15-18, 1996.
19. Papadakis, M., Myose, R. Y., Heron, I., and Johnson, B. L., “An Experimental Investigation of Gurney Flaps on a GA(W)-2 Airfoil with 25% Slotted Flap,” *AIAA Paper* 1996-2437, 34th Aerospace Sciences Meeting & Exhibit, Reno, NV, 1996.
20. Jeffrey, D., Zhang, X., and Hurst, D. W., “Aerodynamics of Gurney Flaps on a Single-Element High-Lift Wing,” *Journal of Aircraft*, Vol. 37, No. 2, 2000, pp 295-301.
21. Gerrad, J. H., “An Experimental Investigation of the Oscillating Lift and Drag of a Circular Cylinder Shedding Turbulent Vortices,” *Journal of Fluid Mechanics*, Vol. 11, Issue 2, 1961, pp 244-256.
22. Gai, S. L. and Palfrey R., “Influence of Trailing-Edge Flow Control on Airfoil Performance,” *Journal of Aircraft*, Vol. 40, No. 2, 2003, pp 332-337.
23. Yachen Li, Jinjun Wang, and Panfeng Zhang, “Influences of Mounting Angles and Locations on the Effects of Gurney Flaps,” *Journal of Aircraft*, Vol. 40, No. 3, 2003, pp 494-498.

24. Lance W. Traub, and Gaurav Agarwal, "Exploratory Investigation of Geometry Effects on Gurney Flap Performance." *Journal of Aircraft*, Vol. 44, No. 1, 2007, pp 349-351.
25. Allen, John B., "Trailing Edge Splitter," *United States Patent* 5265830, November 30, 1993.
26. Spence, D. A., "Some Simple Results for Two-Dimensional Jet-Flap Aerofoils," *The Aeronautical Quarterly*, November 1958, pp 395-406.
27. Miller A. C., "Flow Control via Synthetic Jet Actuation," M.S. Thesis, Texas A&M University, College Station, Texas, USA, 2004.
28. Lance W. Traub, Miller, A., and Rediniotis, O., "Preliminary Parametric Study of Gurney Flap Dependencies," *Journal of Aircraft*, Vol. 43, No. 4, 2006, pp 1242-1244.
29. Englar, R. J., "Circulation Control for High Lift and Drag Generation on STOL Airfoil," *Journal of Aircraft*, Vol. 12, No. 6, 1975, pp 457-463.
30. Jones, G. S., and Englar, R. J., "Advances in Pneumatic Controlled High Lift Systems Through Pulsed Blowing," *AIAA Paper* 2003-3411.
31. Lance W. Traub, David Lund, Zachary Reeder and Rediniotis O. K., Preliminary Flight Tests of a Hinge-Less Roll Control Effector," *Journal of Aircraft*, Vol. 43, No. 4, 2006 , pp 1244-1246.
32. Gad-el-Hak, M., "Flow Control: Passive, Active, and Reactive Flow Management," Cambridge University Press, New York, 2000, pp 150-188.
33. Gad-El-Hak M., and Bushnell Dennis M., "Separation Control-Review," ASME Transactions, *Journal of Fluids Engineering*, Vol. 113, March 1991, pp 5-30.

34. Johnson, W., Tennant, J. S., and Stamps, R. E, "Leading-Edge Rotating Cylinder for Boundary-Layer Control on Lifting Surfaces," *Journal of Hydronautics*, Vol. 9, No. 2, 1975, pp 76-78.
35. Mokhtarian, F. and Modi, V., "Fluid Dynamics of Airfoils with Moving Surface Boundary-Layer Control," *Journal of Aircraft*, Vol. 25, No. 2 , 1988, pp 163-169.
36. Modi V., Mokhtarian F., Fernando M., and Yokomizo T., "Moving Surface Boundary Layer Control as Applied to Two-Dimensional Airfoils," *AIAA Paper* 1989-296, 27th Aerospace Sciences Meeting, Reno, NV, January 9-12, 1989.
37. Wilmer H. Reed, "Active Control Device for Aircraft Tail Buffet Alleviation," *United States Patent* 5549260, August 27, 1996.
38. Huang L. S., Maestrello L., and Brayant T. D. , "Separation Control Over an Airfoil at High Angles of Attack by Sound Emanating from the Surface ," *AIAA Paper* 1987-1261, 19th Fluid Dynamics, Plasma Dynamics, and Lasers Conference, Honolulu, HI, June 8-10, 1987.
39. Koga, D. J., Reisenhel, P., and Nagib, H. M., "Control of Separated Flow Fields Using Forced Unsteadiness," *Fluids and Heat Transfer Report No. R-84-1*, Illinois Institute of Technology, Chicago, IL, 1984.
40. Bar-Sever, A., "Separation Control on an Airfoil by Periodic Forcing," *AIAA Journal*, Vol. 27, No. 6, 1989, pp 820–821.
41. Andrew M. Honohan, Michael Amitay, and Ari Glezer, "Aerodynamic Control Using Synthetic Jets, " *AIAA Paper* 2000-2401, Fluids 2000 Conference and Exhibit, Denver, CO, June 19-22, 2000.

42. David E. Parekh and Ari Glezer, "AVIA - Adaptive Virtual Aero Surface," *AIAA Paper* 2000-2474, Fluids 2000 Conference and Exhibit, Denver, CO, June 19-22, 2000.
43. Seifert S., Eliahu, D., Greenblatt, I. Wygnanski, "Use of Piezoelectric Actuators for Airfoil Separation Control," *AIAA Journal*, Vol. 36, No. 8, 1998, pp 1535-1537.
44. Seifert, A., and Pack, L., "Dynamics of Active Separation Control at High Reynolds Numbers," *AIAA Paper* 2000-0409, 38th Aerospace Sciences Meeting & Exhibit, Reno, NV, 2000.
45. Greenblatt D. and Wygnanski I., "Dynamic Stall Control by Oscillatory Forcing," *AIAA Paper* 1998-676, 36th Aerospace Sciences Meeting and Exhibit, Reno, NV, Jan. 12-15, 1998.
46. Seifert, A., Bachar, T., Koss, D., Shepshelovich, M., and Wygnanski, I., "Oscillatory Blowing: A Tool to Delay Boundary-Layer Separation", *AIAA Journal*, Vol. 31, No. 11, 1993, pp 2052-2060.
47. Wu, J. Z., Lu, X., Denny, A. G., Fan, M., and Wu, J., "Post-Stall Flow Control on an Airfoil by Local Unsteady Forcing," *Journal of Fluid Mechanics*, Vol. 371, 1998, pp 21-58.
48. Michael Amitay, Barton L. Smith, and Ari Glezer, "Aerodynamic Flow Control Using Synthetic Jet Technology", *AIAA Paper* 1998-208, 36th Aerospace Sciences Meeting and Exhibit, Reno, NV, January 12-15, 1998.
49. Gilarranz, J. L., Traub L. W., and Rediniotis O. K., "Characterization of a Compact, High-Power Synthetic Jet Actuator for Flow Separation Control," *AIAA Paper*

2002-127, 40th AIAA Aerospace Sciences Meeting and Exhibit, Reno, NV, January 14-17, 2002.

50. Gilarranz, J. L. and Rediniotis O. K., "Compact, High-Power Synthetic Jet Actuators for Flow Separation Control," *AIAA Paper* 2001-737, 39th Aerospace Sciences Meeting and Exhibit, Reno, NV, January 8-11, 2000.

51. Gilarranz, J. L., Traub L. W., and Rediniotis O. K., "A New Class of Synthetic Jet Actuators—Part I: Design, Fabrication and Bench Top Characterization," *Journal of Fluids Engineering*, Vol. 127, Issue 2, March 2005, pp 367-376.

52. Gilarranz, J. L., Traub L. W., and Rediniotis O. K., "A New Class of Synthetic Jet Actuators—Part II: Application to Flow Separation Control," *Journal of Fluids Engineering*, Vol. 127, Issue 2, March 2005, pp 377-387.

53. B. N. Taylor, Guide for the Use of the International System of Units (*SI*), *NIST Special Publication* 811, 1995 Edition (U.S. Government Printing Office, Washington DC, April 1995).

54. Guide to the Expression of Uncertainty in the Measurement, *ISO*, Geneva, Switzerland, 1993.

55. British Standards 1042 (1992), "Measurement of Fluid Flow in Closed Conduits", Section 1.1, 1992.

56. Jones, B. M., "The Measurement of Profile Drag by the Pitot Traverse Method," *Aeronautical Research Council R&M* 1688, 1936.

57. Barlow, J. B., Rae, W. H., and Pope, A., "Low-Speed Wind Tunnel Testing," 3rd ed., John Wiley & Sons Inc., New York, pp 176-186, 1999.

58. Hoerner, S. F., “Fluid-dynamic lift,” *Hoerner Fluid Dynamics*, Vancouver, WA, 1985, Chap. 3.
59. Barlow, J. B., Rae, W. H., and Pope, A., “Low-Speed Wind Tunnel Testing,” 3rd ed., John Wiley & Sons Inc., New York, Chap. 9, 1999.

VITA

Gaurav

M- 15, Saket,
New Delhi, 110017
India.

E-mail: gaurav_ag11@yahoo.co.in

Education:

M.S., Mechanical Engineering, Texas A&M University, 2007

B.E., Mechanical Engineering, National Institute of Technology, Allahabad, India, 2002

Professional Experience

| | |
|-----------------------------|------------------|
| Graduate Research Assistant | 08/2005- present |
|-----------------------------|------------------|

Aerospace Engineering Department, Texas A&M University

| | |
|----------------------|------------------|
| Technical Instructor | 10/2002 -08/2005 |
|----------------------|------------------|

Honda Sael Cars India Ltd, Greater NOIDA, India

| | |
|----------------|-----------------|
| Plant Engineer | 07/2002-10/2002 |
|----------------|-----------------|

GE Industrial Systems, Faridabad, India

Publications

Lance W. Traub, Gaurav Agarwal, "Exploratory Investigation of Geometry Effects on Gurney Flap Performance." *Journal of Aircraft*, Vol. 44, No.1, 2007, pp 349-351.